CRYSTAL PLASTICITY FINITE ELEMENT SIMULATIONS

USING DISCRETE FOURIER TRANSFORMS

A Dissertation
Presented to
The Academic Faculty

by

Hamad F. Al-Harbi

In Partial Fulfillment
of the Requirements for the Degree
Doctor of Philosophy in the
George W. Woodruff School of Mechanical Engineering

Georgia Institute of Technology
May 2014

CRYSTAL PLASTICITY FINITE ELEMENT SIMULAITONS

USING DISCRETE FOURIER TRANSFORMS

Approved by:

Dr. Surya R. Kalidindi, Advisor
George W. Woodruff School of
Mechanical Engineering
Georgia Institute of Technology

Dr. Hamid Garmestani
School of Materials Science and
Engineering
Georgia Institute of Technology

Dr. David L. McDowell
George W. Woodruff School of
Mechanical Engineering
Georgia Institute of Technology

Dr. Christopher L. Muhlstein
School of Materials Science and
Engineering
Georgia Institute of Technology

Dr. Richard W. Neu
George W. Woodruff School of
Mechanical Engineering
Georgia Institute of Technology

Date Approved: December 13, 2013

This thesis is dedicated to my parents, my wife, and my beautiful daughters. This thesis would not have been possible without the support and sacrifices of my wife.

ACKNOWLEDGEMENTS

I would like to thank my thesis advisor Prof. Surya R. Kalidindi for his support and guidance without which this work would not have been possible. I thank him for giving me the freedom to work on different research topics and encouraging me to explore my ideas. I am also grateful to Dr. David McDowell, Dr. Richard Neu, Dr. Hamid Garmestani, and Dr. Christopher Muhlstein for taking the time to be on my thesis committee.

I would like to express my sincere gratitude for everyone who helped and supported me during my PhD at both Drexel University and Georgia Tech. In particular, I would like to thank everyone in the MINED research group. I also thank my good friends Nabeel Al-Harthi, Bandar Al-Zahrani, and Mohammed Shamma who provided support through difficult times and encouraged me to reach my goals. I would like to thank my entire family for their support throughout the course of my education. I would like to especially thank my wife, without whose support and sacrifices I would not be here.

Additionally, I would like to thank the Saudi Arabian Cultural Mission at the United States, King Saudi University at Saudi Arabia, and the National Science Foundation (NSF GRANT # 0727931) for the financial support.

TABLE OF CONTENTS

LIST OF TABLES

LIST OF FIGURES

LIST OF SYMBOLS AND ABBREVIATIONS

Abbreviations

AHSS	Advanced High Strength Steels
BCC	Body Centered Cubic
C3D8	Continuum Three-Dimensional Eight-Noded Solid Element
CPFEM	Crystal Plasticity Finite Element Method
CSM	Continuous Stiffness Measurement
DFTs	Discrete Fourier Transforms
EBSD	Electron Backscatter Diffraction
FCC	Face Centered Cubic
FE	Finite Element
FEM	Finite Element Method
FFT	Fast Fourier Transform
FZ	Fundamental Zone
GSH	Generalized Spherical Harmonics
HCP	Hexagonal Close Packed
ICME	Integrated Computational Materials Engineering
IF-Steel	Interstitial-Free Steel
ODF	Orientation Distribution Function
OIM	Orientation Imaging Microscopy
RVE	Representative Volume Element
SD-CPFEM	Spectral Database Crystal Plasticity Finite Element Method
UMAT	User Materials Subroutine

Symbols

$\mathbf{F}$	Total deformation gradient tensor
$\mathbf{F}^*$	Elastic deformation gradient tensor
$\mathbf{F}^p$	Plastic deformation gradient tensor
$\mathcal{L}$	Fourth-order elasticity tensor defined in the crystal frame
$\mathbf{T}^*$	Second Piola-Kirchoff stress tensor
$\mathbf{E}^*$	Elastic strain tensor
$\mathbf{T}$	Cauchy stress tensor (Classical crystal plasticity approach)
$\mathbf{I}$	Second-order identity tensor
$\mathbb{I}$	Fourth-order identity tensor
$\mathbf{L}^{\mathrm{p}}$	Plastic velocity gradient tensor
$\mathbf{L}$	Velocity gradient tensor
$\dot{\gamma}^{\alpha}$	Shearing rate on the α^{th} slip system
$\mathbf{m}_0^{\alpha}$	Slip direction of the α^{th} slip system
$\mathbf{n}_0^{\alpha}$	Slip plane normal of the α^{th} slip system
τ^{α}	Resolved shear stress on the α^{th} slip system
s^{α}	Slip resistance of the α^{th} slip system
$\dot{\gamma}_0$	Reference value of the shearing rate
m	Strain rate sensitivity parameter
h_o	Initial hardening rate
s_s	Saturation value of the slip resistance
a	Hardening exponent
$\mathbf{W}$	Applied spin tensor
$\mathbf{W}^*$	Elastic spin tensor
$\mathbf{W}^{\mathrm{p}}$	Plastic spin tensor

$\mathbf{R}^{*}$	Lattice rotation tensor
$\varphi_1, \phi, \varphi_2$	Set of three Bunge-Euler angles used to bring the crystal frame into coincidence with sample frame
$\varphi_1^{\mathrm{D}}, \Phi^{\mathrm{D}}, \varphi_2^{\mathrm{D}}$	Set of three Bunge-Euler angles used to bring the principle frame of $\mathbf{D}^{p}$ into coincidence with the sample frame
$\varphi_1^{\mathrm{p}}, \Phi^{\mathrm{p}}, \varphi_2^{\mathrm{p}}$	Set of three Bunge-Euler angles used to bring the crystal frame into coincidence with the principle frame of $\mathbf{D}^{p}$
$\ddot{T}_l^{\mu\nu}$	Symmetrized generalized spherical harmonics (GSH)
${}_{ij}A_l^{\mu\nu}$, ${}_{ij}S_l^{\mu\nu}$, $G_l^{\mu\nu}$	Fourier coefficients (GSH representations)
$\boldsymbol{\sigma}'$	Deviatoric Cauchy stress tensor
$\boldsymbol{\sigma}$	Cauchy stress tensor (Spectral crystal plasticity approach)
$\mathbf{D}$	Stretching tensor
$\mathbf{D}^{\mathrm{p}}$	Plastic stretching tensor
$\mathbf{D}^{*}$	Elastic stretching tensor
g	Crystal lattice orientation with respect to the sample frame
g^{p}	Crystal lattice orientation with respect to the principle frame of $\mathbf{D}^{\mathrm{p}}$
$\mathbf{B}_{kn}$, $\mathbf{C}_{kn}$, G_{kn}	Fourier coefficients (DFTs representations)
θ	Deformation mode
$f(\mathrm{g})$	Orientation distribution function (ODF)
$\boldsymbol{\tau}^{\boldsymbol{\nabla}*}$	Jaumann rate of the Kirchoff stress tensor
$\widetilde{\boldsymbol{\mathcal{L}}}$	Fourth-order elasticity tensor defined in the current (deformed) frame
$\boldsymbol{\sigma}^{\boldsymbol{\nabla}*}$	Jaumann rate of the Cauchy stress tensor
$\boldsymbol{\sigma}'^{\mathrm{DFT}}$	Deviatoric Cauchy stress tensor computed using the crystal plasticity DFT databases
$\boldsymbol{\sigma}'^{\mathrm{Jmn}}$	Deviatoric Cauchy stress tensor computed using the Jaumann rate relations

$\Delta\boldsymbol{\sigma}$	Increment in the Cauchy stress tensor
$\Delta\boldsymbol{\varepsilon}$	Increment in the strain tensor
$\mathbf{E}_t$	Relative strain tensor
$\boldsymbol{\sigma}'^{(\mathrm{pr})}$	Deviatoric Cauchy stress tensor defined in the principal frame of $\mathbf{D}^{\mathrm{p}}$
$\mathbf{F}_t$	Relative deformation gradient tensor
$\mathbf{R}_t$	Relative rotation tensor
$\mathbf{U}_t$	Relative stretch tensor
P	Indentation load
h_e	Indentation elastic displacement
P^*	Indentation load at the initial point of effective contact
h^*	Indentation displacement at the initial point of effective contact
S	Continuous Stiffness Measurement (CSM) signal
σ_{ind}	Indentation stress
$\varepsilon_{\mathrm{ind}}$	Indentation strain
E^*	Indentation effective Young's modulus
a	Indentation contact radius
E_s	Young's modulus of the sample
E_i	Young's modulus of the indenter
ν_s	Poisson's ratio of the sample
ν_i	Poisson's ratio of the indenter
R^*	Effective radius
R_s	Sample radius
R_i	Indenter radius
h_t	Total displacement
h_r	Residual displacement

SUMMARY

Crystallographic texture and its evolution are known to be major sources of anisotropy in polycrystalline metals. Highly simplified phenomenological models cannot usually provide reliable predictions of the materials anisotropy under complex deformation paths, and lack the fidelity needed to optimize the microstructure and mechanical properties during the production process. On the other hand, physics-based models such as crystal plasticity theories have demonstrated remarkable success in predicting the anisotropic mechanical response in polycrystalline metals and the evolution of underlying texture in finite plastic deformation. However, the use of crystal plasticity models is extremely computationally expensive, and has not been adopted broadly by the advanced materials development community. In particular, the integration of crystal plasticity models with finite element (FE) simulations tools (called CPFEM) requires very large computational resources because of the high computational time required to solve the highly nonlinear, numerically stiff, crystal plasticity constitutive equations at every integration point in the FE mesh. This makes the use of CPFEM impractical when the size of the polycrystalline aggregate is very large.

Recently, our research group has established a new strategy to speed up the crystal plasticity computations at the crystal level through the use of a compact database of discrete Fourier transforms (DFTs). This new DFT database approach allows for compact representation and fast retrieval of crystal plasticity solutions, which is found to be able to speed up the calculations by about two orders of magnitude. In this thesis, we present the first successful implementation of this spectral database approach in a

commercial finite element code to permit computationally efficient simulations of heterogeneous deformations using crystal plasticity theories. More specifically, the spectral database approach to crystal plasticity solutions was successfully integrated with the implicit version of the commercial FE package ABAQUS through a user materials subroutine, UMAT, to conduct more efficient CPFEM simulations. Details of this new spectral database CPFEM are demonstrated and validated through a few example case studies for selected deformation processes on Face Centered Cubic (FCC) and Body Centered Cubic (BCC) metals. The evolution of the underlying crystallographic texture and its associated macroscale anisotropic properties predicted from this new approach are compared against the corresponding results from the conventional CPFEM. It is observed that implementing the crystal plasticity spectral database in a FE code produced excellent predictions similar to the classical crystal plasticity FE method, but at a significantly faster computational speed and much lower computational cost.

Additionally, in an effort to extend the application of the proposed approach to other material systems, new spectral crystal plasticity databases have been established and validated for BCC and Hexagonal Close Packed (HCP) metals. The utility of these spectral databases has also been demonstrated through selected case studies that include computation of the yield surfaces and a new class of plastic property closures. Furthermore, an important application of the CPFEM for the extraction of crystal level plasticity parameters in multiphase materials has been demonstrated in this thesis. More specifically, CPFEM along with a recently developed data analysis approach for spherical nanoindentation and Orientation Imaging Microscopy (OIM) have been used in this thesis to extract the critical resolved shear stress of the ferrite phase in dual phase steels.

It should be noted that the lack of knowledge of crystal-level slip hardening parameters for many important multiphase polycrystalline materials is a major challenge in applying crystal plasticity theories for simulating the deformation behavior of these materials. This new methodology offers a novel efficient tool for the extraction of crystal level hardening parameters in any single or multiphase materials.

CHAPTER 1

INTRODUCTION

The higher demand of producing fuel-efficient vehicles requires rapid evaluation of advanced new materials in the product design along with their manufacturing routes. The complex microstructures of these materials and their associated properties place more demands on using advanced numerical simulation analysis in the product design stage instead of the conventional experimental trial and error loops. Considerable attention has been paid to conducting accurate finite element (FE) simulations of sheet metal forming operations as they form one of the most widely used production processes in the automobile manufacturing industry. In particular, there have been significant efforts to improve the constitutive descriptions of the material's elastic-plastic anisotropy during large strain metal forming operations. Most of these constitutive equations are based on phenomenological relations, mainly because of their relatively short computation times and easy access to the needed model parameters from standard testing methods. These models, however, do not account for the important details of material microstructure such as texture (Bunge, 1993a) and its evolution, which are known to be a major source of anisotropy in polycrystalline metals. Consequently, the simplified models cannot usually provide reliable predictions of the materials anisotropy under complex deformation paths, and lack the ability needed to optimize the microstructure and mechanical properties during the production process. The concept of integrating microstructure and property predictions with product design and manufacturing processes is one of the major goals of the Integrated Computational Materials Engineering (ICME)

(Allison, 2011; Panchal et al., 2013; Pollock et al.). In this context, physics-based models such as crystal plasticity theories have shown remarkable success in predicting the anisotropic mechanical response in polycrystalline metals and the evolution of underlying texture in finite plastic deformation. However, the use of crystal plasticity models is extremely computationally expensive, and has not been adopted broadly by the advanced materials development community.

Significant numbers of studies have been devoted to integrate plastic anisotropy into finite element formulations. The simple and most widely approach is to use constitutive laws based on phenomenological descriptions of the anisotropic yield surface (referred as normality flow rules) in the FE analysis. The most commonly used description of the anisotropic yield surface was suggested by Hill in 1948 in the form of a quadratic function (Hill, 1948, 1990). Several improvements have been proposed in the last few decades (Barlat, 1987; Barlat and Lian, 1989; Cazacu et al., 2006; Lian et al., 1989; Plunkett et al., 2007; Plunkett et al., 2006). The material parameters needed for the yield function expressions in these models are usually extracted from a small number of standard mechanical tests. The main advantage of using analytical expressions for the yield surface in the FE models is the short simulation times. This approach, however, neglects the effect of texture and its evolution during the deformation process. The fact that the same yield surface is used at every material point in the specimen makes the predictions from this approach questionable in forming operations that involve complex deformation paths. This is because the yield surfaces in different regions in the specimen are expected to evolve differently due to differences in texture evolution caused by the difference in local deformation histories.

In order to include the effect of initial texture on the shape of yield surfaces, Van Houtte and coworkers (Li et al., 2003; Van Houtte, 1994; Van Houtte and Van Bael, 2004; Van Houtte et al., 1995; Van Houtte et al., 2009) have developed analytical expressions of the yield loci based on the initial crystallographic texture of the material. The large numbers of material parameters needed for the analytical expression of the plastic potential in this method are extracted from crystal plasticity models. The texture-based yield surface approach can capture the effect of the initial texture on the plastic anisotropy, but it again neglects the effect of texture evolution during plastic deformation, which plays a prominent role in large strain metal forming operations.

Instead of the yield surface concept, the direct application of crystal plasticity theories provides an alternative approach to predict the plastic anisotropy of polycrystalline materials by accounting for the fundamental mechanism of plastic deformation at the scale of the constituent single crystals. The crystal plasticity constitutive equations define the response of each crystal by taking into account the details of slip system geometry in each individual crystal. To predict the response of the overall polycrystalline aggregate, one needs to use one of the homogenization models that can be classified based on the assumed local interaction between grains, such as Taylor-type (also known as full constraints) (Taylor, 1938), relaxed constraints (Kocks and Mecking, 2003), LAMEL (Van Houtte et al., 2005), self-consistent (Lebensohn et al., 2004; Lebensohn and Tomé, 1993; Lebensohn et al., 2007; Molinari et al., 1987), and crystal plasticity finite element models (Bachu and Kalidindi, 1998; Kalidindi and Anand, 1994; Kalidindi et al., 1992; Kalidindi and Schoenfeld, 2000; Needleman et al., 1985; Peirce et al., 1982, 1983). The simplest and most widely used approach is the

Taylor-type model. In this method, the applied velocity gradient tensor at the microscale is assumed to be the same as the one applied at the macroscale (on the polycrystal). The macroscopic stress for the polycrystal is obtained by volume averaging the stresses inside the polycrystal. The Taylor-type model usually provides good predictions of the overall anisotropic stress-strain response and the averaged texture evolution for single-phase cubic metals (Bronkhorst et al., 1992b). However, it usually lacks good predictions at the scale of individual crystal and it fails to show the development of heterogeneities within the grains (Bhattacharyya et al., 2001; Kalidindi, 2004; Van Houtte et al., 2005).

The most sophisticated and successful model that takes into account the local interactions between all grains in the sample is the crystal plasticity finite element method (called CPFEM) (Bachu and Kalidindi, 1998; Kalidindi and Anand, 1994; Kalidindi et al., 1992; Kalidindi and Schoenfeld, 2000; Needleman et al., 1985; Peirce et al., 1982, 1983). This approach uses the finite element method to find the response of the polycrystal by placing a finite element mesh over the grains such that each element represents one grain or part of the grain. The crystal lattice orientations and material state variables are updated at every material point in the specimen by solving the crystal plasticity constitutive equations. In this approach, the equilibrium and compatibility conditions are satisfied using a weak form of the principle of virtual work in a given finite element. This model not only provides excellent predictions of the texture and anisotropic stress-strain response, but also predicts the local lattice rotations and heterogeneity of plastic deformation at the crystal level (Choi et al., 2011; Delaire et al., 2000; Erieau and Rey, 2004; Héripré et al., 2007; Kalidindi et al., 2004a; Kanjarla et al., 2010; Musienko et al., 2007; Raabe et al., 2002; Sachtleber et al., 2002; St-Pierre et al.,

2008; Zhao et al., 2008). This approach, however, requires very large computational resources because of the high computational time required to solve the highly nonlinear, numerically stiff, crystal plasticity constitutive equations at every integration point. This makes the use of CPFEM impractical when the size of the polycrystalline aggregate is very large.

Several other higher-order homogenization models have also been proposed to obtain the response of the polycrystal from the responses of constituent single crystals based on certain assumptions regarding grain interactions. The most widely used approach is the viscoplastic self-consistent model (Lebensohn et al., 2004; Lebensohn and Tomé, 1993; Lebensohn et al., 2007; Molinari et al., 1987). The self-consistent approach assumes that each crystal acts as an ellipsoidal inclusion embedded in a homogenous effective medium that has the average behavior of the polycrystal. Therefore, the local interaction between each crystal and the neighboring crystals is taken in an average sense over the complete polycrystal. On the other hand, the LAMEL model considers the local interactions between immediate neighboring grains by careful examination of the stress equilibrium at the grain boundaries (Kanjarla et al., 2010; Liu et al., 2002; Van Houtte et al., 2002; Van Houtte et al., 2006; Van Houtte et al., 2005). Numerous studies have been published to compare the predictions from the different homogenization methods (see for example (Bonilla et al., 2007; Lebensohn et al., 2003; Van Houtte et al., 2002; Van Houtte et al., 2005)). Van Houtte et al. (Van Houtte et al., 2002; Van Houtte et al., 2005)) provided quantitative comparisons between different homogenization methods including full-constraints, relaxed constrains, LAMEL, visco-plastic self-consistent, and CPFEM models. The CPFEM is usually used to validate any

other homogenization model because it accounts for both stress equilibrium and strain compatibility (although in a weak numerical sense). However, one should note that the predictions from the CPFEM depend on the mesh density of the FE model. It is believed that for higher anisotropic materials and/or complex deformation processes, higher mesh resolution would be necessary in order to describe the microstructure and capture the intergranular heterogeneous strain and stress fields. However, this would incur much higher computational cost.

The homogenization approaches described above are usually applied to a single representative polycrystalline aggregate with a given initial texture subjected to particular boundary conditions. However, when using crystal plasticity constitutive equations in FE tools for simulating large-scale applications such as metal forming operations, a representative polycrystalline microstructure needs to be assigned to each integration point in the FE model. In this case, a suitable homogenization approach needs to be employed to obtain the mechanical behavior of the polycrystalline aggregate at each material point. The execution of such simulations becomes computationally prohibitive if the model consists of a large number of elements. Several approaches have been developed to improve the computational efficiency of these simulations. As an example, a texture component analysis is proposed by Raabe et al. (Raabe and Roters, 2004; Raabe et al., 2004; Tikhovskiy et al., 2007; Zhao et al., 2004) to decrease the number of discrete crystal orientations at each integration point in the FE model. In this approach, the orientation distribution function is decomposed into texture and background (random) components using texture component functions. The texture components are then fed into the FE mesh using a small number of discrete crystal orientations. The texture-

component CPFEM significantly enhances the computation efficiency when simulating metal forming operations. However, the initial background (random) texture component is still not accurately incorporated into the FE mesh. This is mainly because the initial random components can evolve into preferred orientations during the simulation. It is important to note that the computational efficiency in this method comes only from the use of a small number of crystal orientations at every integration point instead of a large set of orientations that is usually needed to reproduce the crystallographic texture. In other words, the high computational time required to solve the highly nonlinear crystal plasticity constitutive equations for every crystal orientation is still not improved. Therefore, the texture-component CPFEM becomes inefficient if the FE model consists of a very large number of elements. Another promising approach called materials knowledge systems (MKS) has been recently developed based on the concept of statistical continuum theories (Kröner, 1977; Kroner E. In: Gittus J, 1986) to provide computationally efficient scale-bridging relationships between the macro- and micro-length scales (Al-Harbi et al., 2012; Fast and Kalidindi, 2011; Kalidindi et al., 2008; Kalidindi et al., 2010; Landi and Kalidindi, 2010; Landi et al., 2010). The MKS framework has been shown to be well suited for conducting practical multi-scale simulations where every material point at the macroscopic level is associated with a representative microstructure. The MKS approach was applied to different problems involving non-linear material behavior such as spinodal decomposition and rigid-plastic deformation. However, the MKS formulation has not yet been applied to crystal plasticity framework. More details of the MKS framework and its implementation into FE tools to enable multiscale materials modeling are explained in Appendix A.

There is a critical need to speed up solving the crystal plasticity constitutive equations in order to use CPFEM within reasonable computation cost in a number of advanced metals development efforts. Knezevic et al. (Knezevic et al., 2009; Knezevic et al., 2008a) has recently established a new strategy to speed up the crystal plasticity computations at the crystal level through the use of a compact database of discrete Fourier transforms (DFTs). This spectral database is used to efficiently reproduce the solutions for the main functions of the crystal plasticity theory for any given crystal orientation subjected to arbitrary deformation mode. The spectral database approach has been successfully applied in face-centered cubic polycrystalline metals that deform by crystallographic slip. This approach was found to be able to speed up the crystal plasticity computations by two orders of magnitude compared to the conventional crystal plasticity model. Another special advantage of the spectral database is that trade-offs can be made by the user in terms of the desired accuracy and computation speed in any simulation through the selection of the truncation levels in the number of dominant DFTs used. The spectral database has been demonstrated only for rigid-viscoplastic deformation, and has not been incorporated into FE simulation tools.

The current dissertation has mainly focused on addressing the challenges associated with integration of the DFT-based spectral crystal plasticity databases with a commercial FE tool to conduct more efficient CPFEM simulations on both FCC and BCC polycrystalline materials. The development of this new computationally efficient spectral database CPFEM (SD-CPFEM) is considered the main unique contribution of the current thesis. Additionally, in an effort to extend the application of the proposed approach to other material systems, new spectral crystal plasticity databases have also

been established and validated for BCC and HCP metals. Furthermore, an important application of the CPFEM for the extraction of crystal level plasticity parameters in multiphase materials has been demonstrated in this thesis. More specifically, CPFEM along with a recently developed data analysis approach for spherical nanoindentation and Orientation Imaging Microscopy (OIM) have been used in this thesis to extract the critical resolved shear stress in dual phase steels. It should be noted that the lack of knowledge of crystal-level slip hardening parameters for many important multiphase polycrystalline materials is a major challenge in applying crystal plasticity theories for simulating the deformation behavior of these materials. Below is a summary of the main results accomplished in the current thesis:

1. A new spectral crystal plasticity database has been established and validated for BCC metals with 48 slip systems. Another new spectral database has also been developed for HCP metals for only two slip resistance ratios. These spectral databases are successfully applied to a rigid-viscoplastic polycrystal Taylor-type model to predict the texture evolution and stress-strain response for a few selected examples of deformation processes. The utility of these databases has been demonstrated through selected case studies that include computation of the yield surfaces and a new class of plastic property closures for both FCC and BCC metals.
2. The DFT database approach for crystal plasticity computations has been integrated with the commercial FE package ABAQUS through a user materials subroutine, UMAT. This will allow the user to conduct more efficient CPFEM

simulations at dramatically reduced computational cost. For this purpose, the following two tasks were accomplished:

2.1. The crystal plasticity calculations using spectral databases have been extended from rigid-viscoplastic behavior into elastic-viscoplastic deformation. A new modified Newton-Raphson scheme has been developed to decompose the total strain rate tensor into elastic and plastic parts.

2.2. A new efficient analytical expression for the Jacobian required to implement the spectral databases with any implicit finite element code has been developed in this study.

3. A combined application of nanoindentation, OIM, and CPFEM has been used to estimate the critical resolved shear stress of the ferrite phase in dual phase steels.

The current thesis is structured as follows. We briefly review in Chapter 2 the classical and spectral crystal plasticity approaches used in this study. The chapter begins with a review of the crystal plasticity constitutive equations followed by a short summary of the fully implicit time-integration procedure to solve these constitutive equations as described by Kalidindi et al. in Ref. (Kalidindi et al., 1992). The spectral database approach to crystal plasticity computations is then reviewed. We then proceed to build and validate new DFT-based crystal plasticity databases for BCC and HCP metals in Chapter 3. We also demonstrate in this chapter some of the computational advantages of the DFT-based spectral databases in two important directions: (i) fast computation of yield surfaces in the five-dimensional deviatoric stress space predicted by the Taylor model for both FCC and BCC metals, and (ii) delineation of first-order plastic property

closures for both FCC and BCC metals without any simplifying assumptions of sample symmetry. In Chapter 4, we proceed to demonstrate the necessary steps to integrate the DFT database approach for crystal plasticity computations with the FE package ABAQUS. In particular, we illustrate how the crystal plasticity calculations using spectral databases are extended from rigid-viscoplastic behavior into elastic-viscoplastic deformation, and the details of the computation of the Jacobian required for implementing the spectral databases with any implicit FE tool. We also validate in Chapter 4 the predictions from the new spectral database CPFEM tools developed in this thesis against the corresponding predictions from the classical CPFEM tools using a few selected case studies. We present in Chapter 5, preliminary results from the application of a new methodology for extracting the critical resolved shear stress of the ferrite phase in dual phase steels using a combined application of nanoindentation, OIM, and CPFEM. We summarize our conclusions in Chapter 6 with some suggestions for future research.

CHAPTER 2

BACKGROUND

2.1 Crystal Plasticity Framework

Crystal plasticity models are used in many applications because of their ability to relate the anisotropic behavior of polycrystalline materials to their microstructures (Asaro and Needleman, 1985b; Bridier et al., 2009; Bronkhorst et al., 1992a; Delannay et al., 2002; Garmestani et al., 2002; Goh et al., 2003; Hosford and Caddell, 1993; Kalidindi et al., 1992; Mayeur and McDowell, 2007; Mayeur et al., 2008; McDowell, 2010; Raabe et al., 2005; Raabe et al., 2001; S. R. Kalidindi, 2004; Van Houtte et al., 2002). These physics-based constitutive equations not only provide better predictions of the anisotropic material response but can also capture the texture evolution in a polycrystalline sample subjected to finite plastic deformation. Furthermore, the integration of crystal plasticity models with FE simulation tools opens the path to a more reliable prediction of the material response when subjected to complex loading paths. However, the high computational time required to solve the highly nonlinear, numerically stiff, crystal plasticity constitutive equations makes the application of these theories impractical in simulating large scale applications.

In this section, some of the main details of crystal plasticity modeling framework are summarized. For finite deformations, the total deformation gradient tensor **F** on a crystalline region can be decomposed into elastic and plastic components as (Asaro and Needleman, 1985a)

$$\mathbf{F} = \mathbf{F}^{*}\mathbf{F}^{\mathrm{p}} \tag{2.1}$$

where $\mathbf{F}^{*}$ contains deformation gradients due to elastic stretching and lattice rotation, while $\mathbf{F}^{\mathrm{p}}$ denotes the deformation gradient due to plastic deformation. The constitutive equation in the crystal can be expressed as

$$\mathbf{T}^{*} = \boldsymbol{\mathcal{L}}\,\mathbf{E}^{*} \tag{2.2}$$

where $\boldsymbol{\mathcal{L}}$ is the fourth-order elasticity tensor, $\mathbf{T}^{*}$ and $\mathbf{E}^{*}$ are a pair of work conjugate stress and strain measures defined using the elastic deformation gradient tensor as

$$\mathbf{T}^{*} = \mathbf{F}^{*-1}[(\det \mathbf{F}^{*})\,\mathbf{T}]\,\mathbf{F}^{*-\mathrm{T}}\,, \quad \mathbf{E}^{*} = \frac{\mathbf{1}}{\mathbf{2}}\left(\mathbf{F}^{*\mathrm{T}}\,\mathbf{F}^{*} - \mathbf{I}\right) \tag{2.3}$$

where $\underline{\mathbf{T}}$ is the Cauchy stress in the crystal and $\underline{\mathbf{I}}$ is the second-order identity tensor. The evolution of $\underline{\mathbf{F^p}}$ can be expressed as

$$\dot{\mathbf{F}}^{\mathrm{p}} = \mathbf{L}^{\mathrm{p}}\,\mathbf{F}^{\mathrm{p}} \tag{2.4}$$

where $\mathbf{L}^{\mathrm{p}}$ is the plastic velocity gradient tensor given by

$$\mathbf{L}^{\mathrm{p}} = \sum_{\boldsymbol{\alpha}} \dot{\gamma}^{\alpha}\ \mathbf{m}_0^{\alpha} \otimes \mathbf{n}_0^{\alpha} \tag{2.5}$$

where $\dot{\gamma}^{\alpha}$ is the shearing rate on the slip system α, and $\mathbf{m}_0^{\alpha}$ and $\mathbf{n}_0^{\alpha}$ denote the slip direction and the slip plane normal of the slip system α, respectively in the initial configuration. In the rate dependent formulation (Hutchinson, 1976; Needleman et al., 1985; Pan and Rice, 1983), the shearing rate on each slip system depends on the resolved shear stress τ^{α} and

the slip resistance s^{α} of that slip system. It can be expressed in a power-law relationship as (Kalidindi et al., 1992)

$$\dot{\gamma}^{\alpha} = \dot{\gamma}_0 \left|\frac{\tau^{\alpha}}{s^{\alpha}}\right|^{\frac{1}{m}} \mathrm{sgn}(\tau^{\alpha}),\ \tau^{\alpha} \approx \mathbf{T}^{*} \cdot \mathbf{m}_0^{\alpha} \otimes \mathbf{n}_0^{\alpha} \tag{2.6}$$

where $\dot{\gamma}_0$ is the reference value of the shearing rate, and m is the strain rate sensitivity parameter. For most metals at room temperature, the value of m is usually taken to be very small (~ 0.01). The evolution of the slip resistance can be described phenomenologically by a saturation-type law as (Brown et al., 1989)

$$\dot{s}^{\alpha} = h_o \left(1 - \frac{s^{\alpha}}{s_s}\right)^{a} \sum_{\beta} \left|\dot{\gamma}^{\beta}\right| \tag{2.7}$$

where h_o, s_s and a denote the slip hardening parameters. It should be noted that the latent hardening is neglected in Eq. (2.7). Finally, the lattice spin tensor $\mathbf{W}^{*}$ (and the related lattice rotation tensor, $\mathbf{R}^{*}$) in the crystalline region is given by

$$\mathbf{W}^{*} = \dot{\mathbf{R}}^{*}\mathbf{R}^{*\mathrm{T}} = \mathbf{W} - \mathbf{W}^{\mathrm{p}}, \qquad \mathbf{W}^{\mathrm{p}} = \frac{1}{2}\left(\mathbf{L}^{\mathrm{p}} - \mathbf{L}^{\mathrm{p}\mathrm{T}}\right) \tag{2.8}$$

where $\mathbf{W}$ is the applied spin tensor, and $\mathbf{W}^{\mathrm{p}}$ is the plastic spin tensor.

Various implicit and explicit time-integration schemes have been developed to solve the above constitutive equations (Cuitino and Ortiz, 1993; Delannay et al., 2006; Kalidindi et al., 1992; Li et al., 2006; Li et al., 2008; McGinty, 2001; Rossiter et al., 2010). It should be noted that the small value of the strain rate sensitivity parameter in Eq. (2.6) makes the system of equations extremely stiff. The implementation of explicit integration scheme, where the state variables at the current time step are updated based

on the values from the previous time step, requires an extremely small time step to obtain the desired accuracy and stability. Thus, explicit time integration is not usually desirable for quasi-static deformation. On the other hand, the fully implicit time-integration scheme allows the use of much larger time step, but it requires the use of an iterative process, such as Newton-Raphson method, to solve the system of equations. The convergence of any iterative procedure used in the fully implicit time-integration scheme becomes an issue because of the stiff nature of these equations. The fully implicit time-integration procedure of the above crystal plasticity constitutive equations as described by Kalidindi et al. in Ref. (Kalidindi et al., 1992) is summarized in Table 2.1. This algorithm is used in this work to validate the spectral crystal plasticity approach. A more detailed description of the implementation of these equations with the implicit version of the FE package ABAQUS is described by Kalidindi et al. in Ref. (Kalidindi et al., 1992).

Table 2.1: A summary of the fully implicit time-integration scheme of the crystal plasticity constitutive equations as described by Kalidindi et al. in Ref. (Kalidindi et al., 1992).

1. At the beginning, the following quantities are assumed to be known,
   - Initial slip systems$(\mathbf{m}_0^\alpha, \mathbf{n}_0^\alpha)$
   - Deformation gradients at the previous time step $\mathbf{F}(t)$ and the current time step $\mathbf{F}(\tau)$ where $\tau = t + \Delta t$
   - Plastic deformation gradient at time t, $\mathbf{F}^{\mathrm{p}}(t)$
   - Initial slip resistance s_o (for simplicity, the values of the slip resistance s^α are assumed to be constant here).
2. Start with an initial guess of the second Piola-Kirchoff stress, $\mathbf{T}^*$
3. Calculate the resolved shear stress,

$$\tau^\alpha = \mathbf{T}^* \cdot \mathbf{S}_0^\alpha, \qquad \mathbf{S}_0^\alpha = \mathbf{m}_0^\alpha \otimes \mathbf{n}_0^\alpha$$

4. Compute the increment of the shearing rate on the slip system α,

$$\Delta\gamma^\alpha = \Delta t \left(\dot{\gamma}_0 \left| \frac{\tau^\alpha}{s^\alpha} \right|^{\frac{1}{m}} \mathrm{sgn}(\tau^\alpha) \right)$$

Table 2.1 (continued).

5. Calculate the new second Piola-Kirchoff stress,

$$\widetilde{\mathbf{T}}^{*} = \mathbf{T}^{*\mathrm{tr}} - \sum_{\alpha} \Delta\gamma^{\alpha}\, \mathbf{C}^{\alpha}$$

where

$$\mathbf{T}^{*\mathrm{tr}} = \mathcal{L}\left[\frac{1}{2}\{\mathbf{A} - \mathbf{I}\}\right]$$

$$\mathbf{C}^{\alpha} = \mathcal{L}\left[\frac{1}{2}\left\{\mathbf{A}\,\mathbf{S}_0^{\alpha} + \mathbf{S}_0^{\alpha^T}\,\mathbf{A}\right\}\right]$$

$$\mathbf{A} = \mathbf{F}^{\mathrm{p}^{-T}}(t)\,\mathbf{F}^{\mathrm{T}}(\tau)\;\mathbf{F}(\tau)\;\mathbf{F}^{\mathrm{p}^{-1}}(t)$$

6. Use Newton-Raphson scheme to correct the stress,

$\mathbf{T}^{*}_{n+1} = \mathbf{T}^{*}_{n} - \mathbf{J}_n^{-1}[\mathbf{Err}_n]$

where

$$\mathbf{Err} = \mathbf{T}^{*} - \widetilde{\mathbf{T}}^{*}$$

$$\mathbf{J} = \frac{\partial \mathbf{Err}}{\partial \mathbf{T}^{*}}$$

7. If $max\left|(\mathbf{T}^{*}_{n+1})_{ij} - (\mathbf{T}^{*}_{n})_{ij}\right| >$ tolerance, go to step-2 and use $\mathbf{T}^{*}_{n+1}$

where tolerance is taken as $10^{-4}\ \mathrm{s_o}$.

8. Else (i. e. if error $<$ tolerance), calculate the Cauchy stress and update the state variables,

$$\mathbf{F}^{\mathrm{p}^{-1}}(\tau) = \mathbf{F}^{\mathrm{p}^{-T}}(t)\left[\mathbf{I} - \sum_{\alpha} \Delta\gamma^{\alpha}\, \mathbf{S}_0^{\alpha}\right]$$

$$\mathbf{F}^{*} = \mathbf{F}\;\mathbf{F}^{\mathrm{p}^{-1}}$$

$$\mathbf{T} = \frac{1}{(\det \mathbf{F}^{*})}\,\mathbf{F}^{*}\,\mathbf{T}^{*}\mathbf{F}^{\mathrm{T}}$$

As mentioned earlier, the crystal plasticity constitutive equations described above are applied at the crystal level and therefore predict the response of each individual crystal. Different homogenization methods have been proposed to find the response of the overall polycrystalline aggregate. The most commonly used homogenization models include the Taylor-type (Taylor, 1938), relaxed constraints (Kocks and Mecking, 2003), LAMEL(Van Houtte et al., 2005), self-consistent (Lebensohn et al., 2004; Lebensohn and Tomé, 1993; Lebensohn et al., 2007; Molinari et al., 1987), and CPFEM models (Bachu and Kalidindi, 1998; Kalidindi and Anand, 1994; Kalidindi et al., 1992; Kalidindi and Schoenfeld, 2000; Needleman et al., 1985; Peirce et al., 1982, 1983). These models can be classified based on the assumptions made with regard to the local interactions between the constituent grains. For example, the Taylor-type model assumes that there is no local interaction between the grains. The self-consistent approach assumes that each crystal acts as an ellipsoidal inclusion embedded in a homogenous effective medium that has uniform property. Therefore, the local interaction between each crystal and the neighboring crystals is taken in an average sense over the complete polycrystal. Furthermore, the CPFEM takes into account the local interaction between each grain and their neighbors by satisfying the equilibrium and compatibility conditions between the grains. A large number of studies have been performed to compare the predictions from the different homogenization methods (see for example (Bonilla et al., 2007; Lebensohn et al., 2003; Van Houtte et al., 2002; Van Houtte et al., 2005)). It is commonly agreed that the CPFEM provides better predictions compared to the other homogenization models because it accounts for both stress equilibrium and strain compatibility.

2.2 Crystal Plasticity Computations using Spectral Databases

The crystal plasticity framework described earlier demands significant computational resources. The stiff behavior of the crystal plasticity constitutive equations is a direct consequence of the fact that most metals have a very weak dependence on strain rate at room temperature which demands the use of a small value for the strain rate sensitivity parameter in the flow rule relation in the rate-dependent crystal plasticity formulations (see Eq. (2.6)) (Hutchinson, 1976; Needleman et al., 1985; Pan and Rice, 1983). Furthermore, the same set of equations are usually solved several times in most crystal plasticity simulations of various deformation processing operations. As an example, the implementation of the crystal plasticity equations in a finite element tool requires solving the same set of stiff equations for every crystal orientation at every integration point at every trial strain increment in the simulations. Therefore, the use of crystal plasticity models for simulating practical engineering problems requires extremely high computational effort.

A number of strategies have been proposed to speed up the crystal plasticity calculations. Bunge and Esling (Bunge and Esling, 1984) proposed a new method for predicting the crystallographic texture evolution in polycrystalline materials based on conservation principles in the orientation space (Clément and Coulomb, 1979). In this approach, the evolution of texture in the sample is captured in a spectral representation using Generalized Spherical Harmonics (GSH) as the basis functions. Kalidindi and Duvvuru (Kalidindi et al., 2006b) provided a detailed critical evaluation of the Bunge-Esling approach for capturing texture evolution during large plastic strains in metals. In spite of the good capability of the Bunge-Esling approach for predicting the texture

evolution, it was found that higher order terms of the Fourier representation were required in order to obtain sufficient accuracy. The evaluation of higher order terms demanded high computational cost.

Kalidindi et al. (Kalidindi et al., 2006b) developed another new formulation for performing more efficient crystal plasticity calculations using spectral database. The main idea of this new approach is based on building a spectral database that constitute efficient representations for the solutions of some important variables in crystal plasticity models. Then, one can use that database to perform all subsequent calculations without the need to solve the crystal plasticity equations. The main variables in this approach are selected such that they constitute the essential information needed for predicting the evolution of crystallographic texture and the anisotropic stress-strain behavior when solving the classical crystal plasticity equations. These variables include (i) the five independent components of the symmetric and deviatoric stress tensor σ'_{ij}, (ii) the three independent component of the skew-symmetric lattice spin tensor W^*_{ij}, and (iii) the total shear rate $\sum_{\alpha}|\dot{\gamma}^{\alpha}|$. In this approach, the orientation dependence of these variables under specified imposed deformation mode is captured in a spectral representation using generalized spherical harmonics as follow:

$$W^*_{ij}(g) = \sum_{l=1}^{\infty}\sum_{\mu=1}^{M(l)}\sum_{\nu=1}^{2l+1} {}_{ij}A_l^{\mu\nu}\,\ddot{T}_l^{\mu\nu}(g) \tag{2.9}$$

$$\sigma'_{ij}(g) = \sum_{l=1}^{\infty}\sum_{\mu=1}^{M(l)}\sum_{\nu=1}^{2l+1} {}_{ij}S_l^{\mu\nu}\,\ddot{T}_l^{\mu\nu}(g) \tag{2.10}$$

$$\sum_{\alpha}|\dot{\gamma}^{\alpha}|\,(\mathrm{g}) = \sum_{l=1}^{\infty}\sum_{\mu=1}^{M(l)}\sum_{\nu=1}^{2l+1} G_l^{\mu\nu}\,\ddot{T}_l^{\mu\nu}(\mathrm{g}) \tag{2.11}$$

where ${}_{ij}A_l^{\mu\nu}$, ${}_{ij}S_l^{\mu\nu}$, and $G_l^{\mu\nu}$ represent the Fourier coefficients and $\ddot{T}_l^{\mu\nu}$ denote the symmetrized generalized spherical harmonics, the two dots on the generalized spherical functions imply cubic crystal symmetry and triclinic sample symmetry. The independent variable g denotes the crystal lattice orientation defined using the Bunge-Euler angles which is a set of three orientations $\mathrm{g} = (\varphi_1, \phi, \varphi_2)$ that bring the crystal frame into coincidence with the sample frame (Bunge, 1993b). It should be noted that the development of the spectral database in this approach requires high computational cost but it is a one-time computational cost. In other words, once the above Fourier coefficients are established, they can be used directly in Eqs. ((2.9)-(2.11)) to capture the orientation dependence of the above important variables.

Although it is demonstrated that the spectral representations described above using generalized spherical harmonics can efficiently capture the orientation dependence of the selected important variables in the crystal plasticity calculations, it did not drastically improve the computational speed (Kalidindi et al., 2006b). This was mainly because of the high computational cost required for evaluating the generalized spherical harmonics. Knezevic et al. (Knezevic et al., 2008a) has developed another spectral database for the same important variables (i.e. deviatoric stresses, the lattice spins, and the total shear rates) using discrete Fourier transforms (DFTs) instead of using GSH. In this method, the solutions of these main variables predicted using the Taylor model are stored on a uniform grid in the orientation space and deformation mode space. Then,

these values are used in a local DFT-spectral interpolation to recover the values of these variables for any given orientation and deformation mode. It should be noted that the use of generalized spherical harmonics described earlier provides a more compact representation of the functional dependencies of interest (i.e. less number of terms are required to capture the orientation dependence of these variables) because the basis functions are already symmetrized for appropriate crystal and sample symmetries. On the other hand, the computation of the DFTs in this method is much faster compared to the GSH coefficients because of the availability of efficient Fast Fourier Transform (FFT) algorithm (Brigham, 1988a; Duhamel and Vetterli, 1990b; William H. Press, 2002; William L. Briggs, 1995). This method was applied to face-centered cubic (FCC) metals and found to speed up the crystal plasticity calculations by about an order of magnitude compared to the direct calculations (Knezevic et al., 2008a).

Another similar but more efficient spectral computation scheme has been developed to solve the crystal plasticity constitutive equations using a compact database of DFTs (Knezevic et al., 2009). In this new approach, only a small number of the terms in the DFT is used to reconstruct directly the solutions for the main functions of the conventional crystal plasticity theory for any given crystal orientation under any applied deformation mode. It should be noted that the size of the DFT dataset is essentially equal to the size of the discretized function values in their respective domain. However, here only a small fraction of the DFTs (called dominant DFTs) were found sufficient to capture the orientation dependence of the main variables. The spectral representations are again established for the same three main functions: (i) the deviatoric stress tensor $\boldsymbol{\sigma}'(\mathrm{g}, \mathbf{L})$, (ii) the lattice spin tensor $\mathbf{W}^*(\mathrm{g}, \mathbf{L})$, and (iii) the total shear rate $\sum_{\alpha}|\dot{\gamma}^{\alpha}|\,(\mathrm{g}, \mathbf{L})$. In

these functions, the independent variable g denotes the crystal lattice orientation defined using the Bunge-Euler angles $(\varphi_1, \phi, \varphi_2)$ (Bunge, 1993b), and $\mathbf{L}$ represents the velocity gradient tensor applied at the crystal level. In any time step in the simulation of the deformation process, the stress function gives the values of the deviatoric stress components at the crystal level, the spin tensor predicts the crystal rotation, and the total shear rates determine the slip hardening rates as defined in Eq. (2.7). It should be noted that latent hardening is neglected in this formulation.

In the DFT-based spectral approach, the domain of the functions of interest (i.e. the domain of the deviatoric stress tensor $\boldsymbol{\sigma}'(\mathrm{g}, \mathbf{L})$, the lattice spin tensor $\mathbf{W}^*(\mathrm{g}, \mathbf{L})$, and the total shear rate $\sum_{\alpha}|\dot{\gamma}^{\alpha}|\,(\mathrm{g}, \mathbf{L})$) is the product space of the orientation space and the deformation mode space. The crystal orientation may be described using any of the different parameterization methods such as Euler angles, Rodriguez vectors, angle-axis pairs, and quaternions. In this work, the crystal orientation is defined using the Bunge-Euler angles $(\varphi_1, \phi, \varphi_2)$ (Bunge, 1993b). All possible distinct crystal orientations under specified combination of crystal and sample symmetries are exist in a subspace (referred to as the fundamental zone, FZ) within the entire orientation space. For example, the fundamental zone of the cubic-triclinic symmetry (in this notation the first symmetry refers to crystal symmetry and the second one refers to the sample symmetry) is defined as

$$\varphi_1 \in [0, 2\pi), \phi \in \left[\cos^{-1}\left(\frac{cos\varphi_2}{\sqrt{1+\cos^2\varphi_2}}\right), \frac{\pi}{2}\right], \varphi_2 \in \left[0, \frac{\pi}{4}\right] \tag{2.12}$$

Furthermore, the deformation mode space includes the complete set of all velocity gradient tensors which can be efficiently described as (Van Houtte, 1994)

$$\mathbf{L} = \dot{\varepsilon}\,\mathbf{D}_{\mathrm{o}} + \mathbf{W}, \qquad \mathbf{D}_{\mathrm{o}} = \sum_{\mathrm{j}=1}^{3} \mathrm{D_j}\ \mathbf{e}_{\mathrm{j}}^{\mathrm{p}} \otimes \mathbf{e}_{\mathrm{j}}^{\mathrm{p}}, \qquad \dot{\varepsilon} = \frac{1}{2}|\mathbf{L} + \mathbf{L}^{\mathrm{T}}|$$

$$\mathrm{D}_1 = \sqrt{\frac{2}{3}}\cos\left(\theta - \frac{\pi}{3}\right), \quad \mathrm{D}_2 = \sqrt{\frac{2}{3}}\cos\left(\theta + \frac{\pi}{3}\right), \quad \mathrm{D}_3 = -\sqrt{\frac{2}{3}}\cos(\theta) \tag{2.13}$$

where $\{\boldsymbol{e}_i^p, i = 1,2,3\}$ denotes the principal frame of $\mathbf{D}_{\mathrm{o}}$, and the range of angular variable θ that defines all possible diagonal matrices is $\left[\frac{\pi}{6}, \frac{\pi}{2}\right)$. The spectral databases are built in the $\{\boldsymbol{e}_i^p\}$ reference frame using two primary variables, g^p and θ, where g^p denotes the crystal lattice orientation with respect to the $\{\boldsymbol{e}_i^p\}$ reference frame.

The spectral representations of the functions of interest using the new DFT-based database are expressed (Knezevic et al., 2009) as

$$\mathbf{W}_{\mathrm{rq}}^{*} = \dot{\varepsilon}\frac{1}{\mathrm{N_{g^p}}\ \mathrm{N_\theta}}\sum_{\mathrm{k}}\sum_{\mathrm{n}} \mathbf{B}_{\mathrm{kn}}\ \mathrm{e}^{\frac{2\pi\mathrm{ikr}}{\mathrm{N_{g^p}}}}\ \mathrm{e}^{\frac{2\pi\mathrm{inq}}{\mathrm{N_\theta}}} + \mathbf{W} \tag{2.14}$$

$$\boldsymbol{\sigma}'_{\mathrm{rq}} = \mathrm{s}\ \dot{\varepsilon}^{\mathrm{m}}\ \frac{1}{\mathrm{N_{g^p}}\ \mathrm{N_\theta}}\sum_{\mathrm{k}}\sum_{\mathrm{n}} \mathbf{C}_{\mathrm{kn}}\ \mathrm{e}^{\frac{2\pi\mathrm{ikr}}{\mathrm{N_{g^p}}}}\ \mathrm{e}^{\frac{2\pi\mathrm{inq}}{\mathrm{N_\theta}}} \tag{2.15}$$

$$\left(\sum_{\alpha}|\dot{\gamma}^{\alpha}|\right)_{\mathrm{rq}} = \dot{\varepsilon}\frac{1}{\mathrm{N_{g^p}}\ \mathrm{N_\theta}}\sum_{\mathrm{k}}\sum_{\mathrm{n}} \mathrm{G}_{\mathrm{kn}}\ \mathrm{e}^{\frac{2\pi\mathrm{ikr}}{\mathrm{N_{g^p}}}}\ \mathrm{e}^{\frac{2\pi\mathrm{inq}}{\mathrm{N_\theta}}} \tag{2.16}$$

where r and q enumerate the grid points in the orientation space g^p and the deformation mode space θ, respectively. The corresponding total numbers of grid points in the periodic orientation and deformation mode spaces are denoted by N_{g^p} and N_θ,

respectively. The spectral databases for the function of interest described above are stored in the form of Fourier coefficients $\mathbf{B}_{kn}$, $\mathbf{C}_{kn}$, and G_{kn} (referred to as the DFTs). In order to compute the DFTs of interest, the values of the functions of interest need to be computed on a uniform grid in their respective periodic domains. As described above, it is found that only the dominant DFTs are needed to reconstruct the values of the functions of interest with a small error compared to the direct crystal plasticity computations (Knezevic et al., 2009). This new spectral approach was found to be able to speed up the crystal plasticity calculations by about two orders of magnitude.

CHAPTER 3

CRYSTAL PLASTICITY DATABASES FOR BCC AND HCP METALS

This chapter describes the development of two spectral databases for BCC and HCP metals. These spectral databases are successfully applied to the rigid-viscoplastic polycrystal Taylor-type model to predict the texture evolution and stress-strain response for a few selected examples of deformation processes. This chapter also demonstrates the utility of these spectral databases through selected case studies that include computation of the yield surfaces and a new class of plastic property closures.

3.1 Spectral Databases for BCC Metals

A new spectral database has been developed and validated for deformation of BCC metals with 48 slip systems. The families of potential slip systems for the BCC crystals are assumed to include $\{110\}\langle\bar{1}11\rangle, \{\bar{1}12\}\langle 1\bar{1}1\rangle$, and $\{12\bar{3}\}\langle 111\rangle$. The components of the slip direction ($\mathbf{m}_0^{\alpha}$) and slip plane normal ($\mathbf{n}_0^{\alpha}$) in the initial crystal frame for these slip systems are shown in Table 3.1. The database for BCC metals includes the DFTs for the functions $\boldsymbol{\sigma}'(g^p, \theta)$, $\mathbf{W}^*(g^p, \theta)$, and $\sum_{\boldsymbol{\alpha}}|\dot{\gamma}^{\alpha}|\,(g^p, \theta)$ (see Eqs. (2.14)-(2.16)). These DFTs were computed using the same procedures that were used earlier for FCC metals (Knezevic et al., 2009). As previously mentioned, in order to compute these DFTs, the values of the functions of interest need to be computed in their entire complete respective domain. In this work, the values of the functions $\boldsymbol{\sigma}'(g^p, \theta)$, $\mathbf{W}^*(g^p, \theta)$, and $\sum_{\boldsymbol{\alpha}}|\dot{\gamma}^{\alpha}|\,(g^p, \theta)$ have been computed on a three-degree uniform grid in the

crystal orientation space and deformation mode space using the classical crystal plasticity model described in Section 2.1. The crystal orientation space is identified as $(\varphi_1 \in [0,2\pi), \phi \in [0,2\pi), \varphi_2 \in [0,2\pi))$ and the deformation mode space is identified as $\theta \in [0,2\pi)$. It should be noted that there exist several redundancies in the space identified above. However, it is selected because the values of functions of interest are periodic in this space. Therefore this space allows efficient spectral representations for the function of interests.

Table 3.1: Slip systems for BCC crystals; $\mathbf{m}_0^\alpha$ and $\mathbf{n}_0^\alpha$ denote the slip direction and the slip plane normal of the slip system α, respectively in the initial configuration.

α	$\mathbf{m}_0^\alpha$	$\mathbf{n}_0^\alpha$	α	$\mathbf{m}_0^\alpha$	$\mathbf{n}_0^\alpha$
1	-1 1 1	1 1 0	25	-1 -1 1	1 2 3
2	1 -1 1	1 1 0	26	-1 1 1	1 -2 3
3	1 1 1	-1 1 0	27	1 1 1	-1 -2 3
4	1 1 -1	-1 1 0	28	1 -1 1	-1 2 3
5	1 -1 -1	1 0 1	29	-1 -1 1	2 1 3
6	1 1 -1	1 0 1	30	-1 1 1	2 -1 3
7	1 1 1	-1 0 1	31	1 1 1	-2 -1 3
8	-1 1 -1	-1 0 1	32	1 -1 1	-2 1 3
9	-1 -1 1	0 1 1	33	-1 1 -1	2 3 1
10	1 -1 1	0 1 1	34	1 1 -1	-2 3 1
11	1 1 1	0 -1 1	35	1 1 1	-2 3 -1
12	-1 1 1	0 -1 1	36	-1 1 1	2 3 -1
13	-1 -1 1	1 1 2	37	-1 1 -1	1 3 2
14	-1 1 1	1 -1 2	38	1 1 -1	-1 3 2
15	1 1 1	-1 -1 2	39	1 1 1	-1 3 -2
16	1 -1 1	-1 1 2	40	-1 1 1	1 3 -2
17	1 1 1	-1 2 -1	41	1 -1 -1	3 2 1
18	-1 1 1	1 2 -1	42	1 -1 1	3 2 -1
19	-1 1 -1	1 2 1	43	1 1 1	3 -2 -1
20	1 1 -1	-1 2 1	44	1 1 -1	3 -2 1
21	-1 1 1	2 1 1	45	1 -1 -1	3 1 2
22	1 -1 1	2 1 -1	46	1 -1 1	3 1 -2
23	1 1 1	2 -1 -1	47	1 1 1	3 -1 -2
24	1 1 -1	2 -1 1	48	1 1 -1	3 -1 2

After calculating the values of the functions of interest over their entire respective domain, the DFTs for these functions are computed using the Fast Fourier transform algorithm (Briggs and Henson, 1995; Brigham, 1988b; Cooley and Tukey, 1965; Duhamel and Vetterli, 1990a; Press et al., 2002) in the four-dimensional space of g^p and θ. It should be underlined that the DFTs for these functions are independent of the values of g^p and θ used in the initial calculation of the functions. In other words, these DFTs can be used to reconstruct the values of the above functions for any given crystal orientation and deformation mode. Figure 3.1 (a) shows the magnitude of the DFTs (not including the zero transform) for $\sigma'_{11}(g^p, \theta)$, $W^*_{12}(g^p, \theta)$, and $\sum_\alpha |\dot{\gamma}^\alpha|\,(g^p, \theta)$ normalized by the largest transform for each component and sorted by the magnitude. It is clear from Figure 3.1 (a) that it should be possible to represent any of the three functions shown with only a few dominant DFTs with only a tolerable loss of accuracy. The accuracy of the spectral representation of the functions using only a limited number of dominant transforms was evaluated using an error metric defined as

$$e = \frac{1}{N}\sum_{i=1}^{N} \frac{\left|f_i - f_i^{DFT}\right|}{f^n} \text{ X } 100 \tag{3.1}$$

where f_i and f_i^{DFT} denote the values of the function of interest computed at N selected locations in the domain of the function using the classical crystal plasticity approach and the spectral approach described earlier (using Eqs. (2.14)-(2.16) and only the dominant DFTs), respectively, and f^n is an appropriate normalization value. In the present work, the normalization value has been taken to be three times the initial slip resistance $(3s_o)$

for the deviatoric stress components, and $(3\dot{\varepsilon})$ for the spin tensor components and the total shearing rate. The locations where the functions were evaluated included a total of 100,000 distinct combinations of g^p and θ, distributed randomly in their respective fundamental zones. The errors computed from Eq. (3.1) for $\sigma'_{11}(g^p, \theta)$, $W^*_{12}(g^p, \theta)$, and $\sum_{\alpha}|\dot{\gamma}^{\alpha}|\,(g^p, \theta)$ are plotted against the number of dominant DFTs retained in the computation of f_i^{DFT} in Figure 3.1 (b). The average error when using 500 dominant DFTs was less than 2% for all of these three components. Similar results were also obtained for all the five independent components of the deviatoric stress function and the three independent components of the spin function studied here. It was also observed that the errors noted here for the DFT-based spectral databases for BCC metals were lower than the corresponding errors for FCC metals (Knezevic et al., 2009). For example, when using 500 dominant DFTs for the deviatoric stress component $\sigma'_{11}(g^p, \theta)$ with the FCC database, the corresponding error was about 2.5%, while it is around 1.5% for the BCC database developed here. The more compact representation of the functions for BCC crystals obtained here is attributed to the availability of many more potential slip systems, compared to the FCC crystals. The availability of the larger number of slip systems results in the functions of interest becoming more uniform in their respective domains, and therefore needs lesser numbers of dominant DFTs to achieve the desired accuracy.

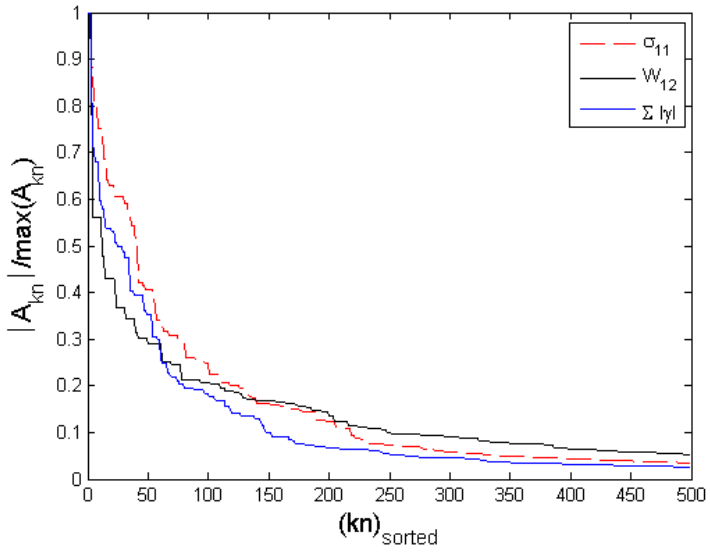

(a)

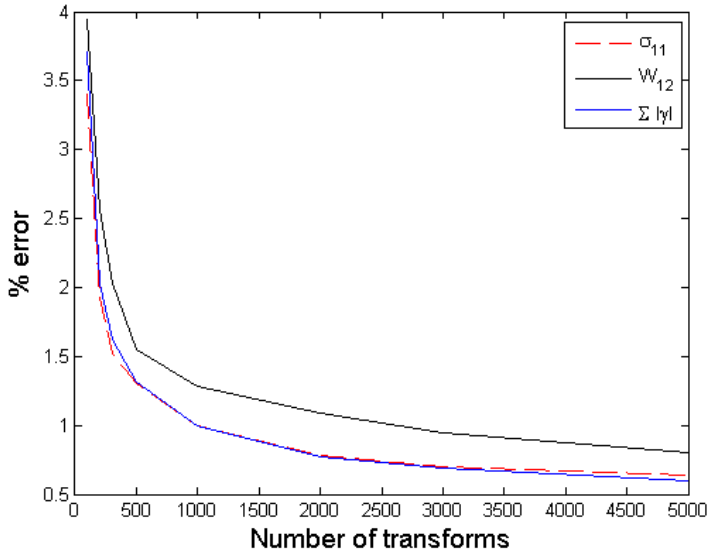

(b)

Figure 3.1: (a) Magnitudes of dominant transforms (not including the zero transform) normalized by the largest value and sorted by magnitude for the components $\sigma'_{11}(g^p, \theta)$, $W^*_{12}(g^p, \theta)$, and $\sum_\alpha |\dot{\gamma}^\alpha|(g^p, \theta)$, where A_{kn} here indicates the dominant DFTs. (b) Average percentage error for the same three components computed using Eq. (3.1) for different numbers of dominant DFTs retained in the computations for 100,000 combinations of selected orientations and deformation modes.

The new BCC spectral database developed here was validated by comparing the predicted stress-strain curves and deformed textures against the corresponding results from the conventional crystal plasticity computations for different deformation processes with different initial textures. The predictions from the two approaches are based on the simple Taylor-type polycrystal model. The slip hardening parameters used in these simulations were those established previously for interstitial-free (IF) steel by curve fitting the Taylor predictions to experimental measurements (Peeters et al., 2001). The values of these slip hardening parameters were $h_o = 500$ MPa, $s_s = 230$ MPa, $a = 2.80$, and $s_0 = 50$ MPa. As an example, the predicted texture and stress-strain curves for a polycrystalline IF steel deformed by simple shear to a shear strain of $\gamma = 0.6$ using the conventional computational approach and the new DFT spectral approach developed here are shown in Figure 3.2. The initial texture in the sample was captured using a set of 1200 discrete crystal orientations (Peeters et al., 2001). The DFT-based predictions used 500 dominant DFTs for the stress, the shearing rate, and the lattice spin components. It is clear that the DFT-based databases developed here for BCC crystals produce excellent predictions, and these are obtained at a significant faster computational speed. The simulation time was 130 seconds for the conventional calculations, and only 2.9 seconds for the spectral approach using dominant DFTs. The computations were performed on a Pentium 4 desktop PC.

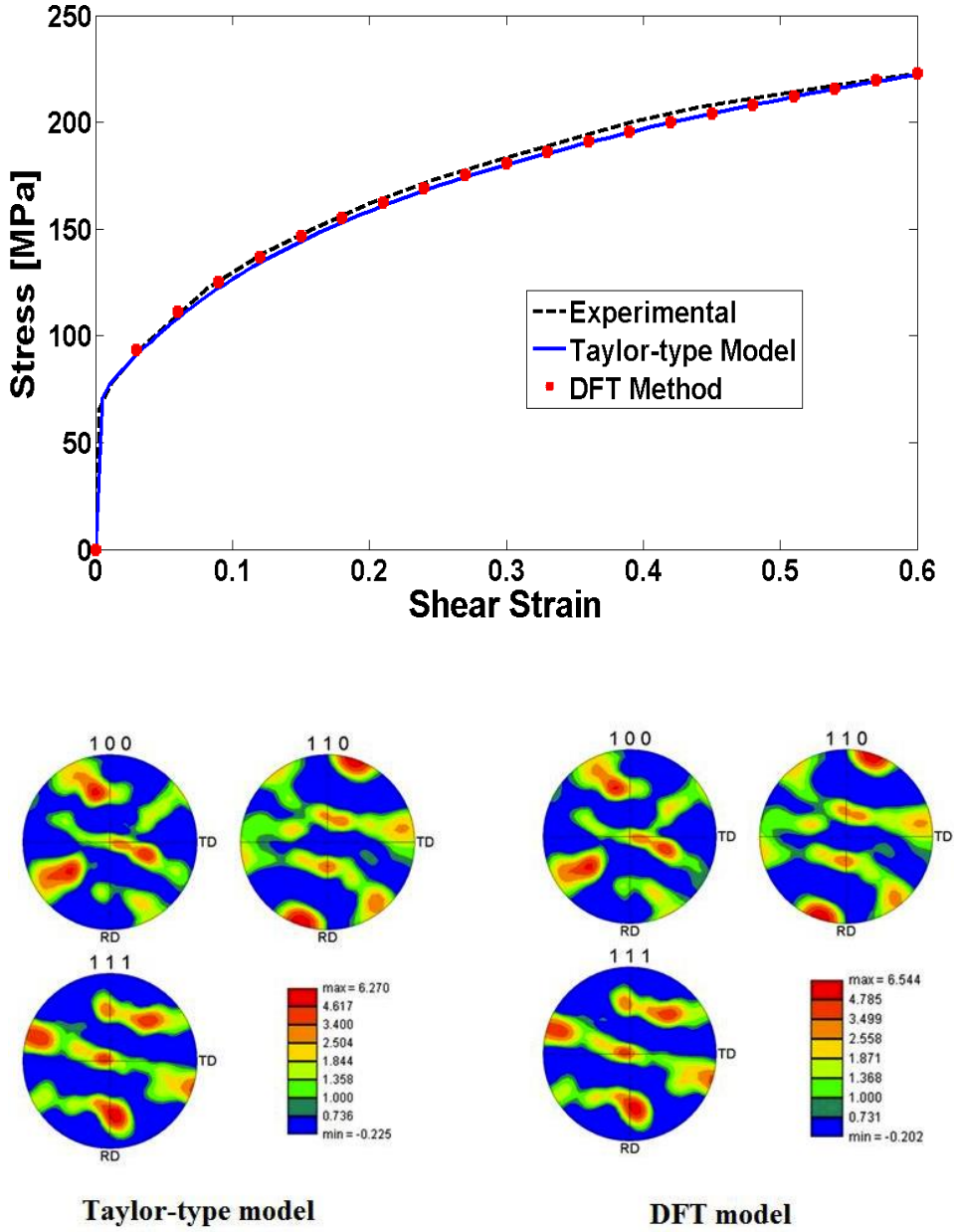

Figure 3.2: Comparison of the predicted stress-strain curves (top) and pole figures (bottom) from the spectral database (using 500 DFTs for the stress, the shearing rate, and the lattice spin components) against the corresponding predictions from the conventional approach for simple shear of IF steel.

Another validation of the BCC spectral database was carried out by simulating plane strain compression on polycrystalline IF-steel to a true strain of $\varepsilon = -1.0$. The initial texture was assumed to be random consisting of 1000 discrete crystal orientations. The stress-strain response and the deformed texture computed from the new DFT spectral approach, using only 300 dominant DFTs for the stress, the shearing rate, and the lattice spin components, are compared against the corresponding predictions from the traditional crystal plasticity approach as shown in Figure 3.3. It is clear that the two predictions are in excellent agreement with each other. For this case study, the simulation took 110 seconds using the conventional calculations, but only 2.1 seconds using the spectral approach using dominant DFTs.

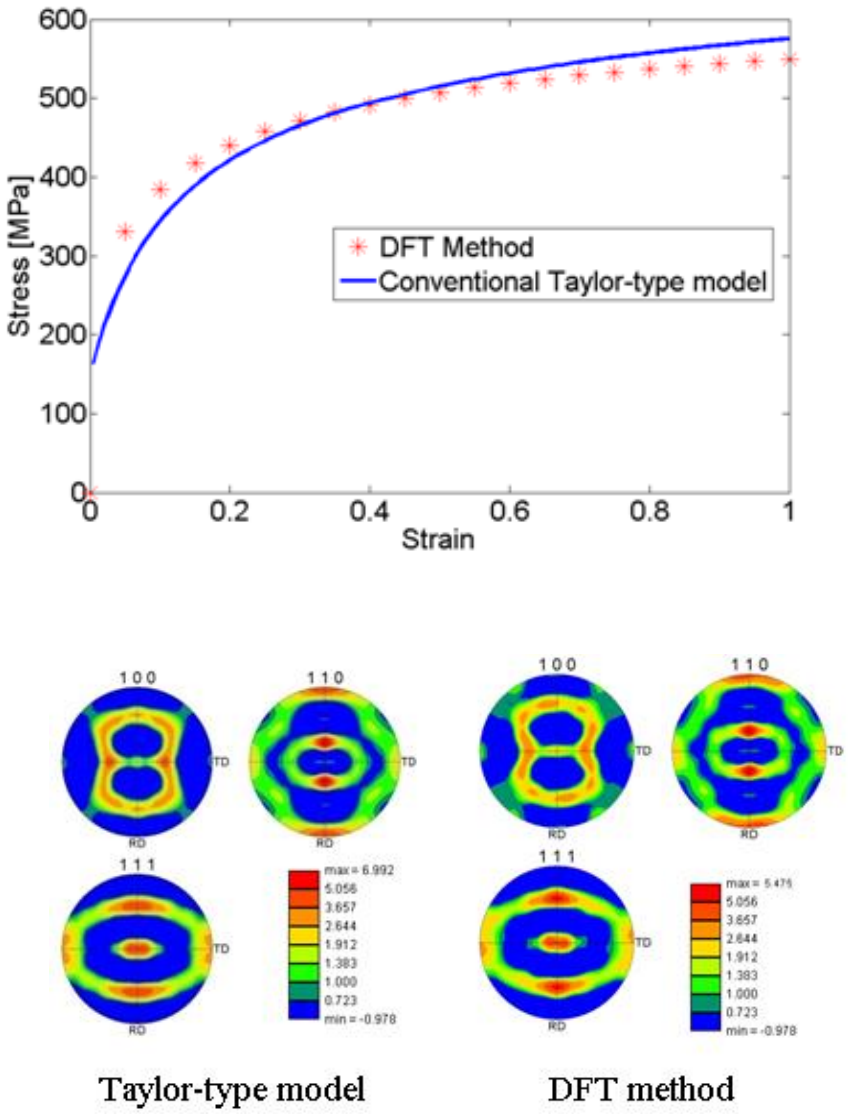

Figure 3.3: Comparison of the predicted stress-strain curves (top) and pole figures (bottom) from the spectral database (using 500 DFTs for the stress, the shearing rate, and the lattice spin components) against the corresponding predictions from the conventional approach for plane strain compression of IF steel.

3.2 Spectral Databases for HCP Metals

Following the approach described earlier, new spectral databases have been developed for HCP metals assuming that the material deform solely by slip. Although twining is an important deformation mechanism and often observed in HCP metals such as magnesium and pure titanium (Christian and Mahajan, 1995; Chun et al., 2005; Knezevic et al., 2010; Levinson et al., 2013; Nemat-Nasser et al., 1999; Salem et al., 2003; Salem et al., 2005; Zeng et al., 2009), some other important HCP metals like Ti-Al alloys are mainly deformed by slip (Conrad, 1981; Williams et al., 2002; Zaefferer, 2003). The families of potential slip systems for HCP crystals are assumed to include the prismatic $\{10\bar{1}0\}\langle 11\bar{2}0\rangle$, basal $\{0001\}\langle 11\bar{2}0\rangle$, and pyramidal $\{10\bar{1}1\}\langle 11\bar{2}3\rangle$ slip systems as shown in Table 3.2. These families of slip systems can have different critical resolved shear stress values because of the low symmetry in HCP crystals. In this work, two different slip resistance ratios that are reported in the literature for Ti-6Al-4V were used to generate the spectral databases. The first slip resistance ratio was taken to be 1:0.75:3.0 in the basal, prism, and pyramidal slip systems respectively (BIELER, 2001). The second slip resistance ratio was taken to be 1:1.5:2.0:1.8:1.3:1.3:3.0 in the prism (a1), prism (a2), prism (a3), basal (a1), basal (a2), basal (a3), and pyramidal (c+a) slip systems respectively (Salem and Semiatin, 2009). The spectral databases developed in this section for these two slip resistance ratios will be hereafter referred to as HCP slip ratio A database and HCP slip ratio B database, respectively.

Table 3.2: Slip systems for HCP metals used in this work for developing the HCP databases.

No.	Slip plane	Slip direction	Slip system ID
1	0 0 0 1	-2 1 1 0	Basal a1
2	0 0 0 1	1 -2 1 0	Basal a2
3	0 0 0 1	1 1 -2 0	Basal a3
4	0 1 -1 0	-2 1 1 0	Prism a1
5	1 0 -1 0	1 -2 1 0	Prism a2
6	1 -1 0 0	1 1 -2 0	Prism a3
7	0 1 -1 1	-1 2 -1 -3	Pyramidal <c+a>
8	0 1 -1 1	1 1 -2 -3	Pyramidal <c+a>
9	1 0 -1 1	2 -1 -1 -3	Pyramidal <c+a>
10	1 0 -1 1	1 1 -2 -3	Pyramidal <c+a>
11	1 -1 0 1	2 -1 -1 -3	Pyramidal <c+a>
12	1 -1 0 1	1 -2 1 -3	Pyramidal <c+a>
13	0 -1 1 1	1 -2 1 -3	Pyramidal <c+a>
14	0 -1 1 1	-1 -1 2 -3	Pyramidal <c+a>
15	-1 0 1 1	-2 1 1 -3	Pyramidal <c+a>
16	-1 0 1 1	-1 -1 2 -3	Pyramidal <c+a>
17	-1 1 0 1	-1 2 -1 -3	Pyramidal <c+a>
18	-1 1 0 1	-2 1 1 -3	Pyramidal <c+a>

The spectral representations were established for the functions $\boldsymbol{\sigma}'(g^p, \theta)$, $\mathbf{W}^*(g^p, \theta)$, and $\sum_{\alpha}|\dot{\gamma}^{\alpha}|\,(g^p, \theta)$ (se Eqs. (2.14)-(2.16)). It should be noted that the total shear rates here is the sum of the shearing rates on all basal, prism, and pyramidal slip systems. For simplicity, we assumed here that the ratio of the slip resistance between the different slip system families remains constant. In order to allow for different hardening on the different slip systems, one needs to keep track of the shearing rates on the different slip systems individually. The same procedure described earlier was followed to compute the DFTs for the functions of interest. Figures 3.4 shows the magnitude of the DFTs (not including the zero transform) for the components $\sigma'_{11}(g^p, \theta)$, $W^*_{12}(g^p, \theta)$, and $\sum_{\alpha}|\dot{\gamma}^{\alpha}|\,(g^p, \theta)$ normalized by the largest transform and sorted by the magnitude for the two spectral HCP databases developed in this study (HCP slip ratios A and B databases). It can be seen from Figures 3.4 that the values of the functions of interest can be captured with only a few dominant DFTs. The average percentage error between the classical crystal plasticity and the spectral approach using HCP slip ratio A database based on 500 dominant DFTs was about 3.4 % for the deviatoric stress component $\sigma'_{11}(g^p, \theta)$ using Eq. (3.1). Several other similar results were obtained for the other components using slip ratio A and B databases.

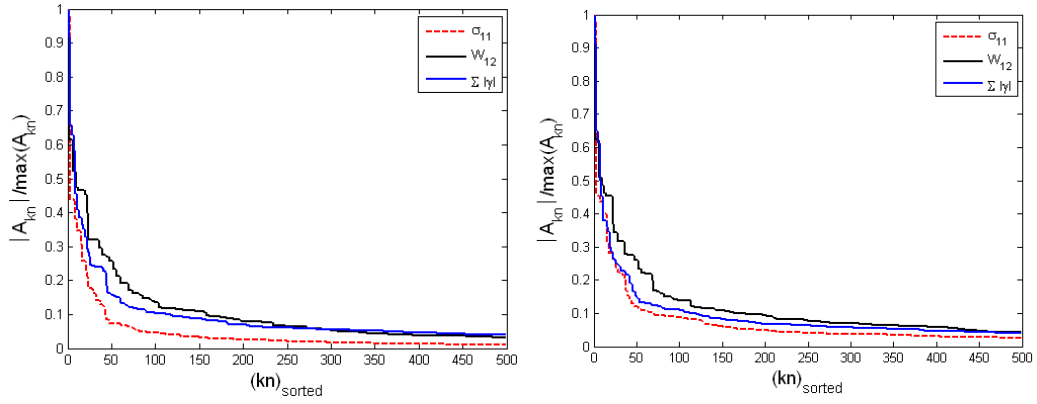

Figure 3.4: Magnitudes of dominant transforms (not including the zero transform) normalized by the largest value and sorted by magnitude for the components $\sigma'_{11}(g^p, \theta)$, $W^*_{12}(g^p, \theta)$, and $\sum_\alpha |\dot{\gamma}^\alpha| (g^p, \theta)$, where A_{kn} here indicates the dominant DFTs: (a) HCP slip ratio A, and (b) HCP slip ratio B.

In order to validate the HCP spectral databases developed in this work, we simulated plane strain compression on polycrystalline titanium alloy to a true strain of -1.0 along the compression axis. The polycrystal was assumed to possess a random initial texture captured by a set of 1000 discrete crystal lattice orientations as shown in Figure 3.5. We used two different ratios for the slip resistance to validate HCP slip ratio A database and HCP slip ratio B database. For the first material (called titanium alloy A), the values of the slip resistance for the basal, prism, and pyramidal slip systems were taken as 49.2 MPa, 36.9 MPa, 147.6 MPa, respectively (BIELER, 2001). On the other hand, titanium alloy B was assumed to have the following slip resistance values: 44.0 MPa, 66.01 MPa, 88.0 MPa, 79.2 MPa, 57.2 MPa , 57.2 MPa, 132.0 MPa for the prism

(a1), prism (a2), prism (a3), basal (a1), basal (a2), basal (a3), and pyramidal (c+a) slip systems, respectively (Salem and Semiatin, 2009). It is assumed that there is no hardening prescribed in the material response for this simulation. The value of the strain rate sensitivity parameter was taken as 0.02.

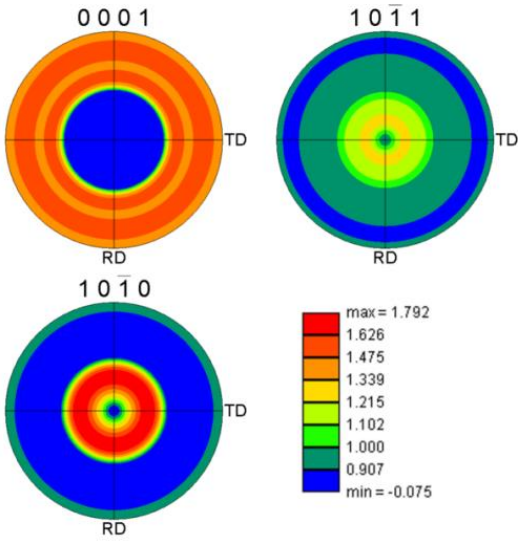

Figure 3.5: Initial random texture used in this case study for titanium alloy.

The predictions from the spectral approach to crystal plasticity calculations using both HCP ratio A and B databases developed here were compared against the corresponding predictions from the classical crystal plasticity approach. The Taylor-type assumption is used here to obtain the response of the polycrystalline aggregate. The deformed texture and stress-strain curves for titanium alloy A using the conventional crystal plasticity and the spectral crystal approach (using HCP slip ratio A database based on 500 dominant transforms for the stress, the shearing rate, and the lattice spin components) are shown in Figures 3.6 and 3.7, respectively. The predicted results for

titanium alloy B using both HCP slip ratio B database (based on 500 dominant transforms for the stress, the shearing rate, and the lattice spin components) and the classical approach are shown in Figures 3.8 and 3.9. It is clear that the DFT-based approach provide excellent predictions at a significantly faster computational speed. The simulation took about 148 seconds on a regular PC for the conventional Taylor-type calculations, but only 11 seconds for the DFT-based spectral methods using 500 dominant transforms.

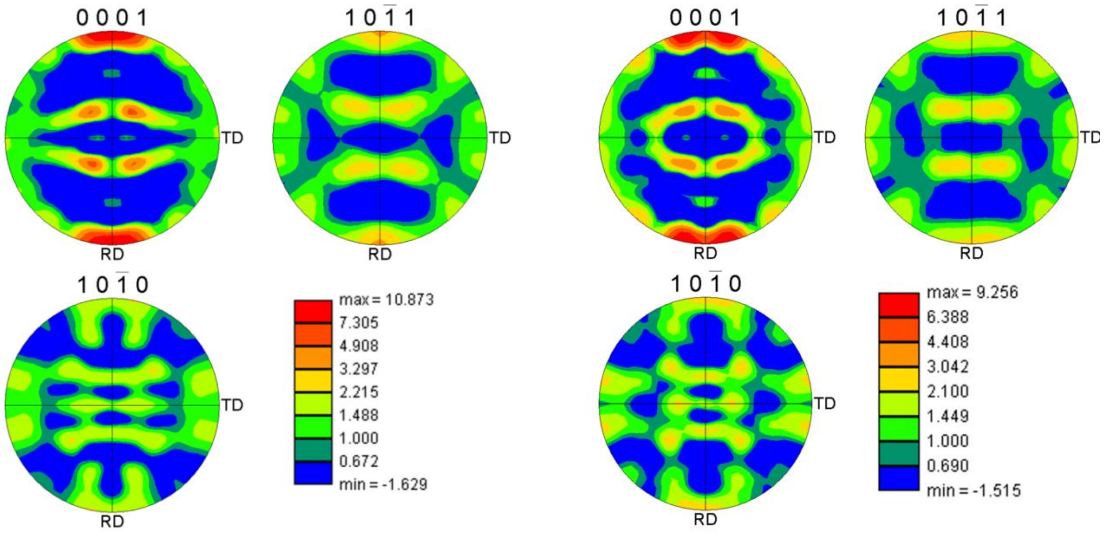

(a) (b)

Figure 3.6: Predicted pole figures for plane strain compression of titanium alloy A after a true strain of -1.0 using (a) the conventional crystal plasticity approach, and (b) the spectral approach using HCP slip ratio A database based on 500 DFTs for the stress, the shearing rate, and the lattice spin components.

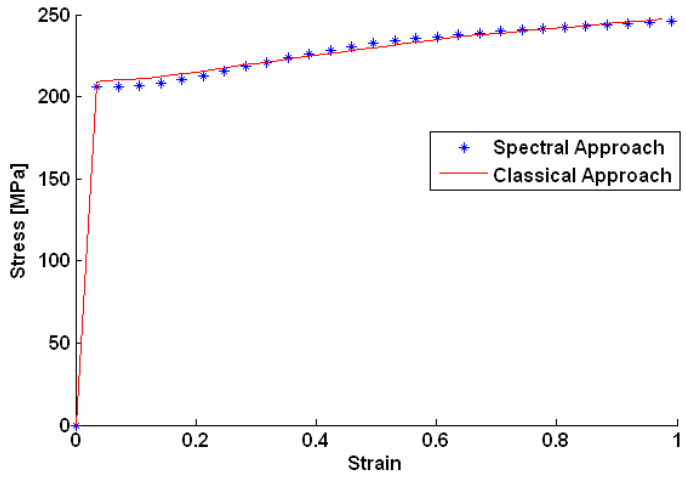

Figure 3.7: Comparison of the predicted stress-strain curves from the spectral method using HCP slip ratio A database (based on 500 dominant DFTs for the stress components, shearing rate, and the lattice spin components) against the corresponding result from the classical Taylor-type model for plane strain compression of titanium alloy A.

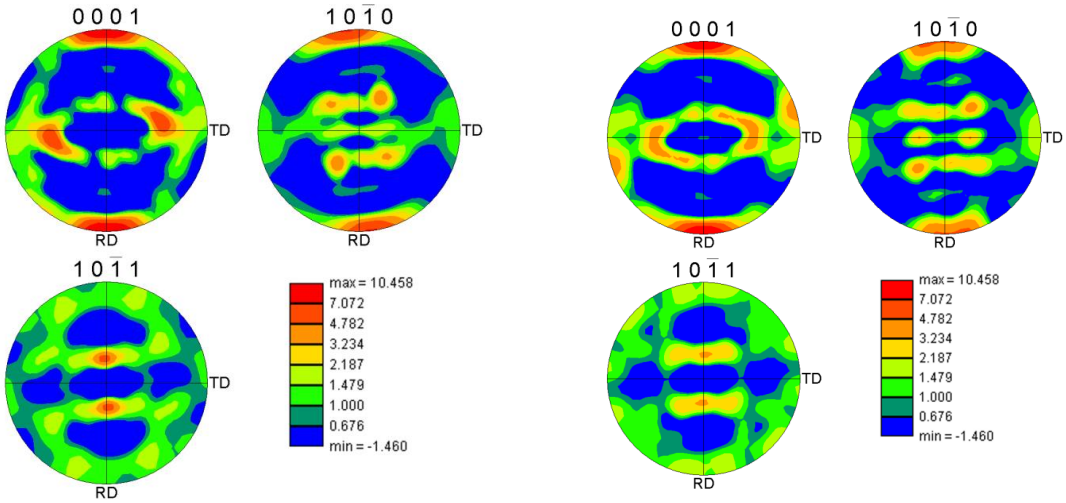

(a) (b)

Figure 3.8: Predicted pole figures for plane strain compression of titanium alloy B after a true strain of -1.0 using (a) the conventional crystal plasticity approach, and (b) the spectral approach using HCP slip ratio B database based on 500 DFTs for the stress, the shearing rate, and the lattice spin components.

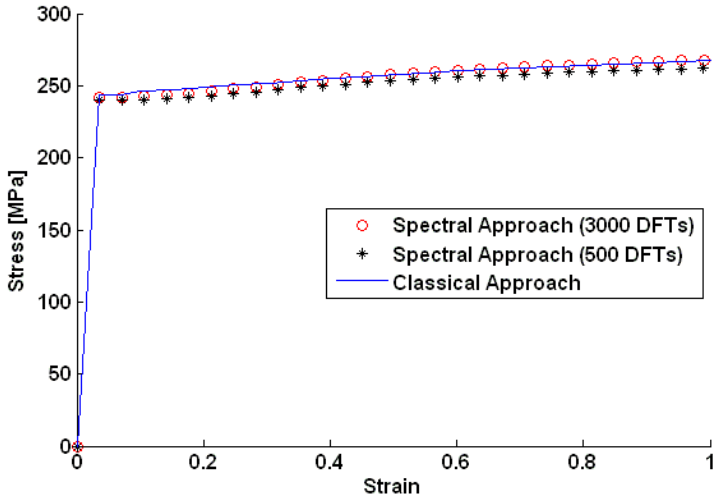

Figure 3.9: Comparison of the predicted stress-strain curves from the spectral method, using HCP slip ratio B database based on 500 and 3000 dominant DFTs for the stress components, shearing rate, and the lattice spin components, against the corresponding predictions from the classical Taylor-type model for plane strain compression of titanium alloy B.

3.3 Applications of Spectral Databases: Fast Computation of Yield Surfaces and Plastic Property Closures

This section demonstrates some of the computational advantages of the DFT-based spectral databases in two important applications. First, a new efficient methodology for the fast computation of the yield surfaces in the five-dimensional deviatoric stress space for both FCC and BCC metals is developed based on the Taylor polycrystal plasticity models. Second, a new class of first-order plastic property closures for both FCC and BCC metals is produced for the first time without invoking any simplifying assumptions regarding sample symmetry. Both of these points are explained in more details next.

3.3.1 Fast Computation of Yield Surfaces using Spectral Databases

It is computationally very expensive to establish the anisotropic yield surface for polycrystalline materials using crystal plasticity constitutive equations. For example, in order to evaluate the stress values on the yield surface, one needs to calculate the effective stress values of the polycrystalline aggregate for all possible deformation modes in the strain rate space. This entails extremely long computation times. A new efficient method has been developed to delineate the yield surface in the five-dimensional deviatoric stress space for both FCC and BCC metals based on the Taylor polycrystal plasticity models. The fast computation of the entire five-dimensional yield surface has been made possible due to the spectral representations of the stress function (see Eq. (2.15)) and the orientation distribution function (ODF) (Bunge, 1993a). A brief review of the ODF and its spectral representation is explained next.

The ODF, also referred to as texture, is used to capture the distribution of the crystal lattice orientations in a polycrystalline sample. It reflects the normalized probability density associated with occurrence of the crystallographic orientation, g, in the sample. ODF, denoted as $f(\mathrm{g})$, is formally defined as

$$f(\mathrm{g})\, d\mathrm{g} = \frac{N_{\mathrm{g}\pm \mathrm{dg}/2}}{N}, \qquad \int_{FZ} f(\mathrm{g})\, d\mathrm{g} = 1 \tag{3.2}$$

where N is the total number of orientations measured in the sample, $N_{\mathrm{g}\pm \mathrm{dg}/2}$ is the number of orientations that lie within an invariant measure $d\mathrm{g}$ centered about the orientation g, and FZ denotes the fundamental zone of distinct orientations in a suitable defined orientation space. The orientation, g, is defined here using the three Bunge-Euler angles $\mathrm{g} = (\varphi_1, \phi, \varphi_2)$ (Bunge, 1993b). The invariant measure is then defined as

$$\mathrm{dg} = \sin\phi \; \mathrm{d}\varphi_1 \mathrm{d}\phi \; \mathrm{d}\varphi_2 \tag{3.3}$$

The spectral representation of the ODF was suggested first by Bunge (Bunge, 1993a) using Generalized Spherical Harmonics (GSH) functions as

$$f(\mathrm{g}) = \sum_{l=0}^{\infty} \sum_{\mu=1}^{M(l)} \sum_{\nu=1}^{N(l)} F_l^{\mu\nu}\, \dot{\dot{T}}_l^{\mu\nu}(\mathrm{g}) \tag{3.4}$$

where $\dot{\dot{T}}_l^{\mu\nu}(\mathrm{g})$ represent the symmetrized GSH functions and $F_l^{\mu\nu}$ denote the Fourier coefficients. The discrete representation of the ODF can be also established using DFT as (Kalidindi et al., 2009)

$$\mathrm{f}_b = \sum_k F_{\mathrm{k}}\, \mathrm{e}^{\frac{2\pi \mathrm{i} \mathrm{k} \mathrm{b}}{\mathrm{N_g}}} \tag{3.5}$$

where f_b represents the value of ODF at the grid point in the orientation space enumerated by b, and F_{k} denotes the DFTs for the ODF calculated as

$$\mathrm{F_k} = \sum_b \mathrm{f}_b \sin\phi_b\, \mathrm{e}^{\frac{-2\pi \mathrm{i} \mathrm{k} \mathrm{b}}{\mathrm{N_g}}} \tag{3.6}$$

The new approach developed here to efficiently compute the yield surface relies on the spectral representations of the ODF (Eq. (3.5)) and the stress function (Eq. (2.15)). The orthogonal property of the DFTs allows calculating the volume-averaged value of the local stress tensors via simple multiplications of the Fourier coefficients for the stress function and ODF. Thus, the effective stress values of the polycrystalline aggregate based on the Taylor model can be efficiently calculated as

$$\bar{\boldsymbol{\sigma}}'_{\mathrm{q}} = \mathrm{s}\, \dot{\varepsilon}^{\mathrm{m}}\, \mathrm{sgn}(\dot{\varepsilon}) \frac{1}{\mathrm{N_g N_\theta}} \sum_{\mathrm{k}} \sum_{\mathrm{n}} \mathrm{F_k}\ \mathbf{C}_{\mathrm{kn}}\ \mathrm{e}^{\frac{2\pi \mathrm{i} \mathrm{n} \mathrm{q}}{\mathrm{N_\theta}}} \tag{3.7}$$

where $\bar{\boldsymbol{\sigma}}'_{\mathrm{q}}$ denotes the components of the volume averaged deviatoric stress tensor for certain deformation mode θ, enumerated by q. $\mathbf{C}_{\mathrm{kn}}$ and $\mathrm{F_k}$ denote the DFTs for the stress function and ODF, respectively. Using this relation, the values of the deviatoric stresses on the yield surface for a selected choice of the principle frame of **D** can be computed by exploring all possible deformation modes using the angular variable θ. To establish the entire yield surface on the sample frame, one needs to explore the space of all possible principle frames. The space of all possible principle frames can be identified using a set

of three Euler angles that relate the sample frame to the principle frame. It should be noted that only a small number of DFTs for the stress function ($\mathbf{C}_{\mathrm{kn}}$) needs to be used in Eq. (3.7). This leads to a very efficient computation of the effective deviatoric stress tensor.

This approach has been used successfully to construct the complete five-dimensional yield surface for both FCC and BCC polycrystalline materials. For BCC metals, the families of 48 potential slip systems are assumed to include $\{110\}\langle\bar{1}11\rangle$, $\{\bar{1}12\}\langle 1\bar{1}1\rangle$, and $\{12\bar{3}\}\langle 111\rangle$. The spectral database described earlier for BCC metals is used in this example (Al-Harbi et al., 2010). Figure 3.10 (a) represents a selected projection of the five-dimensional yield surface computed here for IF-steel using 500 dominant DFTs. The material was assumed to possess a random texture described by a set of 1000 discrete crystal orientations. The time required for computing the entire five-dimensional yield surface (involving computations of the values of 7,200,000 stress tensors) was only 170 seconds. In order to check the accuracy of the yield surface, the $(\sigma_{11}, \sigma_{22})$ section of the IF-steel yield surface computed using 500 dominant DFTs was compared against the one computed using the conventional approach as shown in Figure 3.10 (b). It is clear that the DFT-based computations are in excellent agreement with the conventional computations.

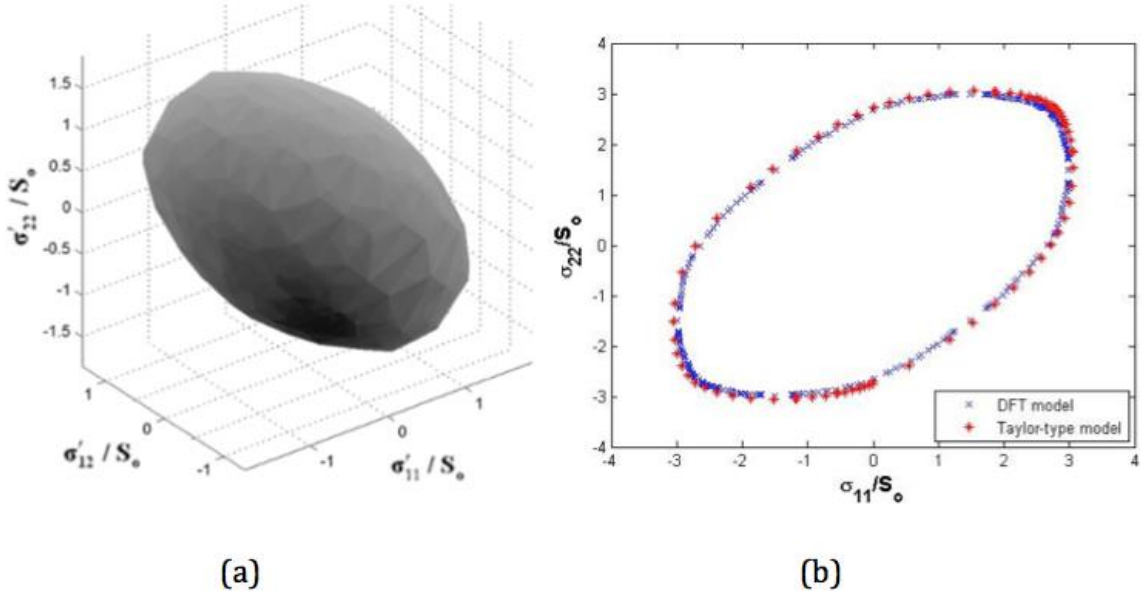

(a) (b)

Figure 3.10: (a) Three-dimensional projection of the yield surface computed using the DFT-based spectral method for IF-steel with a random texture; (b) plots of the predicted $(\boldsymbol{\sigma_{11}}, \boldsymbol{\sigma_{22}})$ −yield locus for the same material comparing the spectral approach with the conventional Taylor approach.

The new spectral approach described here for computing the yield surface is also applied to FCC metals. For FCC metals, the family of twelve $\{111\}\langle 1\bar{1}0\rangle$ slip systems are assumed to be the potential slip systems for plastic deformation. The components of the slip direction $(\mathbf{m}_0^{\alpha})$ and slip plane normal $(\mathbf{n}_0^{\alpha})$ in the initial crystal frame for these slip systems are shown in Table 3.3. In this example, the spectral database developed and validated in prior work for FCC metals is used (Knezevic et al., 2009). Figure 3.11 shows the yield loci in the π-plane for polycrystalline copper computed using 500 dominant DFTs from the FCC database and the corresponding predictions from the conventional calculations. In this example, the metal was assumed to possess a texture that is typically

observed in rolled FCC samples. This texture was described by a set of 1000 discrete orientations, which was obtained by simulating plane strain compression to a true strain of -1.0 on an initially random texture. It was seen once again that the DFT method can reproduce all of the features of the conventional computations for this strongly textured sample.

Table 3.3: Slip systems for FCC crystals; $\mathbf{m}_0^\alpha$ and $\mathbf{n}_0^\alpha$ denote the slip direction and the slip plane normal of the slip system α, respectively in the initial configuration.

α	$\mathbf{m}_0^\alpha$	$\mathbf{n}_0^\alpha$
1	1 -1 0	1 1 1
2	1 0 -1	1 1 1
3	0 1 -1	1 1 1
4	1 0 1	-1 1 1
5	1 1 0	-1 1 1
6	0 1 -1	-1 1 1
7	1 0 -1	1 -1 1
8	0 1 1	1 -1 1
9	1 1 0	1 -1 1
10	1 -1 0	1 1 -1
11	1 0 1	1 1 -1
12	0 1 1	1 1 -1

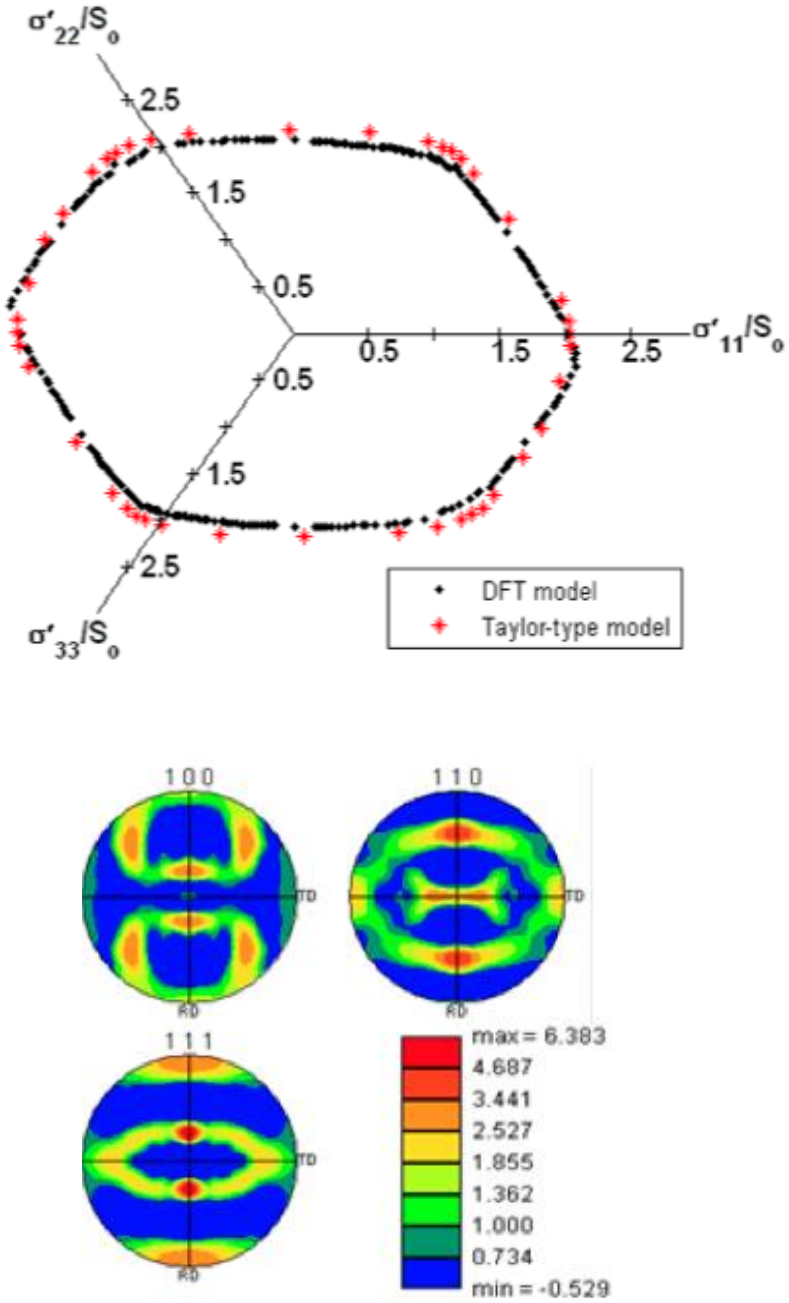

Figure 3.11: Plots of yield surface on the π-plane (top) computed using the spectral methods and the conventional approach for polycrystalline FCC copper. The texture (bottom) in the sample was assumed to be representative of textures found in rolled FCC samples.

3.3.2 Plastic Property Closures for Cubic-Triclinic Textures

Property closures define the complete space of all possible selected combinations of effective properties in a given material system for a selected homogenization theory (Adams et al., 2001; Adams et al., 2004; Fast et al., 2008; Fullwood et al., 2007; Houskamp et al., 2007; Kalidindi et al., 2006a; Kalidindi et al., 2004b; Knezevic and Kalidindi, 2007; Lyon and Adams, 2004; Proust and Kalidindi, 2006; Wu et al., 2007). The elastic-plastic property closures of polycrystalline materials are of great interest in the design of new materials with enhanced properties. The property closure is essentially obtained by mapping every possible microstructure in a given material system into the corresponding properties of interest in the property space. It is computationally very expensive to construct the property closures for polycrystalline materials using physics-based models.

The first-order property closures are established based on the first-order statistics of the material microstructure (Knezevic and Kalidindi, 2007; Knezevic et al., 2008b; Proust and Kalidindi, 2006; Wu et al., 2007). For polycrystalline materials, the first-order statistics of microstructure is generally described using the crystallographic texture (also called orientation distribution function or ODF), also referred to as texture. Thus, the first-order property closures in polycrystalline materials are essentially obtained by mapping all possible textures into the selected property spaces of interest. It should be noted that the complete set of all theoretically possible textures, referred to as texture hull, can be conveniently expressed using the Fourier representations of the texture (see Eqs. (3.4)-(3.6)) (Adams et al., 2001; Kalidindi et al., 2009; Proust and Kalidindi, 2006; Wu et al., 2007). Several optimization techniques have been used to construct the

property closures including the gradient methods (Proust and Kalidindi, 2006), Pareto-front methods (Fullwood et al., 2007), and genetic-like algorithm (Knezevic et al., 2008b).

The delineation of plastic property closures for polycrystalline materials using crystal plasticity theories, which take into account the effect of texture, entails long computation times. Therefore, all of the previously reported plastic property closures have been established for polycrystalline materials that exhibit orthorhombic sample symmetry. This is mainly because of the high computational cost associated with evaluating the effective plastic properties using crystal plasticity theories without the simplifying assumption of sample symmetry. To illustrate this point, consider the evaluation of the typical plastic properties of interest, such as uniaxial yield strength, using crystal plasticity models. In order to establish these plastic properties, it is necessary to guess the imposed deformation mode that would correspond to the stress state of interest. Without any simplifying assumption of sample symmetry, this search has to take place over the entire domain of the deformation mode. This is essentially equivalent to the computation of the entire yield surface. However, it will become much easier to evaluate some of the plastic properties of interest under the assumption of orthorhombic sample symmetry. For example, in evaluating the uniaxial yield strength with the assumption of orthorhombic sample symmetry, the following macroscopic velocity gradient is commonly imposed

$$\mathbf{L} = \dot{\varepsilon}\begin{bmatrix} 1 & 0 & 0 \\ 0 & -\mathrm{q} & 0 \\ 0 & 0 & -(1-\mathrm{q}) \end{bmatrix} \tag{3.8}$$

where the single parameter q can take any value between 0 and 1. The effective tensile yield strength is calculated by adjusting the value of q (denoted as q^*) such that the lateral deviatoric stresses over the polycrystal are equal to each other (i.e. $\sigma'_{22}(q^*) = \sigma'_{33}(q^*)$). Then, the tensile yield strength in the e_1 direction is simply given by

$$\sigma_{y1} = \sigma'_{11}(q^*) - \sigma'_{22}(q^*) \tag{3.9}$$

For cubic-triclinic textures (in this notation the first symmetry refers to crystal symmetry and the second one refers to the sample symmetry), the typical plastic properties of interest are most conveniently computed by establishing the yield surface. However, the computation of the yield surface for polycrystalline materials using crystal plasticity constitutive equations is computationally very expensive.

The new efficient methodology for the fast computation of the yield surface described in the previous section has been utilized to construct the first-order plastic property closures for cubic polycrystalline materials without assuming any sample symmetry (i.e. cubic-triclinic symmetry). It is emphasized here that the highly efficient computation of the yield surface is obtained by using the DFT databases. Several plastic property closures have been constructed for cubic-orthorhombic and cubic-triclinic textures for both FCC and BCC metals based on the Taylor-type model. The genetic-like algorithm (Knezevic et al., 2008b) has been followed here for building the first-order plastic closures. In the genetic-like algorithm, the property combinations of interest are first evaluated for a set of crystal orientations that are uniformly distributed over the crystal orientation space. Then, weighted combinations of crystal orientations located on

the boundary are used to expand the property closure. The process is repeated until the closure does not expand any more.

One of the goals of this study is to quantify the expected increase in the plastic property closures, and the potential design spaces, by relaxing the assumption of orthorhombic sample symmetry. In this work, two plastic property closures were computed for both FCC copper and BCC IF-steel. Figure 3.12 shows the first-order closures delineating all of the feasible combinations of the normalized yield strengths in the sample $\mathbf{e}_1$ and $\mathbf{e}_2$ directions (i.e. σ_{y1} and σ_{y2}) for copper and IF-steel computed assuming both orthorhombic and triclinic sample symmetries. Figure 3.12 clearly indicates that some combinations of σ_{y1} and σ_{y2} cannot be attained with the cubic-orthorhombic textures. Comparison of the closures in Figure 3.12 (a) and Figure 3.12 (b) reveals that the difference between the cubic-orthorhombic and the cubic-triclinic property closures is considerably larger for FCC metals compared to BCC metals. This observation is attributed to the availability of the higher number of slip systems in the BCC metals (48 slip systems in BCC compared to only 12 in the FCC crystals). The higher number of slip systems are expected to lower the degree of anisotropy in the response of the BCC metals, and should therefore reduce the difference between cubic-orthorhombic and cubic-triclinic closures for these metals compared to the FCC metals.

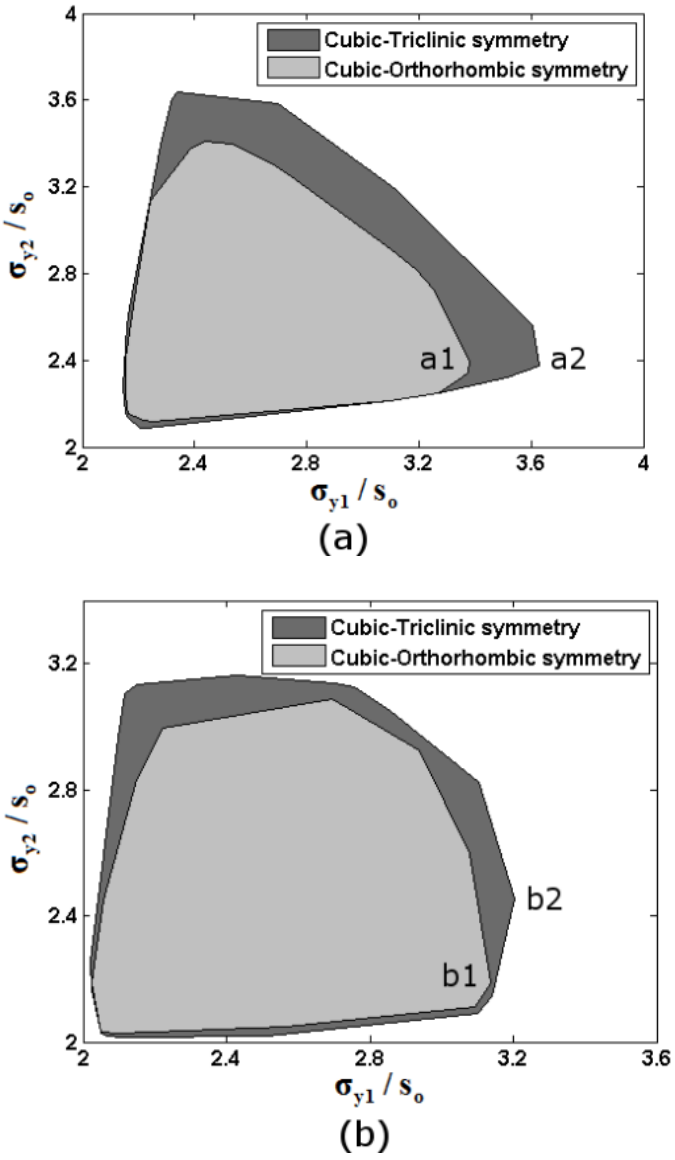

Figure 3.12: First-order cubic-triclinic and cubic-orthorhombic plastic closures for $(\sigma_{y1}/s_o, \sigma_{y2}/s_o)$ computed using the DFT-based methods developed in this work. (a) OFHC Copper, (b) IF-steel.

Textures corresponding to the highest values of the tensile yield strengths in Figure 3.12 (a) and Figure 3.12 (b) are depicted in Figure 3.13. It is seen that the highest tensile strength for copper was obtained for a single crystal oriented close to the $(111)[1\bar{1}\bar{1}]$ orientation. However, this single crystal is not represented in the cubic-orthorhombic closure. The highest tensile yield strength in the cubic-orthorhombic closure, based on the Taylor model used here, is obtained by a crystalline aggregate comprising of four equi-volume crystals that are close to the $(110)\langle 111\rangle$ orientations. Note that the highest possible tensile yield strength in the orthorhombic closure (for the aggregate comprising four equi-volume crystals) is 7% lower than the corresponding optimum solution in the triclinic closure (for the single crystal). For IF-steel, the orientation corresponding to the highest yield strength was found to be the $(132)[\bar{1}1\bar{1}]$ orientation, whereas the highest yield strength with orthorhombic sample symmetry corresponded to a texture that may be visualized as (111) fiber texture with the (111) direction parallel to the tensile loading direction. The difference in their yield strengths was only 3%, somewhat lower than the corresponding difference noted earlier for FCC copper. As noted earlier, the imposition of the orthorhombic sample symmetry had a larger effect on FCC closures compared to the BCC closures. Nevertheless, the results presented here do indicate that relaxing the assumption of orthorhombic sample symmetry increases the design space and identifies new solutions for optimized performance of materials.

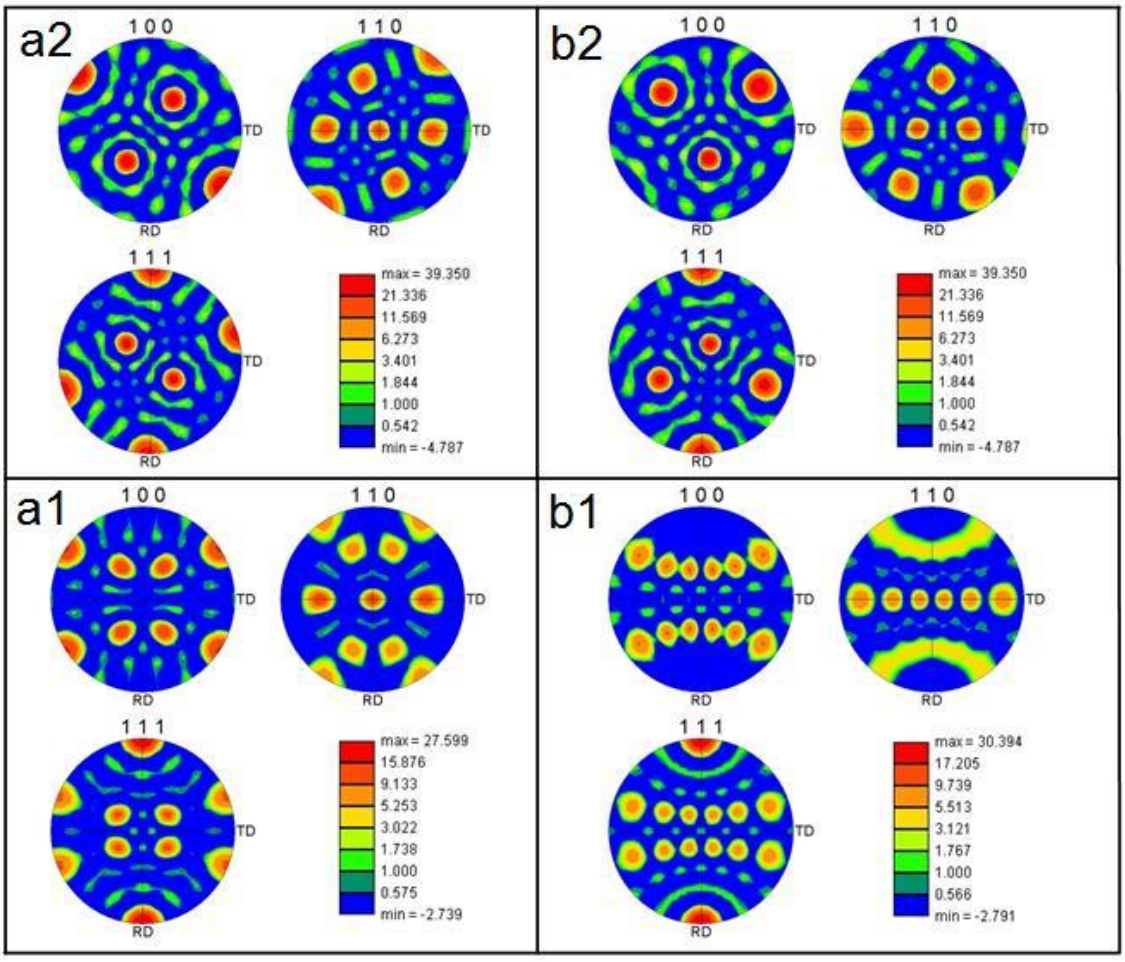

Figure 3.13: Predicted textures at salient points of interest in Figure 3.12 corresponding to the highest values of tensile yield strength, $\boldsymbol{\sigma_{y1}}$.

As another example, we show the first-order cubic-orthorhombic and cubic-triclinic plastic closures for $(\sigma_{y2}, \tau_{y12})$ for both copper and IF steel in Figure 3.14. Once again the imposition of the orthorhombic sample symmetry was seen to produce a bigger effect on the FCC closure compared to the BCC closure. The fact that the difference is consistently larger with a lower number of slip systems (i.e. a higher degree of anisotropy) suggests that the effect will be even larger in the case of other lower symmetry crystal structures such as HCP metals.

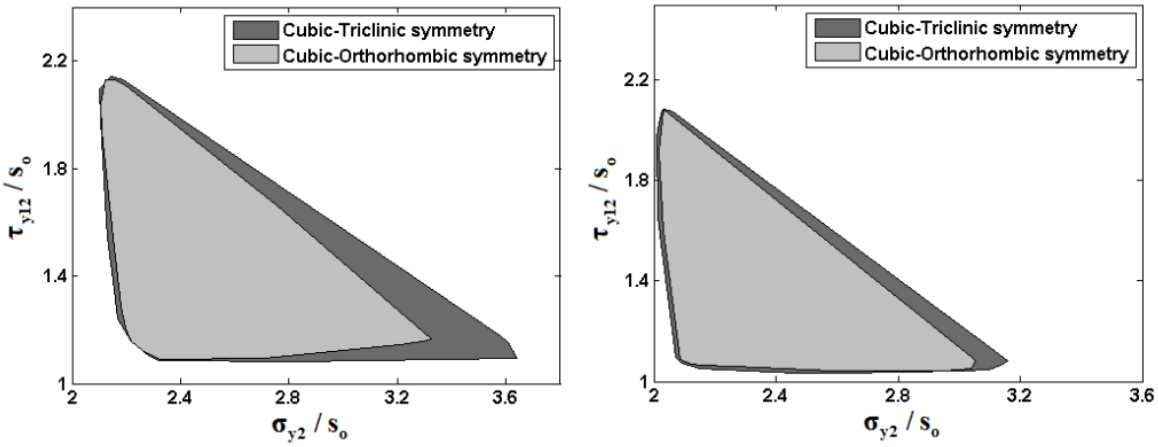

Figure 3.14: $(\sigma_{y2}/s_o, \tau_{y12}/s_o)$ First-order property closures for polycrystalline materials computed using DFT methods based on cubic-triclinic and cubic-orthorhombic symmetries. (a) OFHC Copper, (b) IF-steel.

CHAPTER 4

INTEGRATING THE SPECTRAL CRYSTAL PLASTICITY DATABASES INTO FE SIMULATION TOOLS

The remarkable savings in the computational time involved in solving the crystal plasticity constitutive equations using the new spectral database scheme described in Chapter 3 provide a significant incentive for incorporating it with FE simulation tools. This will allow the user to conduct more efficient CPFEM simulations at dramatically reduced computational cost. This chapter explains how the crystal plasticity DFT databases were integrated with the commercial finite element package ABAQUS through a user materials subroutine (UMAT); this approach will be hereafter referred to as spectral database CPFEM or simply SD-CPFEM. To use the new spectral database scheme in the FE analysis, two tasks must be accomplished. First, the crystal plasticity computations using spectral databases should be extended from rigid-viscoplastic into elastic-viscoplastic deformation. Second, the fourth-rank Jacobian matrix (defined as the derivative of the stress tensor with respect to the increment in strain tensor) needs to be computed efficiently to facilitate integration of the spectral databases with any implicit finite element code. Both of these developments are discussed in more detail next.

4.1 Including Elastic Deformation in the DFT Database Approach

The crystal plasticity calculations using spectral databases need to be extended from rigid-viscoplastic behavior to elastic-viscoplastic deformation. Although the elastic deformation in most metals subjected to finite plastic deformation is indeed very small and can be neglected, it is essential to include elasticity for implementing crystal

plasticity computations with most commercial FE codes. This is mainly because most FE simulation tools, such as ABAQUS (ABAQUS, 2010), provide the total deformation gradient at each integration point as an input to the user-defined material constitutive response (through subroutines such as UMAT in ABAQUS), and expect to be returned the full stress tensor (not just the deviatoric stress tensor). Furthermore, elasticity plays an important role in phenomena such as the springback effect, which is an elasticity driven change in the shape of a part upon unloading.

The following constitutive relations are used to include the elastic deformation with the spectral crystal plasticity approach:

$$\boldsymbol{\tau}^{\boldsymbol{\nabla}*} = \widetilde{\boldsymbol{\mathcal{L}}}\,\mathbf{D}^{*} \tag{4.1}$$

where $\mathbf{D}^{*}$ is the elastic stretching tensor, $\widetilde{\boldsymbol{\mathcal{L}}}$ is the 4$^{\text{th}}$-rank elasticity tensor, and $\boldsymbol{\tau}^{\boldsymbol{\nabla}*}$ is the Jaumann rate of the Kirchoff stress seen by an observer who rotates with the lattice and is defined as

$$\boldsymbol{\tau}^{\boldsymbol{\nabla}*} = \dot{\boldsymbol{\tau}} - \mathbf{W}^{*}\boldsymbol{\tau} + \boldsymbol{\tau}\mathbf{W}^{*} \tag{4.2}$$

The Jaumann rate of the Kirchoff stress can be related to the Jaumann rate of the Cauchy stress $\boldsymbol{\sigma}^{\boldsymbol{\nabla}*}$ as follow:

$$\boldsymbol{\tau}^{\boldsymbol{\nabla}*} = \boldsymbol{\sigma}^{\boldsymbol{\nabla}*} + \mathrm{tr}(\mathbf{D}^{*})\boldsymbol{\sigma} \tag{4.3}$$

where $\boldsymbol{\sigma}^{\boldsymbol{\nabla}*}$ is the Jaumann rate of the Cauchy stress based on the axes that spin together with the lattice and is defined as

$$\boldsymbol{\sigma}^{\nabla *} = \dot{\boldsymbol{\sigma}} - \mathbf{W}^{*}\boldsymbol{\sigma} + \boldsymbol{\sigma}\mathbf{W}^{*} \tag{4.4}$$

In order to use the above relations, the total stretching tensor $\mathbf{D}$ (symmetric part of the velocity gradient tensor) needs to be decomposed into elastic and plastic parts. This decomposition must be accomplished such that the deviatoric stresses computed from both the crystal plasticity DFT databases (see Eq. (2.15), denoted here as $\boldsymbol{\sigma}'^{\mathrm{DFT}}(\mathbf{D}^{p})$) and the above Jaumann rate relations (denoted as $\boldsymbol{\sigma}'^{\mathrm{Jmn}}(\mathbf{D}^{*}, \mathbf{W}^{*}, \Delta \mathrm{t})$) are equal to each other within an acceptable tolerance. It should be noted that the trace of the stretching tensor contributes exclusively to the elastic deformation (assuming that the plastic deformation in metals is isochoric). In other words, only the five independent components of the deviatoric stretching tensor need to be decomposed into elastic and plastic parts. The following modified Newton-Raphson scheme has been developed to accomplish this decomposition:

$$[\mathbf{D}'^{*}]_{n+1} = [\mathbf{D}'^{*}]_{n} - \lambda\ [\mathbf{J}]_{n}^{-1}[\mathbf{Err}]_{n} \tag{4.5}$$

where

$$\mathbf{Err} = \boldsymbol{\sigma}'^{\mathrm{DFT}}(\mathbf{D}^{p}) - \boldsymbol{\sigma}'^{\mathrm{Jmn}}(\mathbf{D}^{*}, \mathbf{W}^{*}, \Delta \mathrm{t}) \tag{4.6}$$

$$\mathbf{J} = \frac{\partial \mathbf{Err}}{\partial \mathbf{D}'^{*}} = -\frac{\partial \boldsymbol{\sigma}'^{\mathrm{DFT}}(\mathbf{D}^{p})}{\partial \mathbf{D}^{p}} - \frac{\partial \boldsymbol{\sigma}'^{\mathrm{Jmn}}(\mathbf{D}^{*}, \mathbf{W}^{*}, \Delta \mathrm{t})}{\partial \mathbf{D}^{*}} \tag{4.7}$$

In Eq. (4.5), the subscripts n and $n+1$ refer to the estimates of $\mathbf{D}'^{*}$ at n and $n+1$ iterations, respectively. The value of the scalar parameter λ in Eq. (4.5) is selected such

that the magnitude of the step correction $\|\Delta\mathbf{D}'^{*}\| = \|[\mathbf{D}'^{*}]_{n+1} - [\mathbf{D}'^{*}]_{n}\| \leq \eta\ \varepsilon_{\text{yield}}$, where ε_{yield} denotes the magnitude of the total strain at yielding and η is a numerical constant taken as 0.1.

It was observed that the initial guess of $\mathbf{D}'^{*}$ strongly affected the number of iterations required to reach convergence in the iterative procedure presented in this work. The following strategy was found to give good results for the initial guess of $\mathbf{D}'^{*}$. First, the values of the deviatoric stress components and the lattice spin tensor are calculated using the spectral crystal plasticity approach assuming rigid-viscoplastic behavior, i.e. $\mathbf{D}'^{\mathrm{p}} = \mathbf{D}'$. These values are then used in (Eqs. (4.1)-(4.4)) to calculate the deviatoric elastic stretching tensor, $\mathbf{D}'^{*}$. If $\|\mathbf{D}'^{*}\| < 0.1\|\mathbf{D}'\|$, use the computed $\mathbf{D}'^{*}$ as the initial guess to start the iterations. Else, the deviatoric stretching tensor, $\mathbf{D}'$, is used as an initial guess for $\mathbf{D}'^{*}$. A flow diagram illustrating the strategy of finding the initial guess of $\mathbf{D}'^{*}$ is given in Figure 4.1. The iterations are carried out until the maximum of the absolute difference in all components of $\mathbf{D}'^{*}$ between two successive iterations is less than $10^{-4}\ \|\mathbf{D}'\|$. Convergence is typically obtained within two iterations; a higher number of iterations are generally required near the elastic-plastic transition zone or during any loading path change.

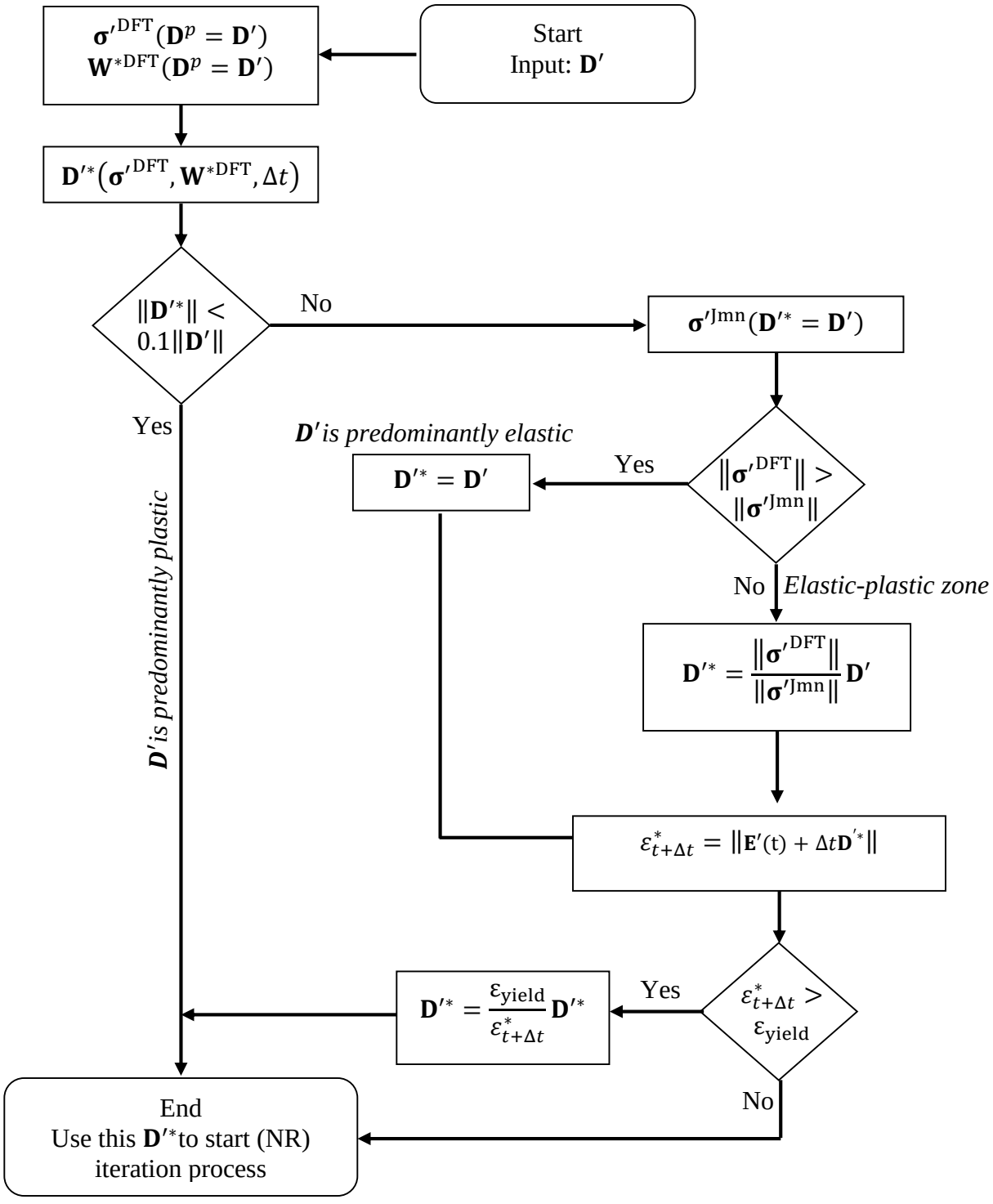

Figure 4.1: Flow diagram that illustrate the strategy followed in this work to find the initial guess of $\mathbf{D}'^{*}$

To verify the stability and accuracy of the above iteration scheme, we have simulated a reverse shearing process using both the spectral database CPFEM approach described in this work and compared the results with those obtained from the classical CPFEM approach (Kalidindi et al., 1992). The FE model is a single cuboid-shaped three-dimensional eight-noded solid element (C3D8) in ABAQUS (ABAQUS, 2010) with the same initial crystal orientation assigned to all eight integration points. The single element is sheared up to a shear strain of γ=0.5 followed by shearing in the opposite direction. The elastic and plastic property parameters in this model are listed in Table 4.1 (these correspond to OFHC copper reported in literature (Kalidindi et al., 1992)). The single crystal is assumed to exhibit the twelve $\{111\}\langle 1\bar{1}0\rangle$ slip systems characteristic of FCC metals (see Table 4.1). Figure 4.2 shows the predicted stress-strain responses from both the spectral database CPFEM (using 500 dominant DFTs for the stress, the shearing rate, and the lattice spin components) and the classical CPFEM for a selected crystal lattice orientation. Several other similar results are obtained for other random crystal orientations. It is clear that the new iteration algorithm described above can accurately capture the elastic response during loading and unloading cycles, and the predictions from both approaches are in excellent agreement with each other.

Table 4.1: Elastic and plastic parameters of the OFHC Copper used in this work (Kalidindi et al., 1992)

C_{11} (MPa)	C_{12} (MPa)	C_{44} (MPa)	m	S_o (MPa)	h_o (MPa)	s_s (MPa)	a
168400	121400	75400	0.01	16	180	148	2.25

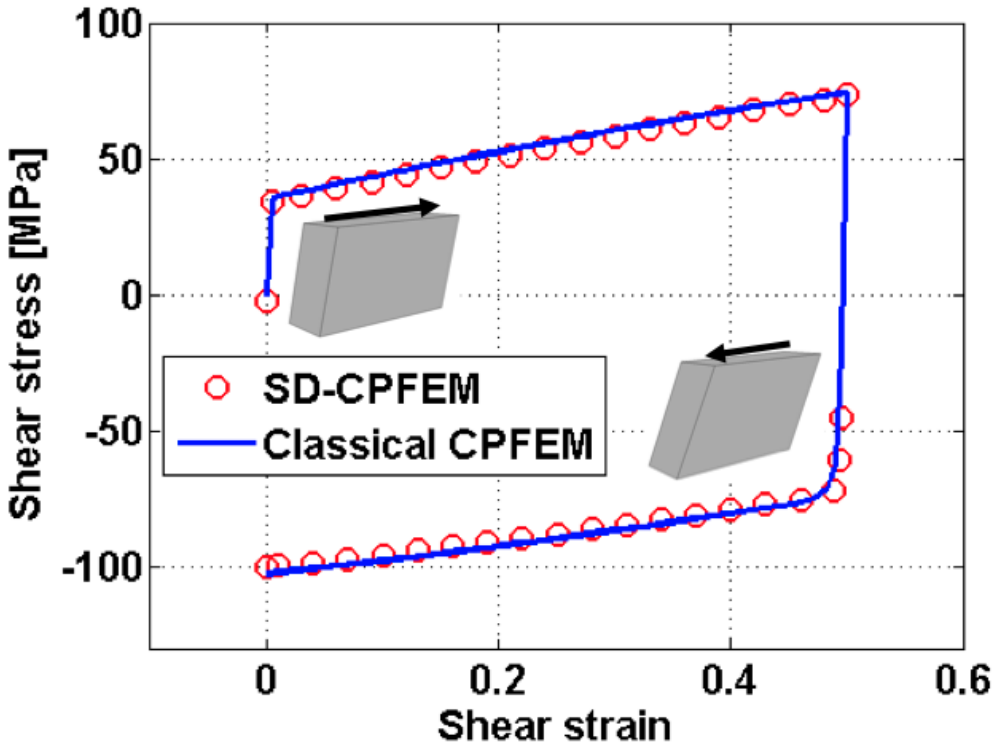

Figure 4.2: Stress-strain curves of reverse shearing process using both the spectral database CPFEM (SD-CPFEM) and the classical CPFEM of copper single element.

4.2 Computation of the Jacobian

The implementation of UMAT in ABAQUS (ABAQUS, 2010) requires the computation of the Jacobian defined as

$$\boldsymbol{\mathcal{J}} = \frac{\partial \Delta \boldsymbol{\sigma}}{\partial \Delta \boldsymbol{\varepsilon}} \equiv \frac{\partial \boldsymbol{\sigma}}{\partial \mathbf{E}_t} \tag{4.8}$$

where $\Delta\boldsymbol{\sigma}$ and $\Delta\boldsymbol{\varepsilon}$ are the increments in the stress and strain tensors in a given time increment, respectively, and $\mathbf{E}_t$ is the relative strain tensor in the same time increment. The Jacobian matrix of Eq. (4.8) is used in the Newton-Raphson iterative method for revising the estimated displacements such that the corresponding stresses are likely to better satisfy the principal of virtual work at the end of the increment. It should be noted that the Jacobian matrix plays an important role in the rate of convergence of the solution to the global equilibrium equations, but has no effect on the accuracy of the solution. For the present work, the following analytical expression for the Jacobian is developed

$$\boldsymbol{\mathcal{J}} = \frac{\partial \boldsymbol{\sigma}}{\partial \mathbf{E}_t} = \frac{\partial \boldsymbol{\sigma}'}{\partial \mathbf{E}_t} + \mathbf{I} \otimes \frac{\partial p}{\partial \mathbf{E}_t} = \frac{\partial \boldsymbol{\sigma}'}{\partial \mathbf{D}'} \frac{\partial \mathbf{D}'}{\partial \mathbf{E}_t} + \mathbf{I} \otimes \frac{\partial p}{\partial \mathbf{E}_t} \tag{4.9}$$

with

$$\frac{\partial \boldsymbol{\sigma}'}{\partial \mathbf{D}'} = \frac{\partial \boldsymbol{\sigma}'}{\partial \mathbf{D}^{\mathrm{p}}} \frac{\partial (\mathbf{D}' - \mathbf{D}'^{*})}{\partial \mathbf{D}'} = \frac{\partial \boldsymbol{\sigma}'}{\partial \mathbf{D}^{\mathrm{p}}} \left(\mathbb{I} - \frac{\partial \mathbf{D}'^{*}}{\partial \boldsymbol{\sigma}'} \frac{\partial \boldsymbol{\sigma}'}{\partial \mathbf{D}'} \right)$$

$$\frac{\partial \boldsymbol{\sigma}'}{\partial \mathbf{D}'} + \frac{\partial \boldsymbol{\sigma}'}{\partial \mathbf{D}^{\mathrm{p}}} \frac{\partial \mathbf{D}'^{*}}{\partial \boldsymbol{\sigma}'} \frac{\partial \boldsymbol{\sigma}'}{\partial \mathbf{D}'} = \frac{\partial \boldsymbol{\sigma}'}{\partial \mathbf{D}^{\mathrm{p}}}$$

$$\frac{\partial \boldsymbol{\sigma}'}{\partial \mathbf{D}'} = \left[\mathbb{I} + \frac{\partial \boldsymbol{\sigma}'}{\partial \mathbf{D}^p}\frac{\partial \mathbf{D}'^*}{\partial \boldsymbol{\sigma}'}\right]^{-\mathbf{1}} \frac{\partial \boldsymbol{\sigma}'}{\partial \mathbf{D}^p} \tag{4.10}$$

where p denotes the pressure, and $\mathbf{I}$ and $\mathbb{I}$ are the second-rank and fourth-rank identity tensors, respectively. The term in Eq. (4.10) that requires long computations is $\frac{\partial \boldsymbol{\sigma}'}{\partial \mathbf{D}^p}$. This term is evaluated analytically using the chain rule as follow:

$$\frac{\partial \boldsymbol{\sigma}'}{\partial \mathbf{D}^p} = \left[\left(\frac{\partial \boldsymbol{\sigma}'}{\partial \dot{\varepsilon}}\bigg|_{\theta,\varphi_1^{\mathrm{D}},\Phi^{\mathrm{D}},\varphi_2^{\mathrm{D}}} \frac{\partial \dot{\varepsilon}}{\partial \mathbf{D}^p}\right) + \left(\frac{\partial \boldsymbol{\sigma}'}{\partial \theta}\bigg|_{\dot{\varepsilon},\varphi_1^{\mathrm{D}},\Phi^{\mathrm{D}},\varphi_2^{\mathrm{D}}} \frac{\partial \theta}{\partial \mathbf{D}^p}\right) + \left(\frac{\partial \boldsymbol{\sigma}'}{\partial \varphi_1^{\mathrm{D}}}\bigg|_{\theta,\dot{\varepsilon},\Phi^{\mathrm{D}},\varphi_2^{\mathrm{D}}} \frac{\partial \varphi_1^{\mathrm{D}}}{\partial \mathbf{D}^p}\right)$$
$$+ \left(\frac{\partial \boldsymbol{\sigma}'}{\partial \Phi^{\mathrm{D}}}\bigg|_{\theta,\dot{\varepsilon},\varphi_1^{\mathrm{D}},\varphi_2^{\mathrm{D}}} \frac{\partial \Phi^{\mathrm{D}}}{\partial \mathbf{D}^p}\right) + \left(\frac{\partial \boldsymbol{\sigma}'}{\partial \varphi_2^{\mathrm{D}}}\bigg|_{\theta,\dot{\varepsilon},\varphi_1^{\mathrm{D}},\Phi^{\mathrm{D}}} \frac{\partial \varphi_2^{\mathrm{D}}}{\partial \mathbf{D}^p}\right)\Bigg] \tag{4.11}$$

where $(\varphi_1^{\mathrm{D}}, \Phi^{\mathrm{D}}, \varphi_2^{\mathrm{D}})$ denotes the set of three Bunge-Euler angles that describe the orientation matrix $[\mathrm{Q}^D]$ used to transform the deviatoric stress tensor from the principle frame of $\mathbf{D}^p$ $\{\boldsymbol{e}_i^p\}$ into the sample frame $\{\boldsymbol{e}_i^s\}$:

$$\boldsymbol{e}_i^s = \sum_{\boldsymbol{j}} \mathrm{Q}_{\mathrm{ij}}^{\mathrm{D}}\, \boldsymbol{e}_j^p \tag{4.12}$$

For simplicity of notation, Eq. (4.11) will be expressed in a condensed form as

$$\frac{\partial \boldsymbol{\sigma}'}{\partial \mathbf{D}^p} = \left[\left(\frac{\partial \boldsymbol{\sigma}'}{\partial \dot{\varepsilon}}\bigg|_{\theta,\mathrm{g}^{\mathrm{D}}} \frac{\partial \dot{\varepsilon}}{\partial \mathbf{D}^p}\right) + \left(\frac{\partial \boldsymbol{\sigma}'}{\partial \theta}\bigg|_{\dot{\varepsilon},\mathrm{g}^{\mathrm{D}}} \frac{\partial \theta}{\partial \mathbf{D}^p}\right) + \left(\frac{\partial \boldsymbol{\sigma}'}{\partial \mathrm{g}^{\mathrm{D}}}\bigg|_{\dot{\varepsilon},\theta} \frac{\partial \mathrm{g}^{\mathrm{D}}}{\partial \mathbf{D}^p}\right)\right] \tag{4.13}$$

where $\mathrm{g}^{\mathrm{D}} = (\varphi_1^{\mathrm{D}}, \Phi^{\mathrm{D}}, \varphi_2^{\mathrm{D}})$.

Analytical expressions for each of the terms in Eq. (4.13) have been derived and validated by comparing the values produced from these expressions with the corresponding values computed numerically by slightly perturbing the independent variable in each expression. It should be noted that, in any time step in the simulation, the term $\frac{\partial \boldsymbol{\sigma}'}{\partial \mathbf{D}^p}$ will be already calculated as a part of the iteration scheme to decompose the stretching tensor into elastic and plastic part (see Eq. (4.7)). Consequently, there is tremendous computational advantage in formulating the Jacobian computation as described in this section. The derivations of the terms in Eq. (4.13) are discussed in more details next.

Recall that the deviatoric stress tensor is calculated using the spectral approach (see Eq.(2.15)) as

$$\boldsymbol{\sigma}'^{(pr)}_{rq}(\theta, \dot{\varepsilon}, \mathrm{g^p}) = s\,\dot{\varepsilon}^m \frac{1}{N_{g^p} N_\theta} \sum_k \sum_n \mathbf{C}_{kn}\, e^{\frac{2\pi i k r}{N_{g^p}}}\, e^{\frac{2\pi i n q}{N_\theta}} \tag{4.14}$$

where the superscript (pr) indicates that the stress values are defined in the principal frame of $\mathbf{D}^p$. This stress tensor can be transformed to the sample frame using the second-rank transformation

$$\boldsymbol{\sigma}'(\mathbf{D}^p, \mathrm{g}) = [\mathrm{Q}^D] \left[\boldsymbol{\sigma}'^{(\mathrm{Pr})}(\theta, \dot{\varepsilon}, \mathrm{g^p})\right] [\mathrm{Q}^D]^{\mathrm{T}} \tag{4.15}$$

where g denotes the crystal lattice orientation defined using the Bunge-Euler angles $(\varphi_1, \phi, \varphi_2)$ (Bunge, 1993b). It should be noted that the Bunge-Euler angles $\mathrm{g}^p, \mathrm{g}, \text{and } \mathrm{g}^D$ are not independent of each other. In fact, one can readily show (see Figure 4.3)

$$[\mathrm{Q}^{p}] = \ [\mathrm{Q}^{D}]^{\mathrm{T}}\,[\mathrm{Q}] \tag{4.16}$$

where $[\mathrm{Q}^{p}]$ is the orientation matrix that brings the crystal frame $\{\boldsymbol{e}_i^c\}$ into coincidence with the principal frame of $\mathbf{D}^{p}, i.e.$ $\{\boldsymbol{e}_i^p\}$, and $[\mathrm{Q}]$ is the rotation matrix that relates the crystal frame $\{\boldsymbol{e}_i^c\}$ to the sample frame $\{\boldsymbol{e}_i^s\}$. These orientation matrices can be calculated using their respective three Bunge-Euler angles. For example, the rotation matrix $[\mathrm{Q}]$ is given by

$$[\mathrm{Q}] \ = \ \begin{bmatrix} \cos\varphi_1\cos\varphi_2 - \sin\varphi_1\sin\varphi_2\cos\Phi & -\cos\varphi_1\sin\varphi_2 - \sin\varphi_1\cos\varphi_2\cos\Phi & \sin\varphi_1\sin\Phi \\ \sin\varphi_1\cos\varphi_2 + \cos\varphi_1\sin\varphi_2\cos\Phi & -\sin\varphi_1\sin\varphi_2 + \cos\varphi_1\ \cos\varphi_2\cos\Phi & -\cos\varphi_1\sin\Phi \\ \sin\varphi_2\ \sin\Phi & \cos\varphi_2\ \sin\Phi & \cos\Phi \end{bmatrix} \tag{4.17}$$

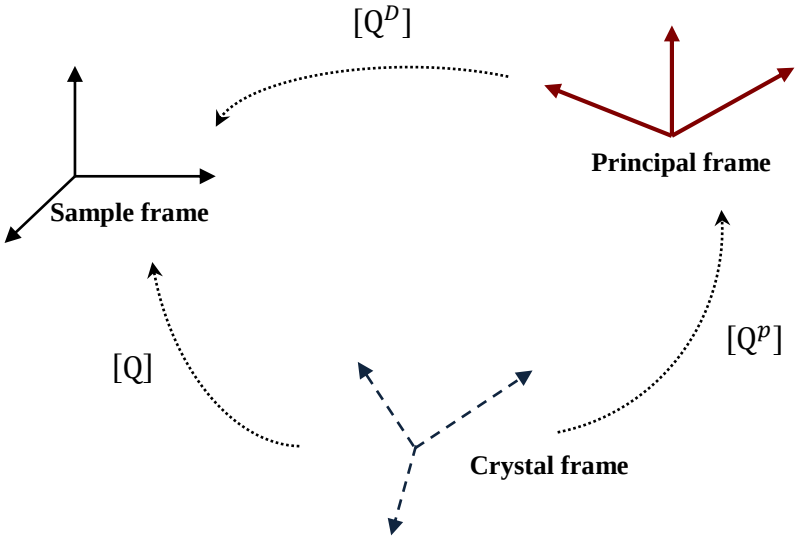

Figure 4.3: A schematic that shows the relations between the sample frame, the principal frame of $\mathbf{D}^{p}$, and the crystal lattice frame.

Using the above relations (Eqs. (4.14)-(4.17)), the analytical expressions for the terms in Eq. (4.13) can be derived as follows (for simplicity, assume that there is no strain hardening, i.e. s is constant in Eq. (4.14)):

1) The term $\left.\frac{\partial \boldsymbol{\sigma}'}{\partial \dot{\varepsilon}}\right|_{\theta,\mathrm{g^D}}$ in Eq. (4.13) is simply evaluated as

$$\left.\frac{\partial \boldsymbol{\sigma}'}{\partial \dot{\varepsilon}}\right|_{\theta,\mathrm{g^D}} = \frac{\mathrm{m}\, s}{\dot{\varepsilon}}\, [\mathrm{Q}^D] \quad \left[\boldsymbol{\sigma}'^{(\mathrm{Pr})}\right] \quad [\mathrm{Q}^D]^{\mathrm{T}} \tag{4.18}$$

2) The term $\left.\frac{\partial \boldsymbol{\sigma}'}{\partial \theta}\right|_{\dot{\varepsilon},\mathrm{g^D}}$ in Eq. (4.13) is calculated as

$$\left.\frac{\partial \boldsymbol{\sigma}'}{\partial \theta}\right|_{\dot{\varepsilon},\mathrm{g^D}} = [\mathrm{Q}^D] \quad \left[\frac{\partial\, \boldsymbol{\sigma}'^{(\mathrm{Pr})}}{\partial \theta}\right] \quad [\mathrm{Q}^D]^{\mathrm{T}} \tag{4.19}$$

where

$$\frac{\partial \boldsymbol{\sigma}'^{(\mathrm{pr})}_{\mathrm{rq}}}{\partial \theta} = \mathrm{s}\ \dot{\varepsilon}^{\mathrm{m}}\ \frac{1}{\mathrm{N_{gp}}\ \mathrm{N_\theta}} \sum_{\mathrm{k}} \sum_{\mathrm{n}} \tilde{\mathbf{C}}_{\mathrm{kn}}\, \mathrm{e}^{\frac{2\pi \mathrm{ikr}}{\mathrm{N_{gp}}}}\ \mathrm{e}^{\frac{2\pi \mathrm{inq}}{\mathrm{N_\theta}}}\ ,$$
$$\tilde{\mathbf{C}}_{kn} = 2\pi \mathrm{in}\, \mathbf{C}_{kn} \tag{4.20}$$

It is clear that the spectral representation presented in this work allows efficient calculation of the term $\frac{\partial \boldsymbol{\sigma}'^{(\mathrm{pr})}_{\mathrm{rq}}}{\partial \theta}$.

3) The term $\frac{\partial \theta}{\partial \mathbf{D}^{\mathrm{p}}}$ in Eq. (4.13) is calculated as

$$\frac{\partial \theta}{\partial \mathbf{D}^p} = \frac{\partial \theta}{\partial \mathrm{D}_1}\frac{\partial \mathrm{D}_1}{\partial \mathbf{D}^p} \tag{4.21}$$

where D_1 is the first eigenvalue of $\mathbf{D}_\mathrm{o}$ defined as (see Eq. (2.13)):

$$\mathbf{D}^\mathrm{p} = \dot{\varepsilon}\,\mathbf{D}_\mathrm{o}, \qquad \mathbf{D}_\mathrm{o} = \sum_{\mathrm{j}=1}^{3} \mathrm{D}_\mathrm{j}\ \mathbf{e}_\mathrm{j}^\mathrm{p} \otimes \mathbf{e}_\mathrm{j}^\mathrm{p}$$

$$\mathrm{D}_1 = \sqrt{\frac{2}{3}}\cos\left(\theta - \frac{\pi}{3}\right), \quad \mathrm{D}_2 = \sqrt{\frac{2}{3}}\cos\left(\theta + \frac{\pi}{3}\right), \quad \mathrm{D}_3 = -\sqrt{\frac{2}{3}}\cos(\theta) \tag{4.22}$$

The term $\frac{\partial \theta}{\partial \mathrm{D}_1}$ in Eq. (4.21) can be calculated directly from the above expression of D_1. However, the term $\frac{\partial \mathrm{D}_1}{\partial \mathbf{D}^p}$ is derived analytically using the determinant of $\mathbf{D}_\mathrm{o}$ defined as

$$\det(\mathbf{D}_\mathrm{o}) = \det\left(\frac{1}{\dot{\varepsilon}}\mathbf{D}^p\right) = \mathrm{D}_1\mathrm{D}_2\mathrm{D}_3 = \mathrm{D}_1^3 - \frac{1}{2}\mathrm{D}_1 \tag{4.23}$$

4) The computation of the term $\left.\frac{\partial \boldsymbol{\sigma}'}{\partial \mathrm{g}^\mathrm{D}}\right|_{\dot{\varepsilon},\theta}$ in Eq. (4.13) involves the calculations of the derivatives $\frac{\partial [\mathrm{Q}^\mathrm{D}]}{\partial \mathrm{g}^\mathrm{D}}$ and $\frac{\partial\, \sigma'^{(\mathrm{Pr})}}{\partial \mathrm{g}^\mathrm{D}}$ (see Eq. (4.15)):

$$\left.\frac{\partial \boldsymbol{\sigma}'}{\partial \mathrm{g}^\mathrm{D}}\right|_{\dot{\varepsilon},\theta} = f\left(\frac{\partial [\mathrm{Q}^D]}{\partial \mathrm{g}^\mathrm{D}},\ \frac{\partial\, \sigma'^{(\mathrm{Pr})}}{\partial \mathrm{g}^\mathrm{D}}\right) \tag{4.24}$$

where

$$\frac{\partial\, \sigma'^{(\mathrm{Pr})}}{\partial \mathrm{g}^\mathrm{D}} = \frac{\partial\, \sigma'^{(\mathrm{Pr})}}{\partial \mathrm{g}^\mathrm{p}}\frac{\partial \mathrm{g}^\mathrm{p}}{\partial \mathrm{g}^\mathrm{D}} \tag{4.25}$$

The term $\frac{\partial\, \sigma'^{(\mathrm{Pr})}}{\partial \mathrm{g^p}}$ is calculated using an expression similar to Eq. (4.20) given as

$$\frac{\partial \boldsymbol{\sigma}'^{(pr)}_{rq}}{\partial \mathrm{g^p}} = s\ \dot{\varepsilon}^m\ \frac{1}{N_{\mathrm{g}^p}\, N_\theta} \sum_k \sum_n \tilde{\mathbf{C}}_{kn}\, e^{\frac{2\pi i k r}{N_{\mathrm{g}^p}}}\ e^{\frac{2\pi i n q}{N_\theta}}\ , \qquad \tilde{\mathbf{C}}_{kn} = 2\pi \mathrm{i} k\, \mathbf{C}_{kn} \tag{4.26}$$

Furthermore, the terms $\frac{\partial \mathrm{g^p}}{\partial \mathrm{g^D}}$ and $\frac{\partial [\mathrm{Q}^D]}{\partial \mathrm{g^D}}$ are derived using Eq. (4.16) and the following relations obtained from Eq. (4.17):

$$\begin{aligned} \cos(\Phi^{\mathrm{p}}) &= [\mathrm{Q}^p]_{33} \\ \cos\left(\varphi_1^{\mathrm{p}}\right) &= \frac{[\mathrm{Q}^p]_{13}}{-[\mathrm{Q}^p]_{23}} \\ \cos\left(\varphi_2^{\mathrm{p}}\right) &= \frac{[\mathrm{Q}^p]_{31}}{-[\mathrm{Q}^p]_{32}} \end{aligned} \tag{4.27}$$

where the subscripts ij in $[\mathrm{Q}^p]_{ij}$ indicate the ijth component of the orientation matrix $[\mathrm{Q}^p]$.

5) The term $\frac{\partial \mathrm{g^D}}{\partial \mathbf{D}^{\mathrm{p}}}$ in Eq. (4.13) is calculated using the relation

$$\mathbf{D}^p\ \mathrm{N}^{(i)} = \lambda\ \mathrm{N}^{(i)} \tag{4.28}$$

where $\mathrm{N}^{(i)}$ denotes the ith column of $[\mathrm{Q}^D]$**,** which represents the eigenvector of $\mathbf{D}^p$ corresponding to the eigenvalue λ. To avoid the additional calculations of evaluating the derivative of the eigenvalues with respect to $\mathbf{D}^{\boldsymbol{p}}$, we use the orthogonality property of the eigenvectors and rewrite Eq. (4.28) as

$$\mathbf{D}^p \, \mathrm{N}^{(i)} \cdot \mathrm{N}^{(j)} = \lambda \, \mathrm{N}^{(i)} \cdot \mathrm{N}^{(j)} = 0 \qquad \text{for } i \neq j \tag{4.29}$$

More specifically, the following system of linear equations is used to find analytical expressions for the term $\frac{\partial \mathrm{g}^{\mathrm{D}}}{\partial \mathbf{D}^p}$ along with using Eq. (4.17):

$$\begin{aligned} \mathbf{D}^p \, \mathrm{N}^{(1)} \cdot \mathrm{N}^{(2)} &= 0 \\ \mathbf{D}^p \, \mathrm{N}^{(1)} \cdot \mathrm{N}^{(3)} &= 0 \\ \mathbf{D}^p \, \mathrm{N}^{(2)} \cdot \mathrm{N}^{(3)} &= 0 \end{aligned} \tag{4.30}$$

For completeness, the analytical expression for the term $\frac{\partial \mathbf{D}}{\partial \mathbf{E}_t}$ in Eq. (4.9) is derived using the following relations

$$\dot{\mathbf{F}} = \mathbf{L} \, \mathbf{F} \tag{4.31}$$

$$\mathbf{F}(\mathrm{t} + \Delta \mathrm{t}) = \exp(\Delta \mathrm{t} \; \mathbf{L}) \; \mathbf{F}(\mathrm{t}) \tag{4.32}$$

$$\mathbf{F}_{\mathrm{t}} = \mathbf{F}(\mathrm{t} + \Delta \mathrm{t}) \, \mathbf{F}(\mathrm{t})^{-\mathbf{1}} = \exp(\Delta \mathrm{t} \; \mathbf{L}) \simeq \mathbf{I} + \Delta \mathrm{t} \; \mathbf{L} \tag{4.33}$$

where $\mathbf{F}_{\mathrm{t}}$ is the relative deformation gradient tensor. Since the total stretching tensor is the symmetric part of the velocity gradient tensor, then

$$\mathbf{D} = \frac{1}{2}\left(\mathbf{L} + \mathbf{L}^{\mathrm{T}}\right) \simeq \frac{1}{2\Delta \mathrm{t}}\left[(\mathbf{F}_{\mathrm{t}} - \mathbf{I}) + (\mathbf{F}_{\mathrm{t}} - \mathbf{I})^T\right] \tag{4.34}$$

$$\mathbf{D} \simeq \frac{1}{2\Delta \mathrm{t}}\left[(\mathbf{R}_{\mathrm{t}}\mathbf{U}_{\mathrm{t}} - \mathbf{I}) + (\mathbf{R}_{\mathrm{t}}\mathbf{U}_{\mathrm{t}} - \mathbf{I})^T\right] \tag{4.35}$$

where $\mathbf{R}_t$ and $\mathbf{U}_t$ are the relative rotation and stretch tensors, respectively. Now, assume that the relative strain tensor is defined as:

$$\mathbf{E}_t = \ln(\mathbf{U}_t) \simeq (\mathbf{U}_t - \mathbf{I}) - \frac{1}{2}(\mathbf{U}_t - \mathbf{I})^2 + \cdots \tag{4.36}$$

By ignoring the higher order terms, we can rewrite Eq. (4.35) as

$$\mathbf{D} \simeq \frac{1}{2\Delta t}(\mathbf{R}_t\mathbf{E}_t + \mathbf{R}_t + \mathbf{E}_t\,\mathbf{R}_t^T + \mathbf{R}_t^T) - \frac{1}{\Delta t}\mathbf{I} \tag{4.37}$$

which is used to derive the analytical expression for the term $\frac{\partial \mathbf{D}}{\partial \mathbf{E}_t}$.

4.3 Case Studies

The formulations described above for including the elastic deformation with the spectral database approach and computing the analytical expressions of the Jacobian were coded in a customized user material subroutine UMAT to perform crystal plasticity computations in ABAQUS. A flow diagram that describes the sequence of calculations in this UMAT is shown in Figure 4.4. The main subroutines of this UMAT are also shown in Appendix B. In order to demonstrate the viability and computational advantages of the new spectral database CPFEM developed in this work, we compare the stress-strain responses and the evolution of crystallographic texture in polycrystalline aggregates of OFHC copper and interstitial-free **(**IF) steel predicted from the new spectral approach with the corresponding results from the classical CPFEM for selected deformation processes, including non-monotonic loading histories. The predictions from the two approaches reported here are produced using the commercial FE package ABAQUS (ABAQUS, 2010) and specially developed user material subroutines (described in this work and those in Ref. (Kalidindi et al., 1992)).

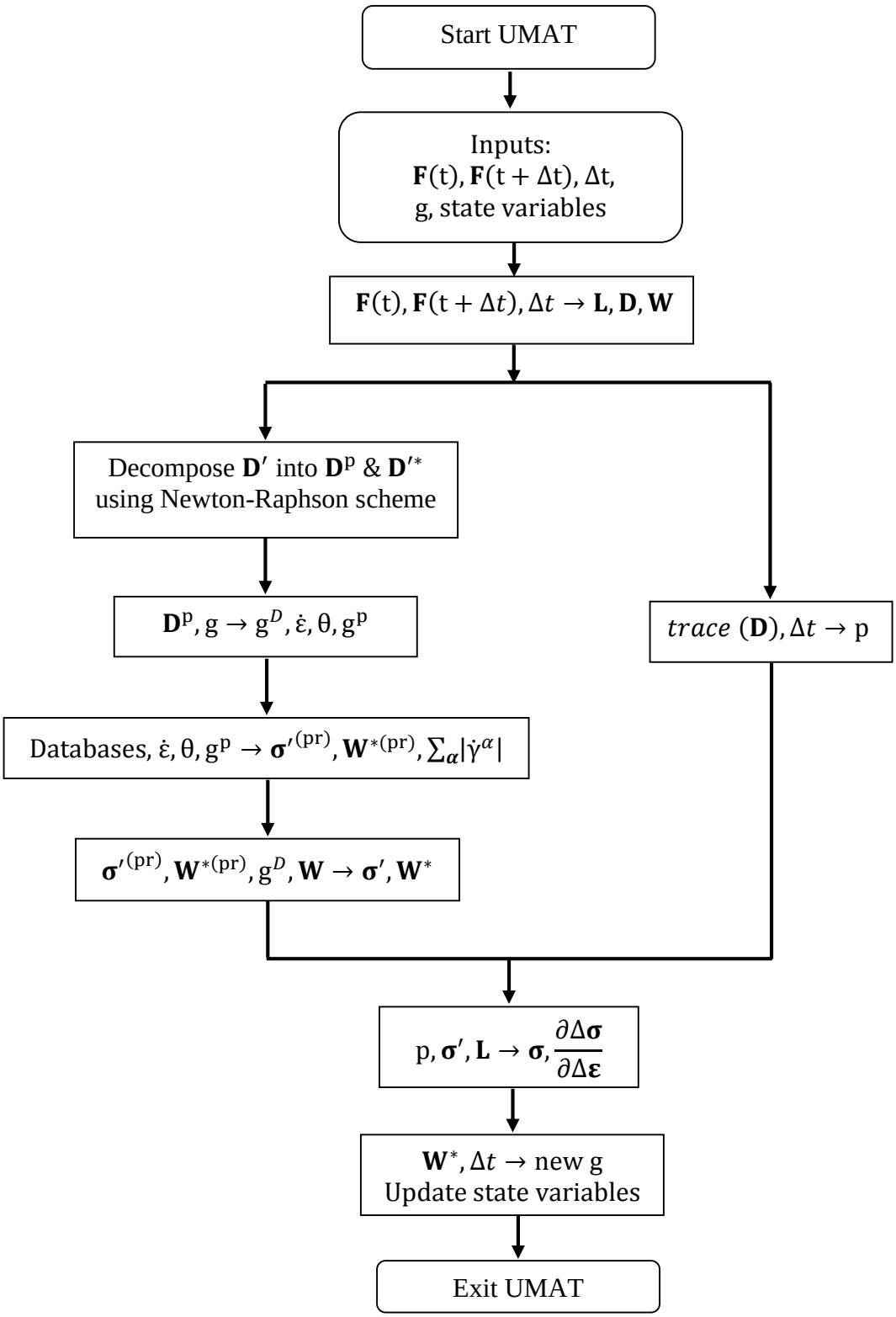

Figure 4.4: Flow diagram for user material subroutine UMAT to perform crystal plasticity computations in the FE package ABAQUS using spectral databases.

4.3.1 Plane Strain Compression of Copper

We first simulated plane strain compression of a polycrystalline aggregate of OFHC copper. For FCC metals, the family of twelve $\{111\}\langle 1\bar{1}0\rangle$ slip systems are assumed to be the potential slip systems for plastic deformation (see Table 3.3). The three-dimensional FE model consisted of 500 C3D8 elements. In this model, the top surface was subjected to a displacement boundary condition, which resulted in a 65% reduction in height corresponding to an axial true strain of about 1.0. The displacements of nodes on the two lateral faces are constrained such that these nodes remain on their respective planes as shown in Figure 4.5. The initial texture was assumed to be random consisting of 4000 different crystal orientations. It should be noted that the random texture is selected because it produces the most heterogeneous microscale stress and strain fields in the sample, and therefore offers an excellent opportunity to validate the SD-CPFEM approach. Each integration point inside each element was assigned a single crystal orientation chosen randomly from the set of 4000 crystal orientations. The elastic and plastic parameters of the OFHC copper used in this case study are shown in Table 4.1.

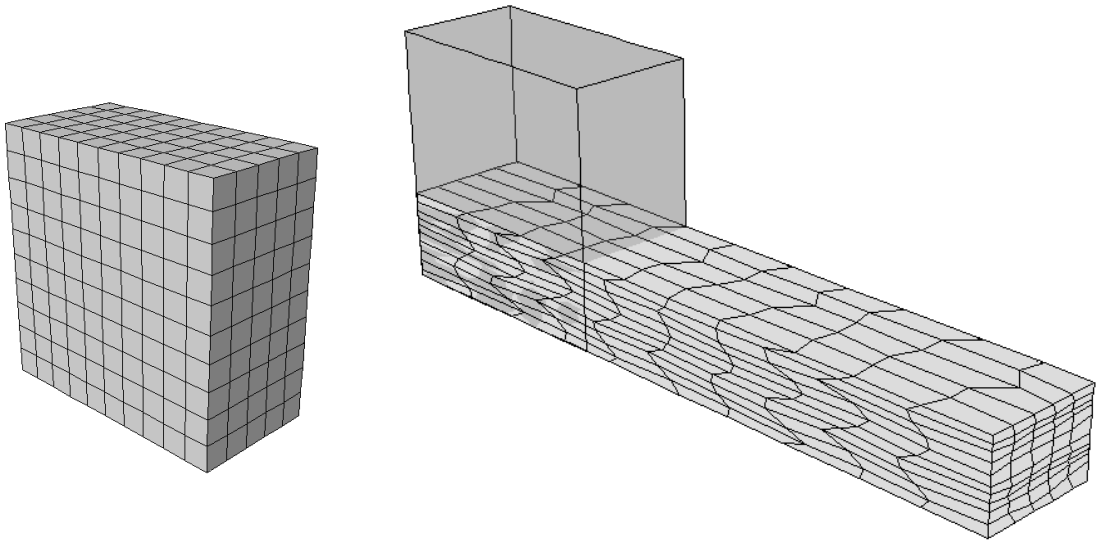

Figure 4.5: FE model of the plane strain compression case study showing the initial mesh (left) and deformed mesh with superimposed initial geometry (right).

We compared in Figure 4.6 the stress-strain responses and deformed texture produced from the SD-CPFEM (for clarity, only few points are shown in the plot), based on 500 dominant DFTs for the stress, the shearing rate, and the lattice spin components, against the corresponding predictions from the conventional CPFEM (Kalidindi et al., 1992). It is clear that the SD-CPFEM produced excellent predictions but at a significantly faster computational speed. In this case study, the simulation took 8964 seconds (~2.5 hr) using the classical CPFEM, and only 602 seconds (~10 min) for the SD-CPFEM based on 500 dominant DFTs. It is underlined that the simulation speed of the SD-CPFEM can be controlled through the selection of the appropriate number of DFTs. The user can select a small number of DFTs to increase the computational speed of the simulation but at the expense of accuracy. For example, in this case study the same simulation required only 231 seconds (~ 4 min) when using 150 DFTs. The predictions from the SD-CPFEM

based on 150 dominants DFTs are also compared against those obtained from the classical CPFEM in Figure 4.7. It is clear that the predictions from the SD-CPFEM using a small number of dominant DFTs are still in reasonable agreement with the predictions from the conventional CPFEM.

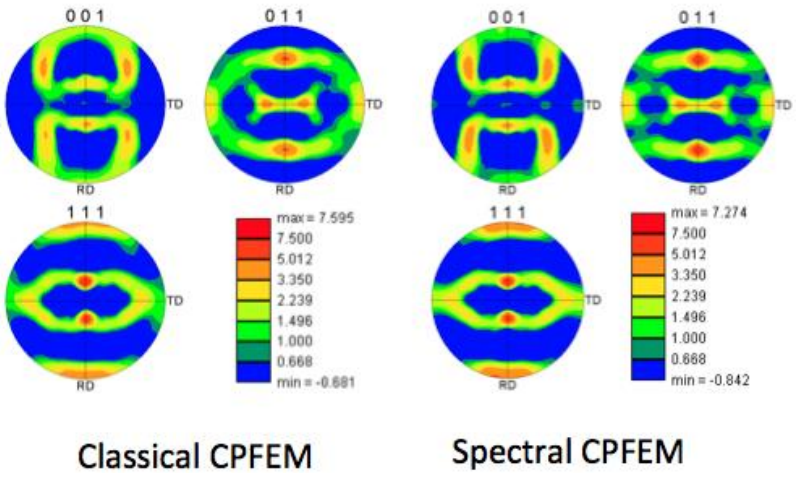

(a)

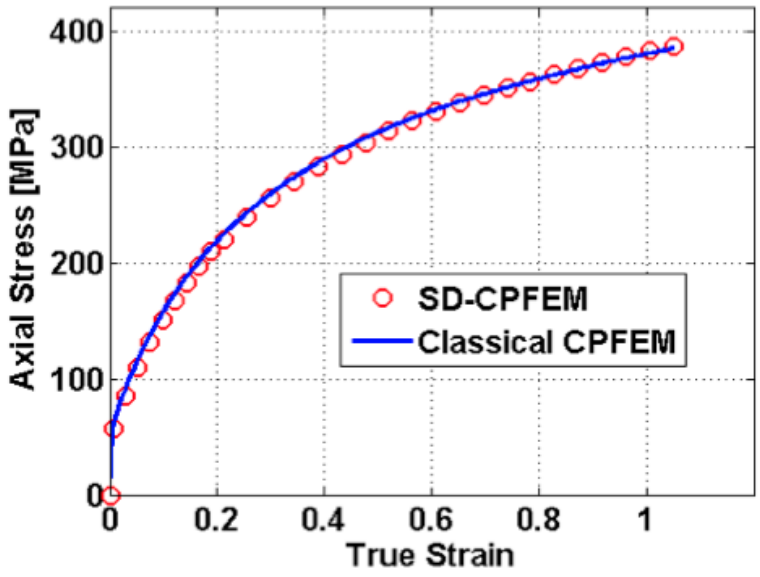

(b)

Figure 4.6: Comparison of the predictions from the SD-CPFEM based on 500 dominant DFTs against the corresponding predictions from the conventional CPFEM for plane strain compression of OFHC copper: (a) pole figures, and (b) stress-strain curves.

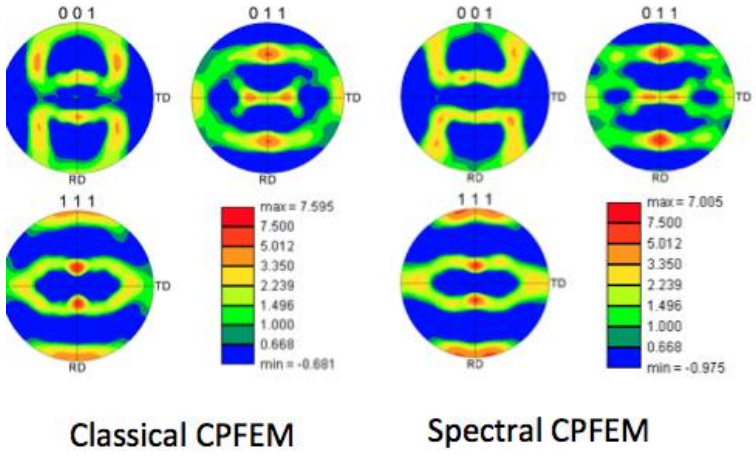

(a)

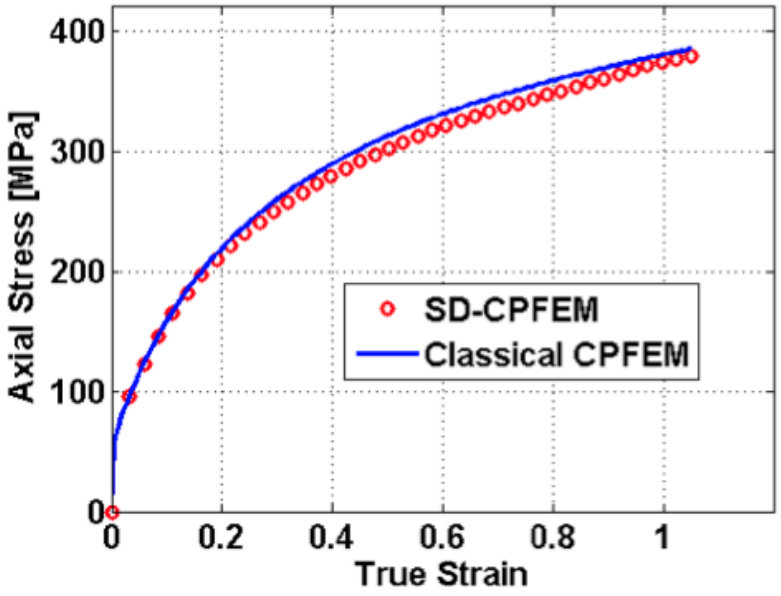

(b)

Figure 4.7: Comparison of the predictions from the SD-CPFEM based on 150 dominant DFTs, against the corresponding predictions from the conventional CPFEM for plane strain compression of OFHC copper: (a) pole figures, and (b) stress-strain curves.

To better quantify the computational efficiency of the SD-CPFEM, we repeated the simulations described above for different number of elements including 500, 4000, and 10976 C3D8 elements. We again assigned a single crystal orientation chosen randomly from a set of large crystal orientations to each integration point inside each element. The sample is subjected to plane strain compression up to an axial strain of 1.0 (~65% reduction in height). Table 4.2 compares the simulation time between the classical CPFEM and the SD-CPFEM based on 500 DFTs and 150 DFTs for different number of elements. It is seen that the SD-CPFEM can speed up the computation time by about 40 times compared to the classical CPFEM when using a small set of dominant DFTs.

Table 4.2: Comparison of the simulation time between the classical CPFEM and the spectral database CPFEM (SD-CPFEM) based on 500 and 150 dominant DFTs for different number of elements for plane strain compression of OFHC copper up to an axial strain of 1.0 (~65% reduction in height). Each integration point inside each element was assigned a single crystal orientation chosen randomly from a set of large crystal orientations.

	500 C3D8 elements	4000 C3D8 elements	10976 C3D8 elements
Classical CPFEM	8964 sec (~2.5 hr)	98507 sec (~27.4 hr)	325161 (~ 3.8 days)
SD-CPFEM (500 DFTs)	602 sec (~10 min)	5781 sec (~1.6 hr)	21725 sec (~6 hr)
SD-CPFEM (150 DFTs)	231 sec (~4 min)	2752 sec (~46 min)	8769 sec (~2.4 hr)

4.3.2 Simple Shear of IF Steel

In the next case study, we compared the stress-strain curves and texture evolution produced from the SD-CPFEM against the corresponding results from the conventional CPFEM for a simple shear deformation of a polycrystalline interstitial free (IF) steel. For BCC metals, the families of 48 potential slip systems are assumed to include $\{110\}\langle\bar{1}11\rangle, \{\bar{1}12\}\langle1\bar{1}1\rangle,$ and $\{12\bar{3}\}\langle111\rangle$(see Table 3.1). For the SD-CPFEM simulations discussed in this case study, the spectral database developed for BCC metals in Section 3.1 were used. It was shown before that because of the availability of a higher number of slip systems in BCC metals (48 slip system in BCC compared to 12 in FCC metals), the spectral database for BCC metals was more compact compared to the one obtained for FCC metals. In other words, a smaller number of dominant DFTs can be used for BCC metals to achieve the desired accuracy.

The FE model is discretized into 500 three-dimensional solid elements (C3D8). A simple shear deformation is applied up to a shear strain $\gamma = 1.0$ as shown in Figure 4.8. To produce the most heterogeneous stress and strain fields in the model and therefore allow better opportunity to validate the spectral approach described in this work, each integration point is assigned a single crystal orientation chosen randomly from a set of 4000 crystal orientations that produce a random texture. The values of the elastic and plastic parameters of the IF steel used in this case study are shown in Table 4.3 (Al-Harbi et al., 2010). Figure 4.9 shows a comparison of the stress-strain responses and final texture predicted by both the spectral and conventional CPFEM codes. As can be clearly seen in this figure, the two predictions are in excellent agreement with each other. It should be noted that the predictions from the SD-CPFEM are obtained with significantly

less computational cost compared to the classical CPFEM. For this case study, the classical CPFEM required 4380 seconds, whereas the SD-CPFEM took only 336 seconds when using 500 DFTs for the stress, the shearing rate, and the lattice spin components.

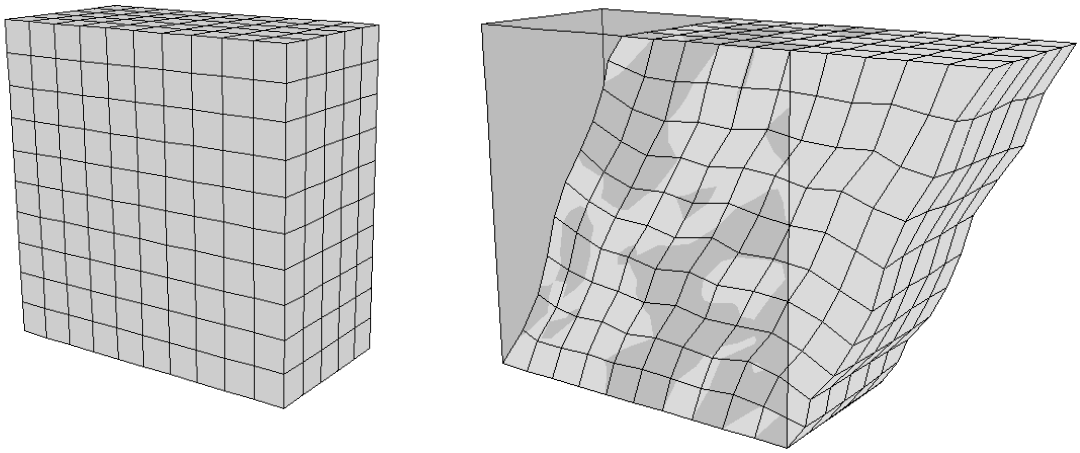

Figure 4.8: FE model of the simple shear case study showing the initial mesh (left) and deformed mesh with superimposed initial geometry (right).

Table 4.3: Elastic and plastic parameters of the interstitial-free **(**IF) steel (Al-Harbi et al., 2010).

C_{11} (MPa)	C_{12} (MPa)	C_{44} (MPa)	m	S_o (MPa)	h_o (MPa)	s_s (MPa)	a
228000	132000	116500	0.01	50	500	230	2.8

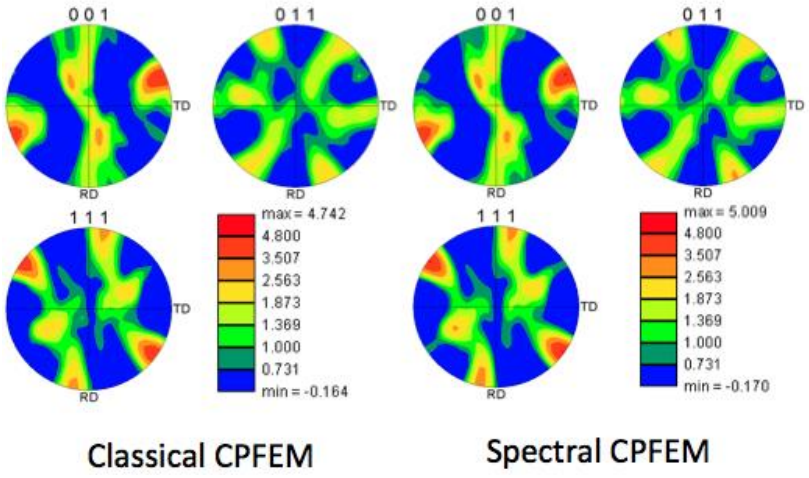

(a)

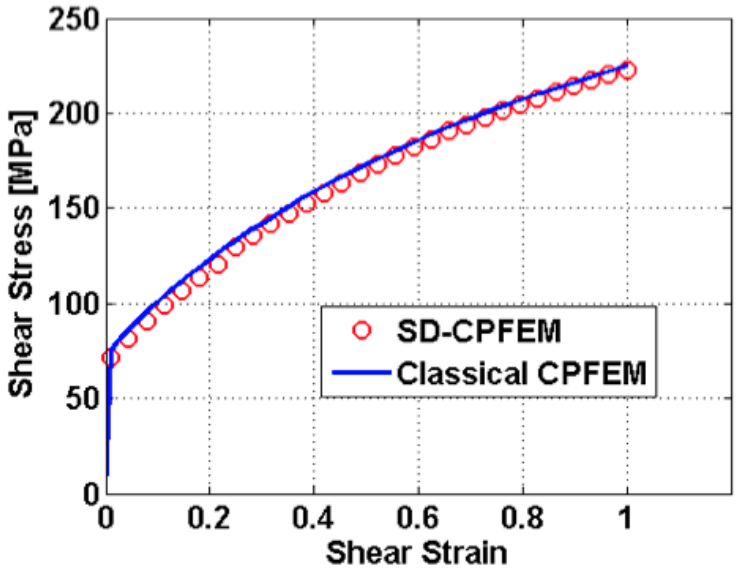

(b)

Figure 4.9: Comparison of the predictions from the SD-CPFEM against the corresponding predictions from the conventional CPFEM for simple shear of interstitial-free (IF) steel: (a) pole figures, and (b) stress-strain curves.

4.3.3 Plane Strain Compression Followed by Simple Shear

To validate the spectral database CPFEM for the case of non- monotonic loading, we simulated a plane strain compression followed by simple shear of a polycrystalline OFHC copper. The FE model consisted of 500 C3D8 elements with one crystal orientation per integration point. The initial texture is assumed to be random. The first step in this simulation involved an imposed displacement boundary condition on the top surface of the model, which resulted in a 35% reduction in height corresponding to an axial true strain of about 0.4. All faces of the sample are constrained to remain planar in this step. In the second step, an imposed simple shear deformation is applied up to a shear strain of $\gamma = 0.5$ as shown in Figure 4.10 (a) and (b). The elastic and plastic parameters of the OFHC copper used in this case study are similar to the one shown in Table 4.1. The effective stress-strain response from the SD-CPFEM is compared against the corresponding predictions from the classical CPFEM in Figure 4.10 (c). The predicted textures from the two approaches after each deformation step are shown in Figure 4.11. It was seen once again that the predictions from the spectral database approach matched very well with the corresponding predictions from the conventional CPFEM at a dramatically reduced computation cost. This prediction took 6380 seconds for the classical CPFEM and only 527 seconds for the SD-CPFEM when using 500 DFTs for the stress, the shearing rate, and the lattice spin components.

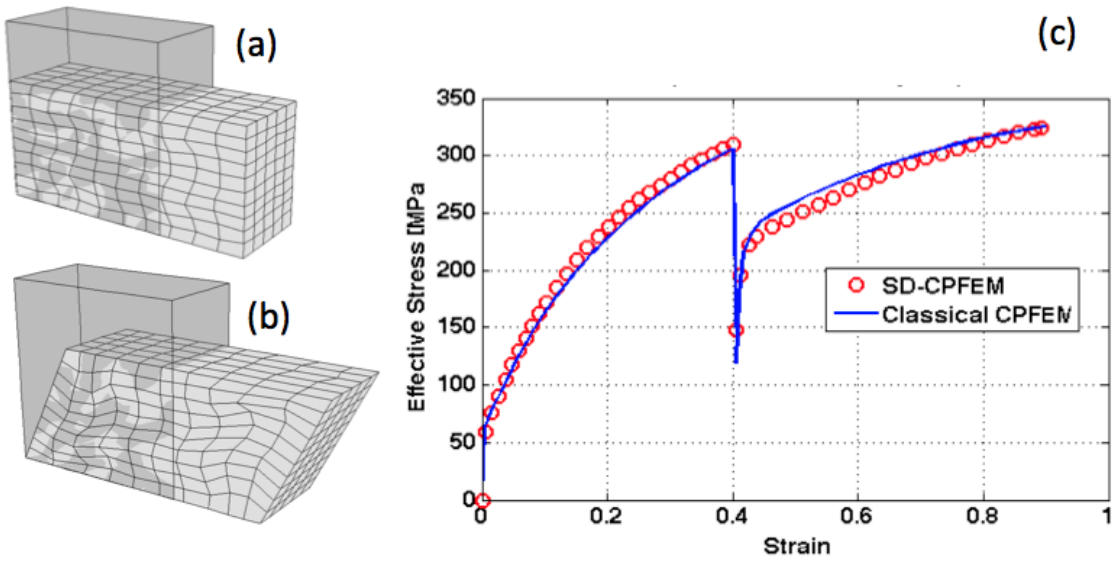

Figure 4.10: Comparison of the predicted effective stress-strain curves from the SD-CPFEM against the corresponding results from the conventional CPFEM for plane strain compression followed by simple shear deformation of OFHC copper: (a) mesh after plane strain compression, (b) mesh after simple shear deformation, (c) effective stress-strain curves.

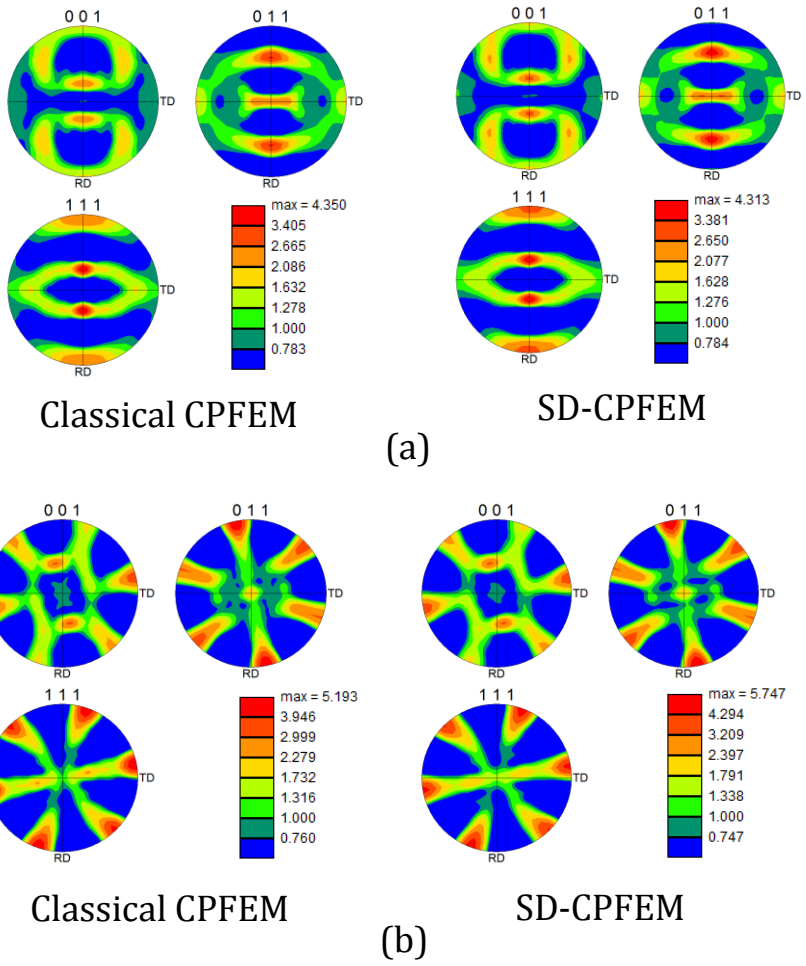

Figure 4.11: Comparison of the predicted texture from the SD-CPFEM against the corresponding predictions from the conventional CPFEM for plane strain compression followed by simple shear deformation of OFHC copper: (a) pole figures after plane strain compression, (b) pole figures after simple shear deformation.

CHAPTER 5

APPLICATION OF CPFEM FOR ESTIMATING THE CRITICAL RESOLVED SHEAR STRESS IN DUAL PHASE STEELS USING SPHERICAL NANOINDENTATION

This chapter presents an important application of the CPFEM for the extraction of crystal level plasticity parameters in multiphase materials. More specifically, we describe a new methodology for extracting the critical resolved shear stress of the ferrite phase in dual phase steels by combining spherical nanoindentation, OIM, and CPFEM. It should be noted that the lack of knowledge of crystal-scale plasticity parameters (e.g. slip hardening parameters) for many important multiphase polycrystalline materials is a major challenge in applying crystal plasticity theories for simulating the deformation behavior of these materials. This mainly arises from the difficulty of measuring the local mechanical response in each individual phase in these materials. After a short literature review, the experimental and computational procedures for this new approach are explained.

5.1 Introduction

Dual phase steels are widely used in automotive applications due to their combination of high strength and good formability. The microstructure of dual phase steel consists mainly of soft ferrite matrix and about 10-30 vol. % of hard martensite particles (Grushko and Weiss, 1989; Korzekwa et al., 1980; Nagorka et al., 1987; Paruz and Edmonds, 1989; Sakaki et al., 1983; Watt and Jain, 1984). There have been

numerous attempts in literature to characterize the local mechanical response of the constituent ferrite and martensite phases in dual phase steels (Calcagnotto et al., 2010; Choi et al., 2013; Kadkhodapour et al., 2011a; Kadkhodapour et al., 2011b; Korzekwa et al., 1984; Sarosiek and Owen, 1984; Woo et al., 2012; Yoshida et al., 2011). The quantification of the local plasticity parameters (e.g. slip hardening parameters) in each individual phase is necessary for the application of physics-based models such as crystal plasticity theories for simulating the deformation behavior of these materials. For single-phase polycrystalline materials, the slip hardening parameters are commonly extracted by calibrating the predicted overall stress-strain responses in multiple loading conditions against the corresponding measurements. However, this approach is unlikely to work as well for multiphase materials such as dual phase steels, where the constituents typically exhibit a higher contrast in their response.

Different strategies have been used to estimate the slip hardening parameters in dual phase steels. Yoshida et al. (Yoshida et al., 2011) estimated the crystal plasticity hardening parameters of the ferrite and martensite phases by fitting the stress-strain curve of a polycrystalline aggregate comprised of both ferrite and martensite grains to the measured macroscopic stress-strain response of dual phase steel. It should be noted that several different sets of slip hardening parameters for the ferrite and martensite phases can produce the same overall stress-strain response. Instead of calibrating the predictions from the crystal plasticity model to the overall measured response, Kadkhodapour et al. (Kadkhodapour et al., 2011a) estimated the hardening parameters of the ferrite phase by fitting the predicted stress-strain curve of the ferrite phase to the corresponding calculated one of the ferrite phase from an empirical model based on the chemical composition of

the material. In another recent strategy, Woo et al. (Choi et al., 2013; Woo et al., 2012) determined the crystal plasticity hardening parameters of the ferrite and martensite phases in the commercial dual phase steels DP980 by calibrating the predictions from CPFEM based on representative volume elements (RVE) to the measured macroscopic stress and measured lattice strains during uniaxial tension. The lattice strains were measured using neutron diffraction experiment. It should be noted that the measured lattice strains represent the behavior of all grains (including ferrite and martensite) within the beam resolution that satisfy Bragg's law for the prescribed diffraction angle and lattice plane of interest. The overlapped diffraction peaks of the ferrite and martensite were separated using Gaussian functions. Table 5.1 summarizes the values of the critical resolved shear stress for the ferrite and martensite phases in dual phase steels from the above methods. It is clear that the difficulty of measuring the local mechanical response in each individual phase has contributed to the large variance in the reported values of the critical resolved shear stress for the ferrite and martensite phases in dual phase steels.

There is a need to develop efficient experimental and numerical tools for studying microscale grain and phase interactions and extracting crystal-level slip hardening parameters for multiphase materials such as dual phase steels. Nanoindentation has shown to be an efficient tool for characterizing the local mechanical behavior in different material systems. Most of the previous traditional work in this field has focused on characterizing the local hardness using sharp indenters. However, Pathak et al. (Kalidindi and Pathak, 2008; Pathak et al., 2008; Pathak et al., 2009b) has recently developed a new data analysis method for spherical nanoindentation that converts the measured indentation load-displacement data into indentation stress-strain curves. These stress-

strain curves have produced more reliable estimates of the local elastic and plastic properties (such as indentation modulus and indentation yield strength) in the sample. In order to use this technique for extracting grain-scale slip hardening parameters, it is necessary to simulate nanoindentation using CPFEM. This chapter presents preliminary results from the application of this new data analysis approach for extracting the critical resolved shear stress of the ferrite phase in dual phase steels using a combined application of spherical nanoindentation, OIM, and CPFEM. This new methodology offers a novel efficient tool for the extraction of crystal level hardening parameters in any single or multiphase materials.

Table 5.1. Some values of the critical resolved shear stress (τ_{crss}) reported in the literature for the ferrite and martensite phases in dual phase steels.

Yield strength* (MPa)	Ferrite τ_{crss} (MPa)	Martensite τ_{crss} (MPa)	Approach	Reference
~ 380	135	950	Calibration to the measured macroscopic stress-strain response of the dual phase steel.	(Yoshida et al., 2011)
~ 550	198, 228	NA	Calibration to the predicted stress-strain response of the ferrite phase obtained from an empirical model.	(Kadkhodapour et al., 2011a)
~ 700	170	435	Calibration to the measured macroscopic stress and measured lattice strains.	(Choi et al., 2013; Woo et al., 2012)

* The values of the yield strength is roughly estimated here from the given macroscopic stress-strain curves.

5.2 Materials and Method

The dual phase steel samples used in this study were produced from low carbon steels (SAE 1018) using intercritical annealing. A low carbon steel rod measuring 12.5 mm diameter x 100 mm height was first put in a vacuumed glass tube and austenitized at 1100^{o}C for 8 hours and then furnace cooled to room temperature. Cylindrical compression samples were machined from the rod with dimensions of 12.5 mm diameter x 20 mm height. The cylindrical samples were then heated to the ferrite/austenite region in a salt bath furnace at 745^{o}C for 4 minutes followed by quenching in water. This heating process produces the typical ferrite/martensite structure of dual phase steels. The microstructure of the produced dual-phase steel samples consisted of about 25% volume fraction of martensite and the remaining was assumed to be mainly ferrite. The volume fraction of the martensite phase was estimated by means of point counting method (ASTM-E562-02, 2002). The average grain size of the ferrite phase was about 90 μm. Figure 5.1(a) shows the stress-strain responses of the initial low carbon steel and the produced dual-phase steel under simple compression. The yield strength of the dual-phase steel is estimated to be 500 MPa using the 0.2% offset strain method (Popov, 1998). The optical micrograph of the dual-phase steel sample is shown in Figure 5.1 (b).

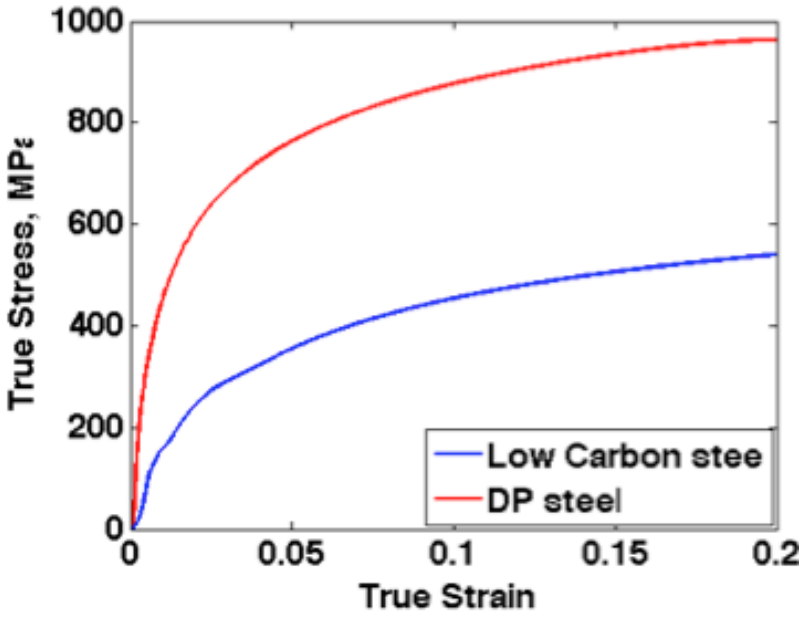

(a)

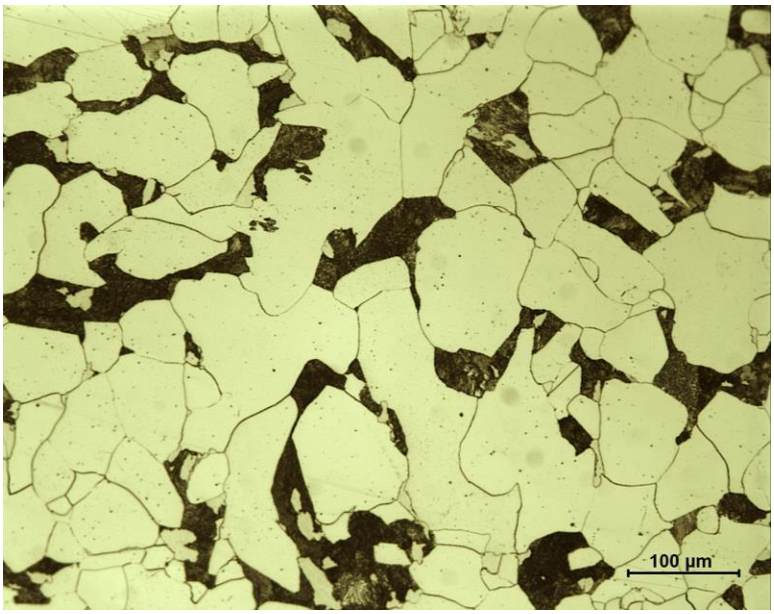

(b)

Figure 5.1: (a) True stress-true strain responses of low carbon and dual-phase steel samples in simple compression; (b) an optical micrograph of the dual-phase steel sample used in this study.

The samples were carefully prepared for nanoindentation testing and OIM measurements. After grinding using silicon carbide papers with different particle sizes from 320 to 2400 mesh, the samples were polished using 9 μm, 3 μm, and 1 μm diamond suspensions in conjunction with several intermediate etches by 2% Nital. The samples were subsequently electropolished using 5% perchloric acid and 95% acetic acid for 90 seconds at 15 ^{o}C and 65 volts. The last electropolishing step was found essential to produce a high-quality surface finish that is especially required for nanoindentation experiment. Nanoindentations were carried out using a nanoindenter (G200 Nano Indenter equipped with the continuous stiffness measurement (CSM) system) with 20 μm radius spherical diamond tip. The indentation tests were carried out under load control condition. The locations of the indents were chosen in the middle of ferrite grains in the dual phase steel samples to reduce the chances of any possible effect from grain boundaries or phase interfaces on the measurements. The fact that the indentation yield points in most of our tests on the ferrite phase were observed to occur after only a few nanometers (20-30 nm) of indentation depth reduces the effect of grain boundary on the measurements when indenting in the middle of the ferrite grain. This is justified by realizing that the value of the contact radius at the indentation yield points was estimated to be less than 1 μm (0.6-0.8 μm), which is much smaller than the average grain size of the ferrite phase (~90 μm). However, it should be noted that there is still a chance for the existence of a grain boundary just below the surface at the indentation site. Finally, the crystal orientations of the indented grains were measured using OIM technique based on electron backscatter diffraction (EBSD) analysis.

5.3 Review of Data Analysis Method for Spherical Nanoindentation

The measured load-displacement data are converted to indentation stress-strain curves following the approach described in Ref. (Kalidindi and Pathak, 2008). The main two steps in this data analysis protocol are briefly summarized below. The first step is an accurate estimation of the initial point of effective contact between the indenter and the sample such that Hertz theory (Hertz, 1896; Johnson, 1985) is satisfied for the initial elastic loading segment. This can be obtained from the measured load signal $(\tilde{P})$, measured displacement signal $(\tilde{h}_e)$, and CSM signal (S) using the following relation:

$$S = \frac{3\,P}{2\,h_e} = \frac{3\,(\tilde{P} - P^*)}{2\,(\tilde{h}_e - h^*)} \tag{5.1}$$

where P^* and h^* are the load and displacement at the initial point of effective contact, respectively. A least square fit between $\left(\tilde{P} - \frac{2}{3}\tilde{h}_e\,S\right)$ and S for the data in the initial loading segment produces the best estimates of P^* and h^*. In the second step, the indentation stress σ_{ind} and indentation strain ε_{ind} are calculated by recasting Hertz theory as

$$\sigma_{ind} = E^*\ \varepsilon_{ind}, \qquad \sigma_{ind} = \frac{P}{\pi\,a^2}, \qquad \varepsilon_{ind} = \frac{4}{3\pi}\frac{h_e}{a} \simeq \frac{h_e}{2.4\,a} \tag{5.2}$$

where P and h_e are the measured indentation load and measured elastic displacement corrected for the initial point of contact, E^* is the effective Young's modulus, and a is the contact radius defined as

$$a = \left(\frac{3\,P\,R^*}{4\,E^*}\right)^{1/3} = \frac{S}{2\,E^*}, \qquad \frac{1}{E^*} = \frac{1-\nu_s^2}{E_s} + \frac{1-\nu_i^2}{E_i} \tag{5.3}$$

where ν and E are Poisson's ratio and Young's modulus, and the subscripts s and i refer to the sample and the indenter, respectively. The estimation of the contact radius, a, requires the knowledge of the effective Young's modulus E^*. The value of E^* can be determined experimentally from the initial elastic loading segment using Hertz theory as

$$h_e = \left(\frac{3\,P}{4\,E^*\sqrt{R^*}}\right)^{2/3}, \qquad \frac{1}{R^*} = \frac{1}{R_s} + \frac{1}{R_i} \tag{5.4}$$

where R^* is the effective radius, which is equal to the indenter radius R_i for purely elastic indentation since the sample radius R_s approaches infinity. Then, a least square fit between h_e and $P^{2/3}$ for the initial elastic loading portion of the data produces the best estimate of E^*.

5.4 Finite Element Model of Spherical Nanoindentation

A three-dimensional FE model was developed to simulate the spherical indentation process using the commercial FE package ABAQUS (ABAQUS, 2010). The size of the sample was assumed to be 20 μm x 20 μm x 15 μm consisting of 91,512 cuboid-shaped three dimensional eight-noded solid elements (C3D8). To accurately capture the heterogeneous stress and strain fields in the indentation zone, the highest mesh densities of the FE mesh were obtained in the region under the indenter tip. For this reason and to

reduce the total number of elements and computational cost, the sample was discretized into five regions with an extremely fine mesh resolution under the indenter tip as shown in Figure 5.2. The mesh refinement from one region to another was achieved using the bilinear multi-point constraint (MPC) option in ABAQUS on the boundaries between the regions of different mesh densities. The size of the element under the indenter tip was 4.8 nm x 4.8 nm x 5.9 nm. The indenter (not shown in Figure 5.2) was modeled using an analytical rigid hemi-spherical surface with a radius of 20 μm (same as the size of the indenter used in the experiments). It should be noted that in real experiment the indenter is not rigid and has a finite Young's modulus. In our experiment, the indenter tip is made of diamond with a Young's modulus of ~ 1.2 GPa. However, the elasticity of the indenter is accounted for by using the effective Young's modulus (see Eq. (5.3)), which includes the elastic properties of both the indenter and the sample. In other words, by using the effective Young's modulus in the analysis of the indentation data, we can relate the predicted results from the FE model (here the Young's modulus of the indenter is $E_i = \infty$) with the corresponding measured values form the experiments (here $E_i \approx 1.2$ GPa). A hard surface-to-surface, frictionless contact was assumed between the sample and the indenter. A vertical displacement boundary condition was imposed on the indenter. The bottom surface of the sample was constrained along the z-direction (indentation direction). The displacement of the indenter and the total force applied on the sample are reported from the simulation at every time increment.

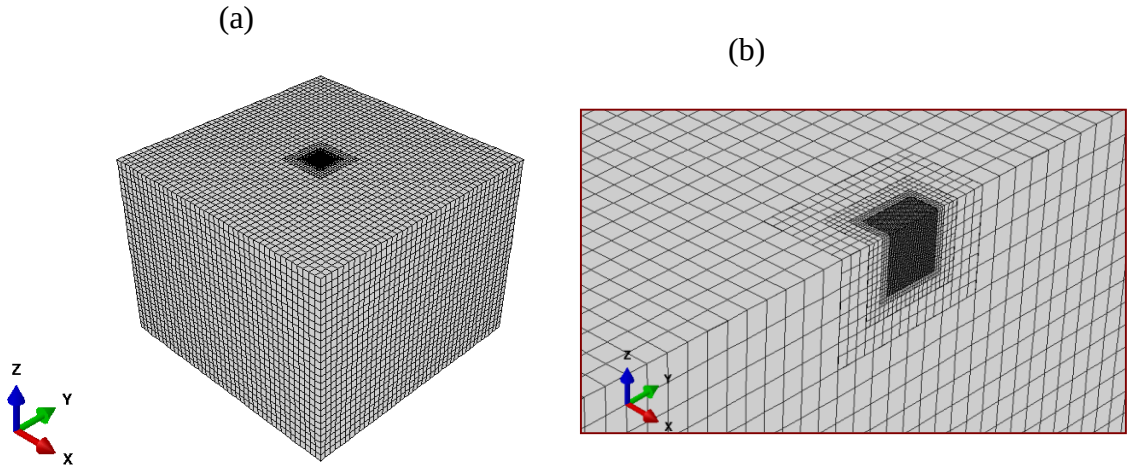

Figure 5.2: (a) FE mesh of the sample in the spherical nanoindentation model, (b) close-up view of the region under the indenter tip.

The FE model developed in this study was validated by comparing the predicted load-displacement curve against the corresponding theoretical result from Hertz theory for purely elastic deformation of an isotropic material (see Eq. (5.4)). The prediction from the FE model was in excellent agreement with the Hertzian result as shown in Figure 5.3. The Young's modulus and Poisson's ratio of the sample for this example were assumed to be 200 GPa and 0.3, respectively.

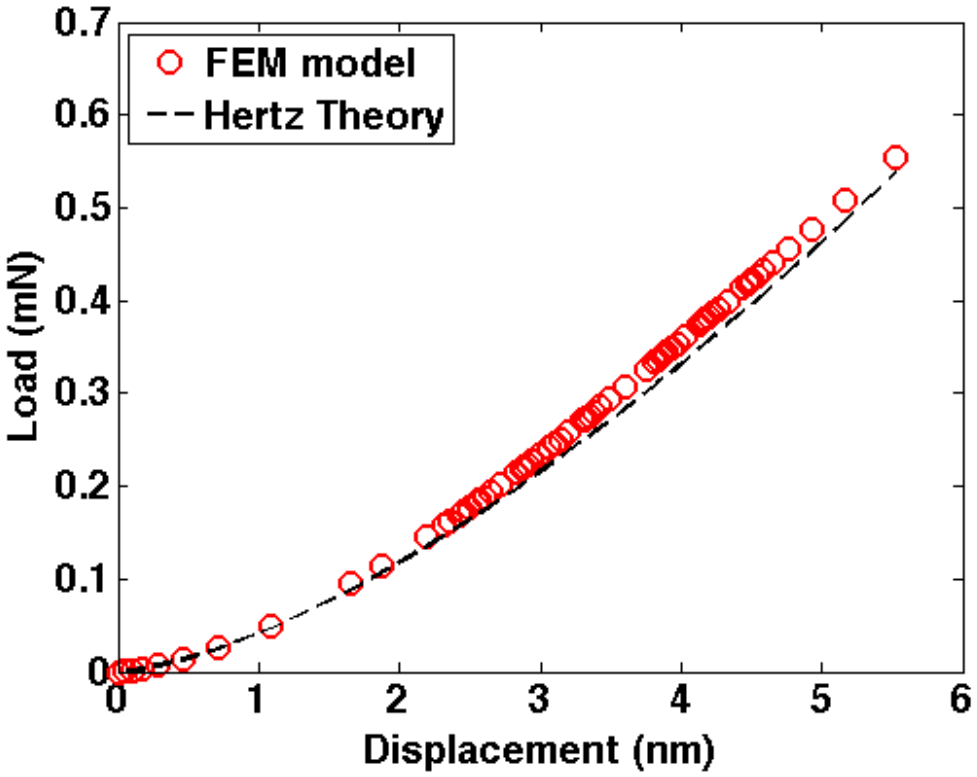

Figure 5.3: Comparison of the predicted load-displacement response from FE simulation against the corresponding prediction from Hertz theory.

In this work, the predicted indentation stress and strain from the FE simulations were also calculated using Eq. (5.2). However, once the plastic deformation initiates under the indenter, the value of the effective radius R^* needs to be computed in order to calculate the contact radius a (see Eq. (5.3)). The value of R^* can be estimated from an elastic unloading segment by rewriting Eq. (5.4) as

$$h_e = h_t - h_r = \left(\frac{3\,P}{4\,E^*\sqrt{R^*}}\right)^{2/3} \tag{5.5}$$

where h_t denotes the total displacement, and h_r refers to the residual displacement upon unloading. The value of R^* that corresponds to the peak load just before unloading can then be determined from a least square fit between h_t and $P^{2/3}$. Since the contact radius evolves continuously with deformation, a large number of unloading segments at several points on the loading segment need to be applied. Note that experimentally, one can directly estimate the value of the contact radius from Eq. (5.3) with the aid of CSM signal.

Since the value of the indentation yield strength from the FE simulations is the main variable that affects the predicted critical resolved shear stress value in this work, we carefully studied the effect of mesh densities on the predicted FE results. This was achieved by comparing the predicted indentation yield points from the current FE model with two other FE models with different mesh densities. The sizes of the element under the indenter tip for the two new FE models were (3.0 nm x 3.0 nm x 3.1 nm) and (2.2 nm x 2.2 nm x 2.4 nm). The corresponding numbers of elements were 133,616 and 199,864, respectively. Note that these two FE models have higher mesh densities under the indenter tip compared to the original model that consists of 91,512 elements. An isotropic elastic-plastic spherical indentation deformation was simulated using these three different FE models. The inputs to the FE simulations include the yield strength, Young's modulus, and Poisson's ratio, which were assumed to be 0.045 GPa, 70 GPa, and 0.3, respectively. A non-hardening behavior of the sample in plastic deformation was assumed in these simulations. The predicted stress-strain responses from the three FE models are shown in Figure 5.4. It is clear that that increasing the mesh densities has negligible effect on the predicted results.

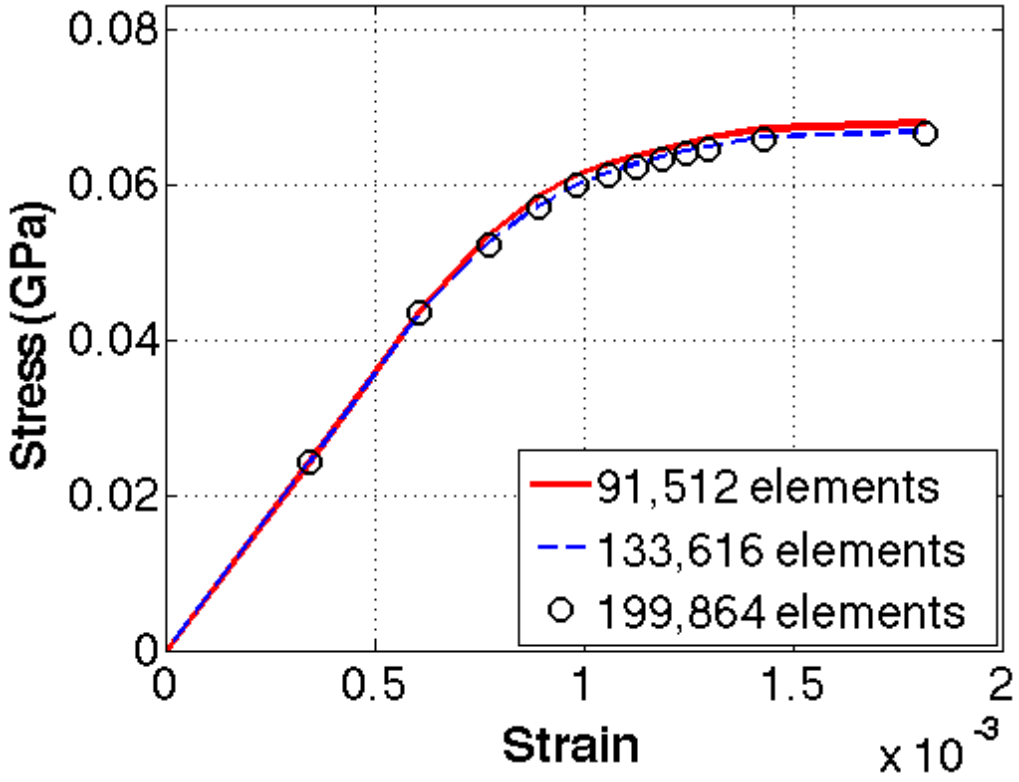

Figure 5.4: Comparison of the predicted stress-strains responses from three FE models with different mesh densities.

5.5 Results and Discussions

As described earlier, nanoindentation measurements were conducted in the middle of the ferrite phase in a dual phase steel sample using 20 μm radius spherical diamond tip. The orientations of the indented grains were measured using OIM technique. The indentation load-displacement curves were converted to indentation stress-strain curves using the recently developed data analysis approach described in Section 5.3. In the present study, the occurrence of large displacement bursts or "pop-ins" were observed in

all of the measurements. These pop-ins are commonly attributed to the difficulty of activating dislocation sources in the indentation zone as explained in more detail by Pathak et al. in Ref. (Pathak et al., 2009a). The occurrence of these large pop-ins makes it difficult to extract reliable values of the indentation yield points. As an example, it would be very difficult to extract the values of the indentation yield points from the indentation stress-strain curves shown in Figure 5.5. For this reason, only few number of measurements that have relatively small pop-ins were considered in this study. The indentation stress-strain curves and OIM scans for some of these measurements are depicted in Figure 5.6. It is observed that the measurements in each grain are consistent with each other after the occurrence of the pop-ins.

The values of the measured indentation yield points were estimated using a back-extrapolation method as shown in Figure 5.7. Table 5.2 summarizes the values of the effective indentation modulus E^* and indentation yield points for the measurements shown in Figure 5.6. It is observed that the indentation yield point for grain #3 (~1.05 GPa) is slightly higher than those obtained for grains #2 and 3 (~ 0.93 GPa). In general, the values of the indentation yield points for the grains studied in this work are close to each other. This can be explained by the small difference in the values of orientations between these grains. In order to extract more reliable values of the critical resolved shear stress, more indentation measurements should be conducted in the ferrite phase on a wider range of orientations.

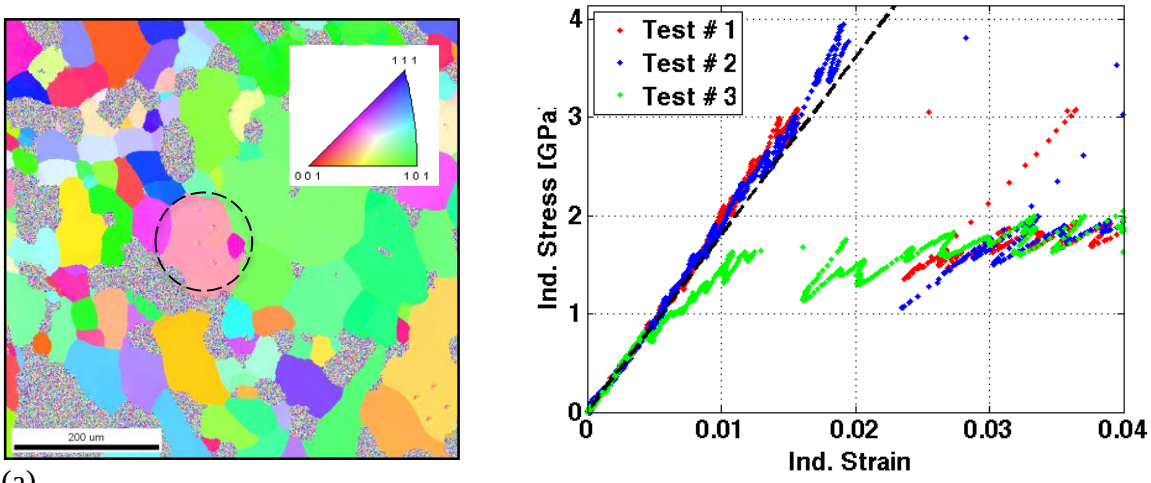

(a) (b)

Figure 5.5: (a) Inverse pole figure map obtained on a sample of dual phase steel showing the location of an indented grain in the ferrite phase, (b) the measured indentation stress-strain curve showing large displacement bursts or "pop-ins".

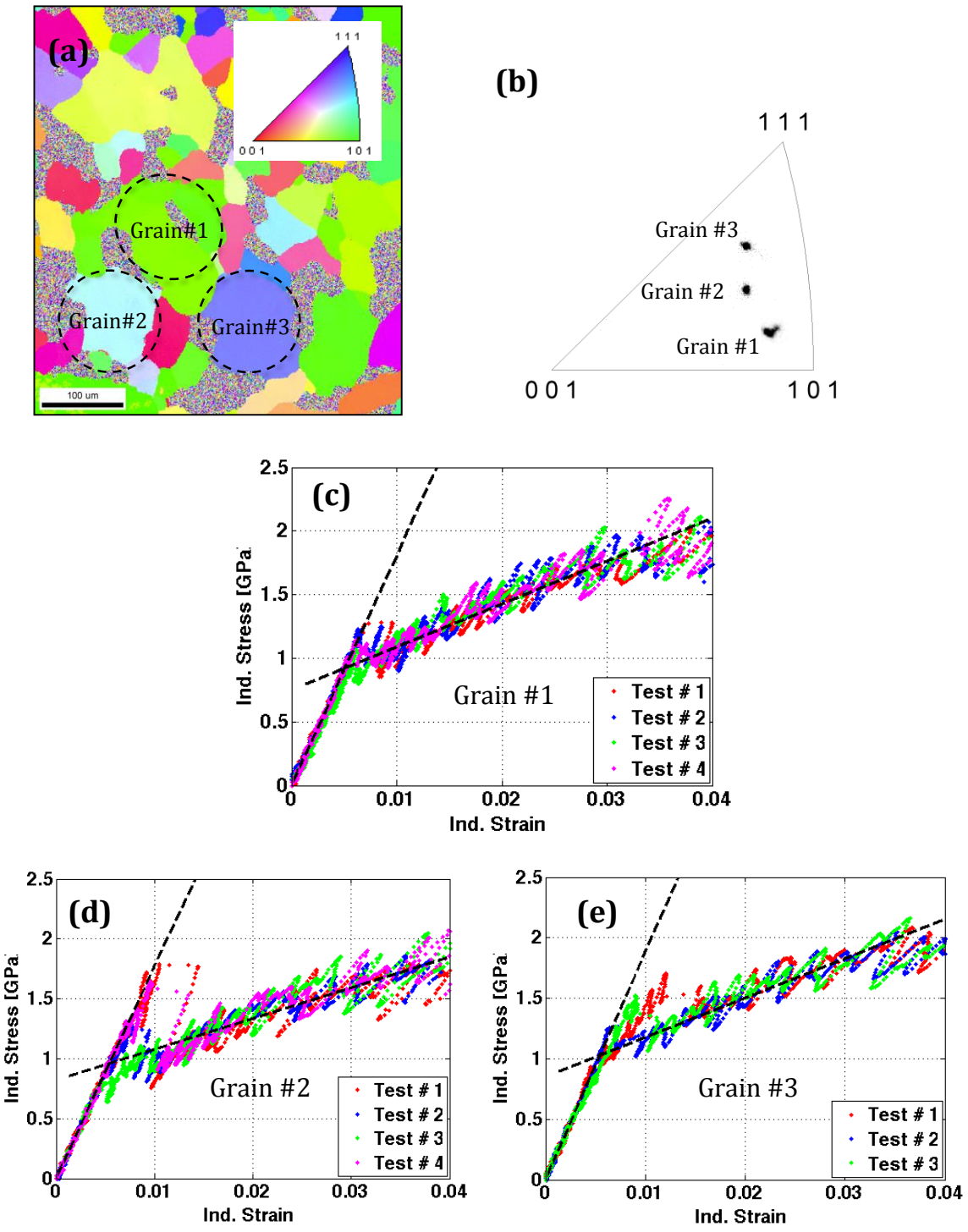

Figure 5.6: (a) OIM scan and (b) (001) inverse pole figure map obtained on a sample of dual phase steel showing the location of three indented grains in the ferrite phase. The measured indentation stress-strain curves on these grains are shown in (c), (d), and (e).

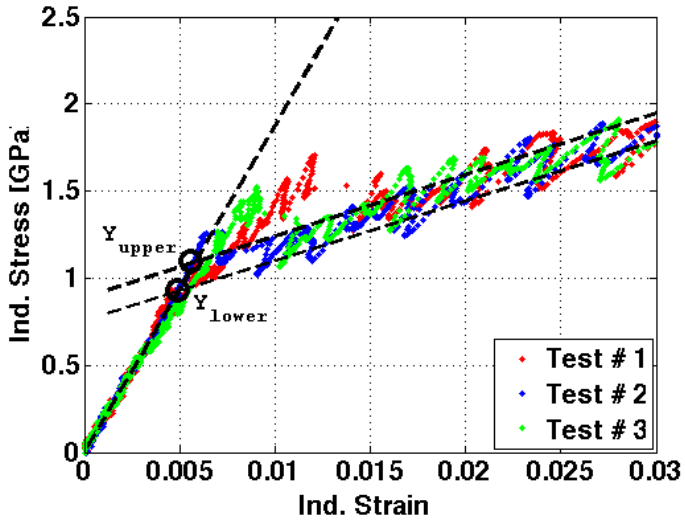

Figure 5.7: The back-extrapolation method used in the current study to estimate the range of the indentation yield points [Y_{lower} -Y_{upper}] from the indentation stress-strain curves.

Table 5.2: An estimation of the effective indentation stiffness and the indentation yield points for the measurements shown in Figure 5.6. The values of the measured orientations for the grains are also shown in terms of Bunge-Euler angles $(\varphi_1, \phi, \varphi_2)$.

Grain #	Orientation $(\varphi_1, \phi, \varphi_2)$	Effective modulus E^* (GPa)	Indentation yield range (GPa)
1	(53.58, 37.26, 351.02)	~ 180	0.8-1.05
2	(269.6, 36.9, 67.4)	~ 182	0.85-1.05
3	(32.23, 40.16, 302.83)	~ 190	0.93-1.1

In order to extract the values of the critical resolved shear stress for the ferrite phase from the measurements shown in Figure 5.6, spherical nanoindentation was simulated using CPFEM. The classical crystal plasticity constitutive equations described in Section 2.1 were used in the current work. In the FE model described earlier, all integration points were assigned a single crystal orientation. It is assumed that there is no hardening prescribed in the material response for this simulation. The value of the strain rate sensitivity parameter was taken as 0.01. The three elastic constants of the ferrite phase was assumed to be similar to those obtained in pure Fe: $C_{11} = 231.4$ GPa, $C_{12} = 134.7$ GPa, and $C_{44} = 116.4$ GPa.

The indentations of the three crystal orientations listed in Table 5.2 were simulated in this work. The indentation stress-strain curves calculated from the outputs of the FE simulations were calibrated against the corresponding measurements shown in Figure 5.6. More specifically, the value of the initial slip resistance was modified until the predicted indentation yield points matched the corresponding measured values. In the current study, the values of the predicted indentation yield points from the CPFEM simulations were assumed to occur when the curves started to deviate from the initial elastic segment. It should be noted that this method for estimating the predicted indentation yield point is different from the back-extrapolation method used earlier to estimate the indentation yield points from the measured stress-strain curves. As explained earlier, the reason for using the back-extrapolation method in the indentation measurements is because of the occurrence of pop-ins, which makes it impossible to find the stress points at which the curves started to deviate from linearity. Thus, caution should be exercised when interpreting the values of the initial slip resistance reported in

this study. Figure 5.8 shows the predicted indentation stress-strain curves from CPFEM for the three grains shown in Figure 5.6 (a). The corresponding predicted values of the effective indentation stiffness and the indentation yield points are shown in Figure 5.6 (b). The value of the initial slip resistance used in the CPFEM was 330 MPa. This value is assumed to be the critical resolved shear stress of the ferrite phase in the dual phase steel sample used in this study. Two important points need to be noted. First, it is emphasized here that the value of the initial slip resistance was estimated based on the indentation measurements conducted on three grains only (see Figure 5.6). It is clear that more indentation measurements are required to extract a more reliable value of the critical resolved shear stress. Second, the value of the extracted initial slip resistance from nanoindentation is very high compared to the reported values in Table 5.1, which were obtained using different methods. This can be attributed to the effect of indentation size effect which results in a higher indentation yield strengths (Elmustafa and Stone, 2003; Nix and Gao, 1998; Qu et al., 2006). This will affect the estimated value of the initial slip resistance since it is extracted based on the direct calibration of the predicted stress-strain curves from the FE model against the corresponding indentation measurements. Therefore, the value of the initial slip resistance reported here cannot be used directly in the simulation of the bulk sample. An additional study would be required to take the effect of indentation size effect on the extracted slip hardening parameters from nanoindentation before using these values in the crystal plasticity models for simulating the mechanical behavior of the bulk sample.

(a)

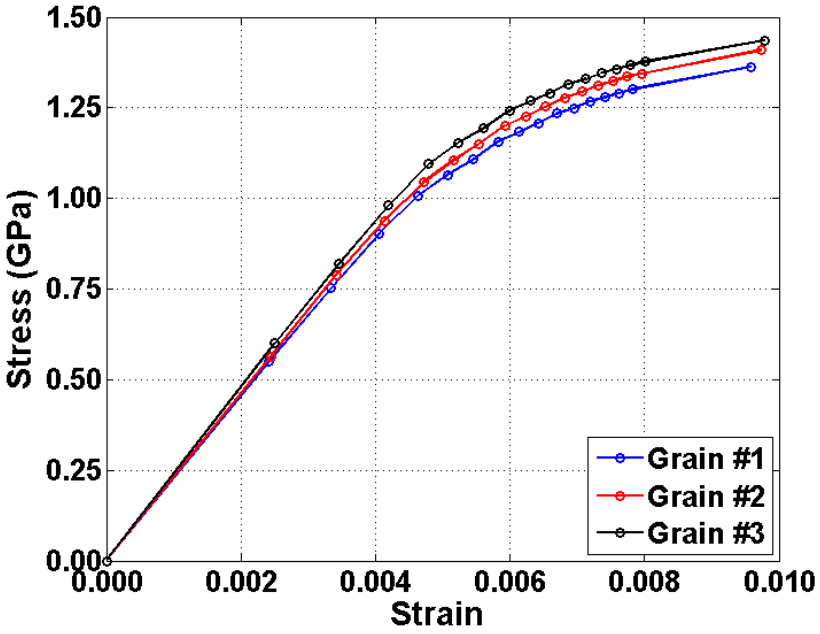

(b)

Grain #	Orientation $(\varphi_1, \phi, \varphi_2)$	Effective modulus E^* (GPa)	Indentation yield points (GPa)
1	(53.58, 37.26, 351.02)	182	~ 1.0
2	(269.6, 36.9, 67.4)	186	~ 1.05
3	(32.23, 40.16, 302.83)	192	~ 1.12

Figure 5.8: (a) The predicted indentation stress-strain curves from CPFEM for the three indented grains shown in Figure 5.6. (b) The predicted values of the effective indentation stiffness (estimated from the first unloading segment) and the indentation yield points (corresponding to the stress values at which the curves started to deviate from linearity) for the same grains.

CHAPTER 6

CONCLUSIONS AND RECOMMENDATIONS

6.1 Conclusions

This thesis has mainly focused on addressing the high computational cost associated with implementing crystal plasticity models in a FE simulation tool. This has been tackled by integrating the recently developed DFT-based spectral crystal plasticity databases with a commercial FE tool to conduct more efficient CPFEM simulations. These recently developed computationally efficient DFT representations were found to speed up the crystal plasticity computations by several orders of magnitude in FCC metals. The new spectral database CPFEM developed in this thesis has shown to be able to speed up the computation time by about 40 times compared to the classical CPFEM when using a small set of dominant DFTs. Furthermore, an important application of CPFEM for the extraction of the initial slip resistance in dual phase steels has been demonstrated in this thesis. More specifically, a combined application of CPFEM, spherical nanoindentation, and OIM has been used to estimate the critical resolved shear stress of the ferrite phase in dual phase steel. In summary, the following results have been accomplished in the current thesis:

1. The recently developed spectral crystal plasticity databases have been extended to other material systems. In particular, a new spectral crystal plasticity database using discrete Fourier transforms (DFTs) was established and validated for BCC metals with 48 slip systems. It was seen that a small number of dominant DFTs is

enough to capture the dependence of the stresses, the lattice spins, and the total slip rate in individual crystals on their lattice orientation and the applied deformation modes. Another new spectral crystal plasticity database was also developed for HCP metals for only two slip resistance ratios. It was assumed that the HCP crystals deform solely by slip. These spectral databases were successfully applied to a rigid-viscoplastic polycrystal Taylor-type model to predict the texture evolution and stress-strain response for a few selected examples of deformation processes. As previously reported, the DFT-based spectral approach was found to be able to speed up the crystal plasticity computations by about two orders of magnitude compared to the classical approach. As a specific application of these novel databases, a new efficient approach was developed for the fast computation of the yield surfaces in the five-dimensional deviatoric stress space for both BCC and FCC metals using the Taylor polycrystal plasticity models. This new approach was validated by comparing the stress values on some selected projections of the yield surface produced using the new spectral approach against the corresponding results from the conventional crystal plasticity approach. As another application of these novel databases, a new class of first-order cubic-triclinic plastic property closures were delineated for both FCC and BCC metals. It was observed that the assumption of orthorhombic sample symmetry reduces the design space and eliminates some of the optimal solutions in the design of materials with improved performance characteristics.

2. The spectral database approach was successfully implemented in a commercial finite element code to permit computationally efficient simulations of heterogeneous deformations using crystal plasticity theories. More specifically, the spectral database approach to crystal plasticity solutions was successfully integrated with the commercial finite element package ABAQUS through a user materials subroutine, UMAT. Details of this new spectral database CPFEM were demonstrated and validated through a few example case studies for selected deformation processes on FCC and BCC metals. The evolution of the underlying crystallographic texture and its associated macroscale anisotropic properties predicted from this new approach were compared against the corresponding results from the conventional CPFEM. It was observed that implementing the crystal plasticity spectral database in a FE code produced excellent predictions similar to the classical CPFEM, but at a significantly faster computational speed and much lower computational cost. It has been shown that the new spectral database CPFEM developed in this thesis can speed up the simulation time by about 40 times compared to the traditional CPFEM.

   For integrating the spectral databases with the FE tool, the following two tasks were accomplished:

   2.1. A new computational scheme was developed for extending the crystal plasticity calculations using spectral databases from rigid-viscoplastic into elastic-viscoplastic behavior. This was accomplished through the

development of a new efficient modified Newton-Raphson scheme that decomposed the total stretching tensor into elastic and plastic parts at each integration point for every crystal orientation. This decomposition was typically obtained within 2-4 iterations; a higher number of iterations were generally required near the elastic-plastic transition zone or during any loading path change. The stability and accuracy of the this new iteration scheme were verified by simulating a reverse shearing process using both the spectral database CPFEM approach and comparing the results with those obtained from the classical CPFEM approach (Kalidindi et al., 1992).

2.2. A new analytical expression for the Jacobian matrix required to implement the spectral databases with any implicit finite element code was developed. The derived analytical expressions for each of the terms in the Jacobian were validated by comparing the values produced from these expressions with the corresponding values computed numerically by slightly perturbing the independent variable in each expression.

3. The viability of the recently developed data analysis approach of spherical nanoindentation for extracting the crystal plasticity slip parameters in multiphase materials was demonstrated in this thesis. More specifically, a combined application of spherical nanoindentation, OIM, and CPFEM was used for extracting the critical resolved shear stress of the ferrite phase in dual phase steels.

6.2 Recommendations for Future Work

The main contribution of the current thesis is the development of a new user materials subroutine, UMAT, for conducting more efficient CPFEM simulations using the spectral crystal plasticity databases. The remarkable savings in the FE simulation time observed in the case studies presented in this thesis provide a significant incentive for applying the spectral database CPFEM to large-scale applications such as metal forming operations. Several enhancements can be made to further speed up the calculations in the current spectral database UMAT. For example, a spectral representation of the Jaumann rate elasticity relation used in this work to include the elastic deformation can enhance the computational efficiency of the iteration scheme for decomposing the strain rate tensor into elastic and plastic parts at every integration point in the finite element mesh. In particular, the dependence of the fourth-rank elasticity tensor on the crystal lattice orientation can be efficiently computed using a spectral database approach. Also, several expressions in the Jacobian matrix depend on the crystal lattice orientations and can be efficiently computed using spectral databases. Furthermore, in the current version of the spectral database UMAT, the crystallographic texture is updated after every time increment in the FE simulation regardless of the amount of plastic strain increment at that time step. However, the updated texture would not change much if the imposed plastic strain increment were very small. Therefore, one can save significant computational time by avoiding updating the texture after every plastic strain increment. It would then be necessary to keep track of the plastic strains after every time increment and update the texture only when the accumulated plastic strains reach a critical value.

The spectral database CPFEM described in this thesis has been applied to FCC and BCC metals that are assumed to be solely deformed by slip. It would be highly valuable to extend the application of this approach to HCP metals in which both slip and twining can occur. The spectral representations described in Chapter 3 for HCP metals have only been applied to two slip resistance ratios and without including twining. However, it is known that twining is an important deformation mechanism in most HCP metals such as pure magnesium. Several modifications need to be applied to the current spectral database approach depending on the selected formulations for incorporating twining in the crystal plasticity models. For example, it would be necessary to establish additional spectral representations for the twin volume fractions and the total shearing rates on the different slip systems (prism, basal, and pyramidal) when using the constitutive framework described by Kalidindi et al. in Ref. (Kalidindi, 1998; Salem et al., 2005). In this case, the spectral representations for the functions of interest depend on the crystal lattice orientation, applied deformation mode at the crystal level, and the values of slip and twin resistance, i.e. the domain of the functions increase from four-dimensional space in the case of cubic system to eight-dimensional space for HCP crystal. This clearly requires significant additional computational effort to build the spectral databases but it is a one-time computational cost.

The last part of this thesis has focused on applying spherical nanoindentation, CPFEM, and OIM for extracting the critical resolved shear stress of the ferrite phase in dual phase steels. Most of the indentation tests discussed in this thesis were conducted on grains that have similar crystal orientations. In order to extract reliable values of the slip resistance, additional tests should be conducted on a wider range of orientations. In

addition, all of the indentation test points reported in this thesis were chosen at the middle of the ferrite grains far from the grain boundaries or the ferrite/martensite interfaces. It would be extremely valuable to perform indentations at different regions in the ferrite phase and at different deformation levels. This will help to quantitatively examine the microscale heterogeneities present in this complex two-phase material by measuring the local mechanical response at different regions in the ferrite matrix. It should be noted that a higher dislocation density has already been observed by transmission electron microscopy (TEM) and high resolution electron backscattered diffraction (EBSD) close to the ferrite/martensite interface in dual phase steel samples (Calcagnotto et al., 2010; Kadkhodapour et al., 2011b; Korzekwa et al., 1984; Sarosiek and Owen, 1984). This is commonly attributed to the austenite-martensite transformation that is associated with 2-4% volume change (Grushko and Weiss, 1989; Korzekwa et al., 1980; Nagorka et al., 1987; Paruz and Edmonds, 1989; Sakaki et al., 1983; Watt and Jain, 1984). However, it is not yet clear how these dislocations evolve with deformations and how they contribute to the observed excellent mechanical properties in dual phase steels such as high work hardening rates.

APPENDIX A

MULTI-SCALE FE SIMULATIONS USING MATERIAL KNOWLEDGE SYSTEMS

This appendix describes the first implementation of the novel localization relationships, formulated in the recently developed mathematical framework called materials knowledge systems (MKS) (Fast and Kalidindi, 2011; Fast et al., 2011; Kalidindi et al., 2010; Landi and Kalidindi, 2010; Landi et al., 2009), into the commercial FE package ABAQUS to enable hierarchical multiscale materials modeling (Al-Harbi et al., 2012). The viability and computational advantages of this new approach, called MKS-FE approach, are demonstrated through a simple case study involving the elastic bending of a cantilever beam made from a composite material by including the microstructure features at each material point in the FE model. Below is a brief review of the MKS framework (Binci et al., 2008; Kalidindi et al., 2008) and its integration with the FE package ABAQUS through a user material subroutine, UMAT.

Let $\langle \mathbf{p} \rangle$ denote the macroscale imposed variable (e.g. local stress, strain or strain rate tensors) that needs to be spatially distributed in the microstructure as $\mathbf{p_s}$ for each spatial cell indexed by **s**. For many physical quantities of interest, $\langle \mathbf{p} \rangle$ is indeed equal to the volume averaged value of $\mathbf{p_s}$ over the microscale. In the MKS framework, the localization relationship, extended from Kroner's statistical continuum theories (Kroner, 1986; Kröner, 1977), captures the local response field in the microstructure using a set of kernels and their convolution with higher-order descriptions of the local microstructure.

The localization relationship can be expressed as a series sum (Fast and Kalidindi, 2011; Fast et al., 2011; Kalidindi et al., 2010; Landi and Kalidindi, 2010; Landi et al., 2009):

$$\mathbf{p}_{\mathbf{s}} = \left(\sum_{h=1}^{H} \sum_{\mathbf{t} \in \mathbf{S}} \boldsymbol{\alpha}_{\mathbf{t}}^{h} \, m_{\mathbf{s}+\mathbf{t}}^{h} + \sum_{h=1}^{H} \sum_{h'=1}^{H} \sum_{\mathbf{t} \in \mathbf{S}} \sum_{\mathbf{t}' \in \mathbf{S}} \boldsymbol{\alpha}_{\mathbf{t}\mathbf{t}'}^{hh'} \, m_{\mathbf{s}+\mathbf{t}}^{h} m_{\mathbf{s}+\mathbf{t}+\mathbf{t}'}^{h'} + \cdots \right) \langle \mathbf{p} \rangle \tag{A.1}$$

where $m_{\mathbf{s}}^{h}$ is the microstructure function defined as the volume fraction of each distinct local state h in the spatial cell **s**, the kernels $\boldsymbol{\alpha}_{\mathbf{t}}^{h}$ and $\boldsymbol{\alpha}_{\mathbf{t}\mathbf{t}'}^{hh'}$ are referred to as the first-order and second-order influence coefficients, respectively, that are assumed to be completely independent of $m_{\mathbf{s}}^{h}$. The influence coefficients capture the contributions of various microstructure features in the neighborhood of the spatial position **s** to the local response field at that position. The first-order influence coefficients $\boldsymbol{\alpha}_{\mathbf{t}}^{h}$ capture the influence of the placement of the local state h in a spatial location that is **t** away from the spatial cell of interest denoted by **s**. Likewise, the second-order influence coefficients $\boldsymbol{\alpha}_{\mathbf{t}\mathbf{t}'}^{hh'}$ capture the combined effect of placing local states h and h′ in spatial cells that are **t** and $\mathbf{t}'$ away, respectively, from the spatial cell of interest **s**. In this notation, **t** enumerates the bins in the vector space used to define the neighborhood of the spatial bin of interest (Adams et al., 2005), which has been tessellated using the same scheme that was used for the spatial domain of the material internal structure, i.e. $\mathbf{t} \in \mathbf{S}$. A salient feature of the MKS approach is that the influence functions are established such that they are independent of the microstructure topology (Fast and Kalidindi, 2011; Fast et al., 2011; Kalidindi et al., 2010; Landi and Kalidindi, 2010; Landi et al., 2009).

The numerical values of the influence coefficients can be estimated by calibrating the series expansions of Eq. (A.1) to results obtained from micro-mechanics FE models

(Landi et al., 2009). It has been shown that Eq. (A.1) can be transformed into the discrete Fourier transform (DFT), where it can be recast as:

$$\mathbf{P_k} = \left[\left(\sum_{h=1}^{H} \left(\boldsymbol{\beta}_{\mathbf{k}}^{h}\right)^{*} \mathrm{M}_{\mathbf{k}}^{h}\right)\right] \langle \mathbf{p} \rangle$$

$$\boldsymbol{\beta}_{\mathbf{k}}^{h} = \Im_{\mathbf{k}}\left(\alpha_{\mathbf{t}}^{h}\right), \quad \mathbf{P_k} = \Im_{\mathbf{k}}(\mathbf{p_s}), \quad \mathrm{M}_{\mathbf{k}}^{h} = \Im_{\mathbf{k}}\left(\mathrm{m}_{\mathbf{s}}^{h}\right) \tag{A.2}$$

where $\Im_{\mathbf{k}}(\,)$ denotes the DFT operation with respect to the spatial variables **s** or **t**, and the superscript star denotes the complex conjugate. Note that the number of coupled first-order coefficients in Eq. (A.2) is only H, although the total number of first order coefficients still remains as $|\mathbf{S}|$*H. This simplification is a direct consequence of the well-known convolution properties of DFTs (Oppenheim et al., 1999). Because of this dramatic uncoupling of the first-order influence coefficients into smaller sets, it becomes trivial to estimate the values of the influence coefficients $\boldsymbol{\beta}_{\mathbf{k}}^{h}$ by calibrating them against results from FE models. It is emphasized here that establishing $\boldsymbol{\beta}_{\mathbf{k}}^{h}$ is a one-time computational task for a selected composite material system because these coefficients are implicitly assumed to be independent of the morphology of the microstructure. Once the influence coefficients are established for a given composite material system, Eq. (A.2) can be used to compute the spatial distribution of the selected response variables of interest for any microstructure dataset. The procedures for establishing the influence coefficients were discussed in prior work (Fast and Kalidindi, 2011; Fast et al., 2011; Kalidindi et al., 2010; Landi and Kalidindi, 2010; Landi et al., 2009).

The MKS framework described above was integrated with the commercial finite element package ABAQUS through a user materials subroutine. In this MKS-FE

simulation, each material point in the macroscopic FE model is associated with a representative three-dimensional microstructure at that location. In this novel approach, information is consistently exchanged between the microscale and macroscale in a fully coupled manner. In other words, the MKS approach is used to compute the microscale spatial distribution of the stress and strain fields at each material point in the macroscopic FE model, and the homogenized (volume-averaged) stress field from the microscale is transferred to the macroscale FE analyses at the component scale. The microscale stress and strain tensors in each spatial cell **s** are calculated using the MKS approach as:

$$\boldsymbol{\varepsilon_s} = \boldsymbol{\mathcal{L}_s}\langle\boldsymbol{\varepsilon}\rangle = \Im_{\mathbf{k}}^{-1}\left(\sum_{h=1}^{H} M_{\mathbf{k}}^{h}\, \boldsymbol{\beta}_{\mathbf{k}}^{*h}\right)\langle\boldsymbol{\varepsilon}\rangle \tag{A.3}$$

$$\boldsymbol{\sigma_s} = \sum_{h=1}^{H} m_{\mathbf{s}}^{h}\, \mathbb{C}^{h}\boldsymbol{\varepsilon_s} \tag{A.4}$$

where $\langle\boldsymbol{\sigma}\rangle$ and $\langle\boldsymbol{\varepsilon}\rangle$ denote the macroscale stress and strain tensors defined at an integration point in the FE mode, $\mathbb{C}^{h}$ represents the 4th-order elasticity tensor for the local state h, $\boldsymbol{\mathcal{L}_s}$ is the 4th-rank localization tensor, and $\Im_{\mathbf{k}}^{-1}$ denotes the inverse DFT operator that transforms from the Fourrier space (**k**) to the real space (**s**). The implementation of UMAT in ABAQUS also requires the computation of the Jacobian defined as

$$\mathbf{J} = \frac{\partial(\Delta\langle\boldsymbol{\sigma}\rangle)}{\partial(\Delta\langle\boldsymbol{\varepsilon}\rangle)} = \frac{1}{|\mathbf{S}|}\sum_{\mathbf{s}\epsilon\mathbf{S}}\sum_{h=1}^{H} m_{\mathbf{s}}^{h}\, \mathbb{C}^{h}\boldsymbol{\mathcal{L}_s} \tag{A.5}$$

The microscale stress and strain distributions predicted from the MKS-FE approach were compared with the corresponding predictions from a direct FE simulation with an extremely fine mesh resolution (i.e. a very large number of elements in the FE

model) that allows explicit incorporation of the microstructural details. A simple case study involving the elastic bending of a cantilever beam made from a composite material was selected for this evaluation. Figure A.1 illustrates the main features of the MKS-FE and the direct-FE simulations for the elastic bending of a composite cantilever beam. In the MKS-FE model, the cantilever beam is discretized into 637 cuboid-shaped three dimensional eight-noded solid elements (C3D8) (ABAQUS, 2010). At each integration point inside each element of the mesh, the microstructure is represented by a spatial domain comprising 9261 (21x21x21) cubical voxels that are occupied by one of the two different phases colored black and white in the figure. In this simulation, the macroscale strain tensor provided by ABAQUS at each integration point is used to calculate the microscale strain and stress tensors at each cell in the microstructure. Then, the volume-averaged stress tensor along with the Jacobian matrix is passed up to the macroscale FE analyses. In the direct-FE simulation, each element in the MKS-FE model is further discretized into 21x21x21 elements as shown in Figure A.1 (b) resulting in a total of 5,899,257 3-D solid elements (C3D8). The elements in each 21x21x21 block of elements are assigned the same 3-D microscale structure and local properties as the microscale RVEs used in the MKS-FE simulation.

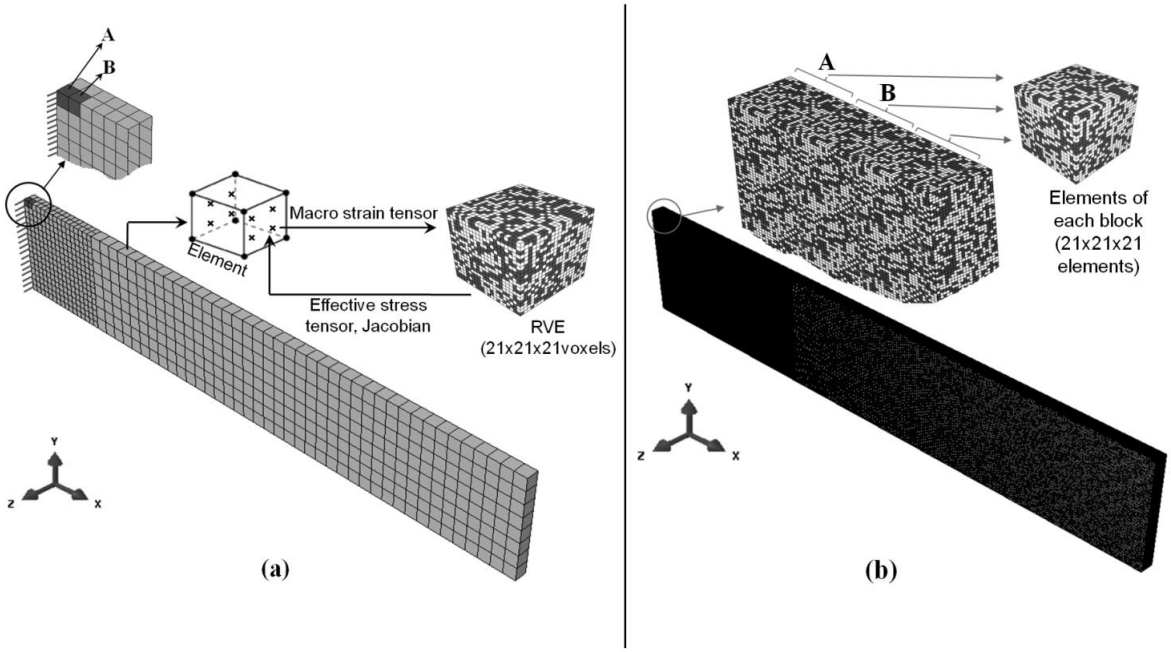

Figure A.1: FE model of the cantilever beam bending problem: (a) a schematic of how the MKS approach is integrated with the FE package ABAQUS in the form of a user material subroutine (UMAT), referred to as MKS-FE approach, and (b) a direct FE model of the cantilever beam used to validate the MKS-FE approach. Each element in the MKS-FE model shown in (a) is discretized into 21x21x21 elements in the direct FE model shown in (b). The elements in each 21x21x21 block of elements are assigned the same 3-D microscale structure and local properties as the microscale RVEs used in the MKS-FE model.

A two-phase composite material was selected for the present study. The two phases are assumed to exhibit isotropic elastic behaviour with Young's moduli of 200 GPa and 300 GPa, respectively. The value of the Poisson's ratio is assumed to be 0.3 for both phases. In this case study, two different microstructures were selected to validate the MKS-FE approach. The first microstructure was constructed by random placement of the

individual phases in the microstructure as depicted in Figure A.2 (a), and is referred to as the random-microstructure. The random-microstructure with its rich diversity of local neighborhoods produces the most heterogeneous microscale stress and strain fields in the composite, and offers an excellent opportunity to validate the MKS-FE approach. The second microstructure is made of rods (or short fibers) placed randomly in the microstructure and oriented along the sample x-direction as shown in Figure A.2 (b), and is referred to as the rod-microstructure. The volume fraction of both phases in both microstructures was kept about 50%. For simplicity, the microstructure is assumed to be the same at each integration point in the MKS-FE model.

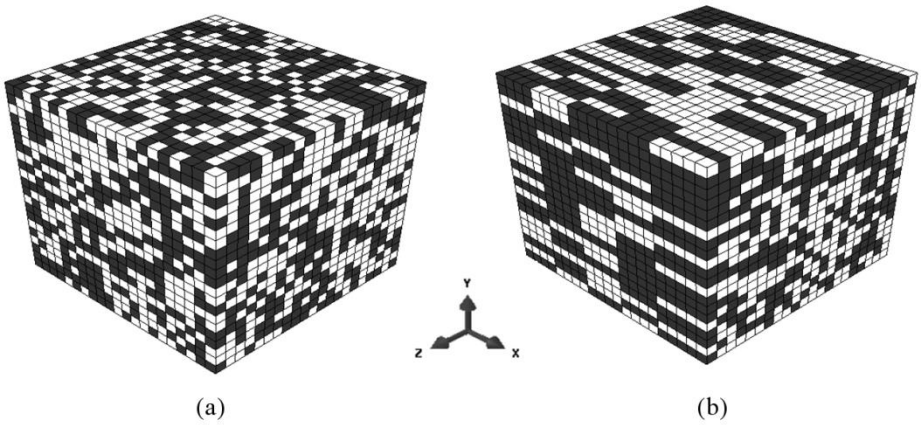

Figure A.2: Details of the two different microstructures used to validate the MKS-FE approach: (a) random, (b) rods (or short fibers) oriented along the x-direction.

The goal in the present study is to critically validate the MKS-FE approach by comparing the spatially resolved microscale stress or strain fields in the MKS-FE model with the stress or strain fields of the corresponding block in the direct FE model. Elements A and B in Figure A.1 (a) have been selected for these comparisons as they represent some of the highest stress locations in the beam. In order to make a meaningful

direct comparison between the MKS-FE results and the direct FE results obtained in this study, the following interpolation scheme is applied for the results obtained from the MKS-FE results. In the MKS-FE model, each material point is assumed to correspond to a 21x21x21 microscale RVE. However, the microscale strain (and stress) distributions are output from the simulation only at each of the eight integration points in the C3D8 elements used in this model. The output microscale distributions at the eight integration points were interpolated using linear shape functions consistent with the C3D8 elements to obtain the microscale distributions at spatial locations corresponding to the centroids of each element in the corresponding block of the direct FE model as shown schematically in Figure A.3. It is important to recognize that this procedure results in the use of different weights for each of the eight integration points for each selected spatial location. Consequently, thee are 9261 microscale distributions for each element of the MKS-FE model. A composite 21x21x21 microscale distribution was assembled from this large set by accepting one value from each microscale distribution as shown in Figure A.3, and used in the direct comparisons with the results from the direct FE model. As an example, the MKS-FE prediction for the microscale strain tensor in spatial cell s = 100 for element A is taken from the spatial cell s = 100 in the interpolated microscale strain distribution at the corresponding spatial cell (i.e. s = 100) in the element A, as shown in Figure A.3.

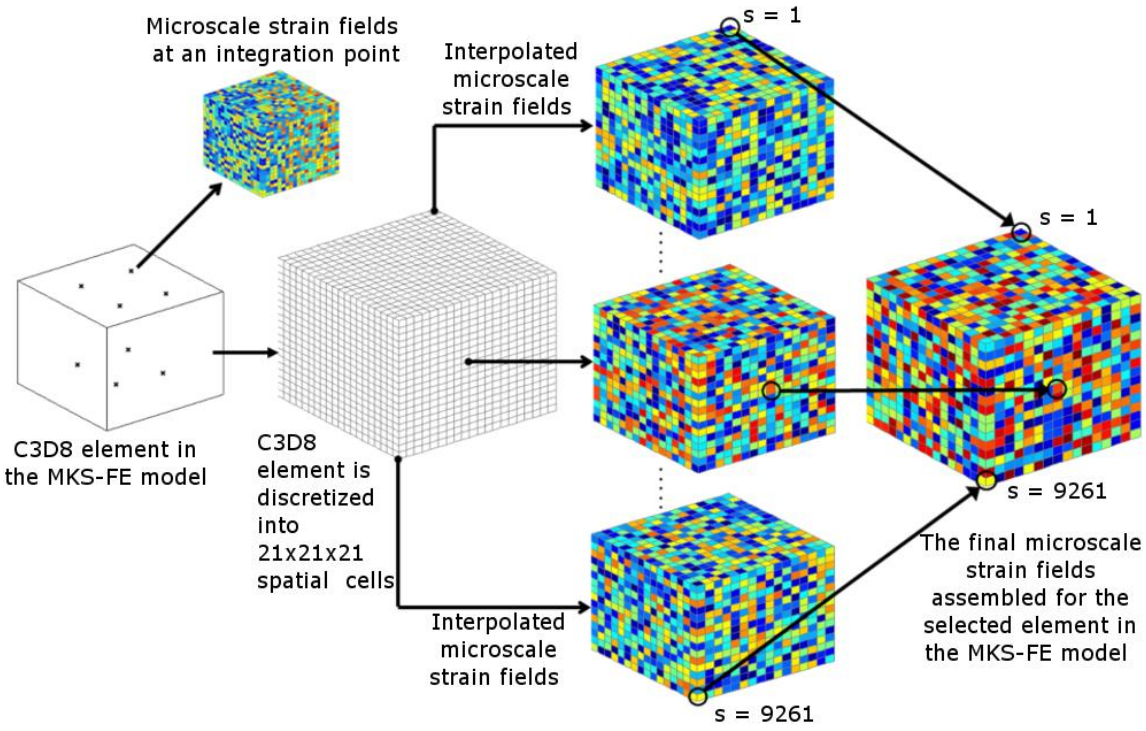

Figure A.3: Illustration of the interpolation scheme used in this work to compare the microscale spatial strain and stress fields predicted from the MKS-FE approach with the corresponding predictions from the direct FE simulation.

Figure A.4 shows a comparison of the contour plots for the microscale $(\varepsilon_s)_{11}$ component of strain for mid-planes through the random-microstructure (shown in Figure A.2 (a)) at elements A and B predicted by both the MKS-FE model (using the interpolation scheme described above) and the direct FE model. It is seen that the two predictions are in excellent agreement with each other.

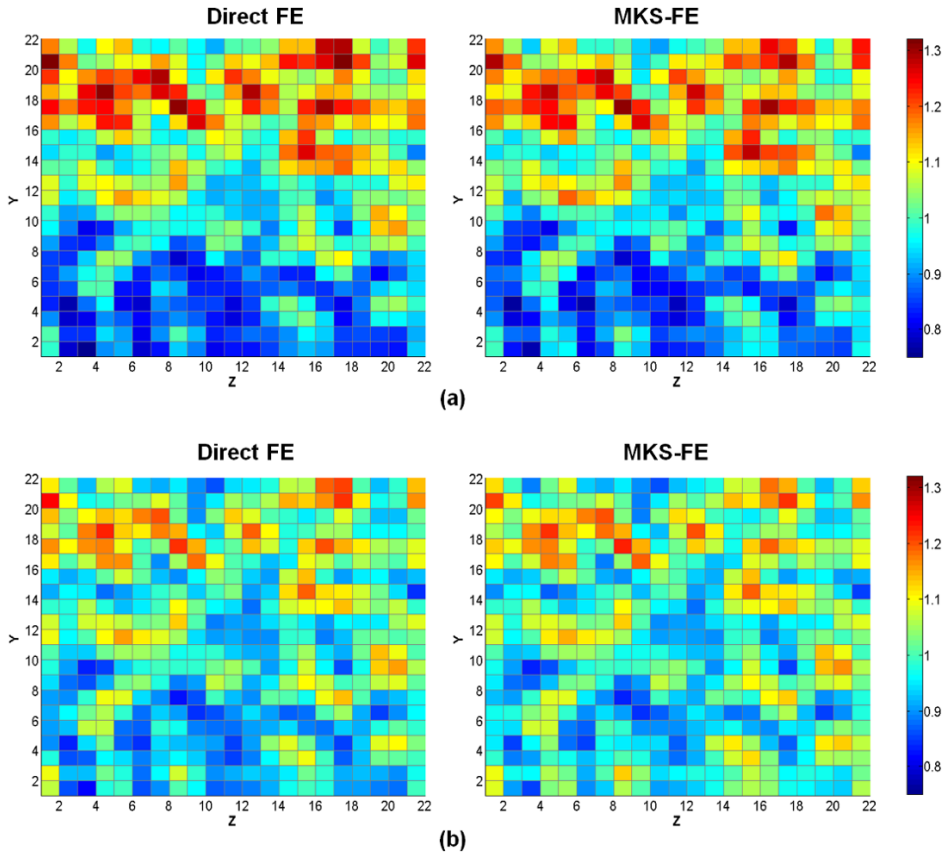

Figure A.4: Comparison of contour maps of the local $\boldsymbol{\varepsilon_{11}}$ component of strain (normalized by the macroscopic applied strain) for the mid-plane of the random microstructure (Figure A.2 (a)), calculated using the MKS-FE against the corresponding predictions from the direct FE model at (a) location A and (b) location B in the cantilever beam model shown in Figure A.1.

Figure A.5 compares the frequency distributions of the microscale σ_{11} component of stress in each phase in the random-microstructure at elements A and B in the MKS-FE model with the corresponding frequency distributions of the elements of blocks A and B in the direct FE model. In this figure, the stress distributions from the MKS-FE approach are shown using solid lines, while the stress distributions from the direct FE model are shown using dotted lines. It is seen that the predictions from the MKS-FE method

matched very well with the corresponding predictions from the direct FE model. It is also observed that the difference in the stress distributions between the two approaches is slightly higher at element A compared to element B, especially in the tails of the distributions. It should be noted that the predictions from the MKS-FE approach are obtained with very minimal computational effort. Specifically, for the case study discussed here, the direct FE simulation involving about 6 million elements required 15 hr when using 64 processors on a supercomputer (using National Center for Supercomputing Applications, NCSA, UIUC, IL), whereas the MKS-FE simulation took only 55 s on a standard desktop computer (2.6 GHz CPU and 4 GB RAM). It is therefore clear that there is tremendous gain in computational efficiency in using the MKS approach for conducting practical multi-scale FE simulations.

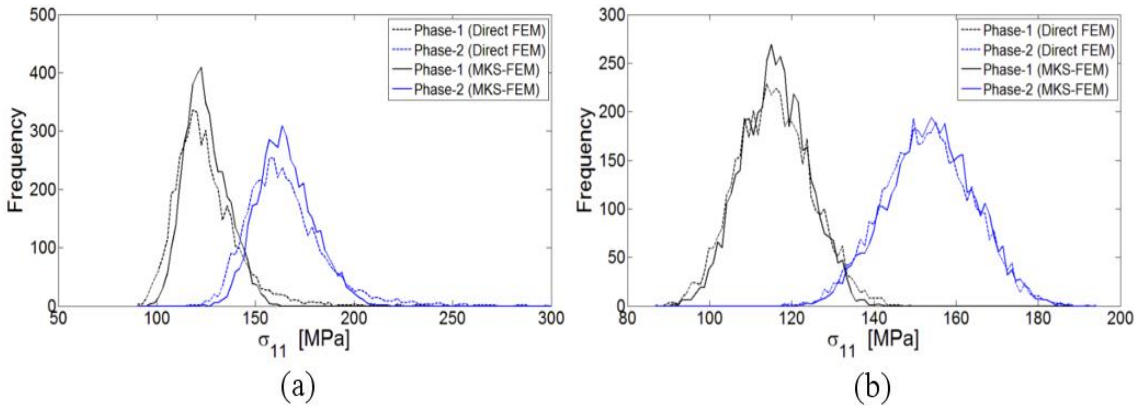

Figure A.5: Comparison of the microscale stress distributions predicted from the MKS-FE model against the corresponding predictions from the direct FE model at (a) location A and (b) location B in the cantilever beam model shown in Figure A.1. Results are for the random-microstructure shown in Figure A.2 (a).

The predictions of the MKS-FE model and the direct FE model were also compared for the rod-microstructure shown in Figure A.2 (b). Because the random and the rod microstructures are distinctly different from each other, this comparison attests to the versatility of the MKS-FE approach for a broad range of potential microstructure topologies. Note that the influence coefficients $\boldsymbol{\beta}_{\mathbf{k}}^{\mathrm{h}}$ of the MKS approach have been shown to be independent of the microstructure topology in prior studies (Fast and Kalidindi, 2011; Fast et al., 2011; Kalidindi et al., 2010; Landi and Kalidindi, 2010; Landi et al., 2009). In other words, the same set of influence coefficients were utilized for both microstructure topologies. The microscale distributions of the σ_{11} component of stress in each phase in the rod microstructure at elements A and B in both the MKS-FE and direct FE models are compared against each other in Figure A.6. Furthermore, the spatial distributions of the local $(\sigma_s)_{11}$ component of stress for a mid-plane through the rod microstructure at element B from the MKS-FE were compared with the results from the direct FE models in Figure A.7. It is seen once again that the two predictions are once again in excellent agreement with each other for the case of rod-microstructure. This result demonstrates the versatility of the MKS-FE approach in its broad applicability to a wide range of microstructure topologies.

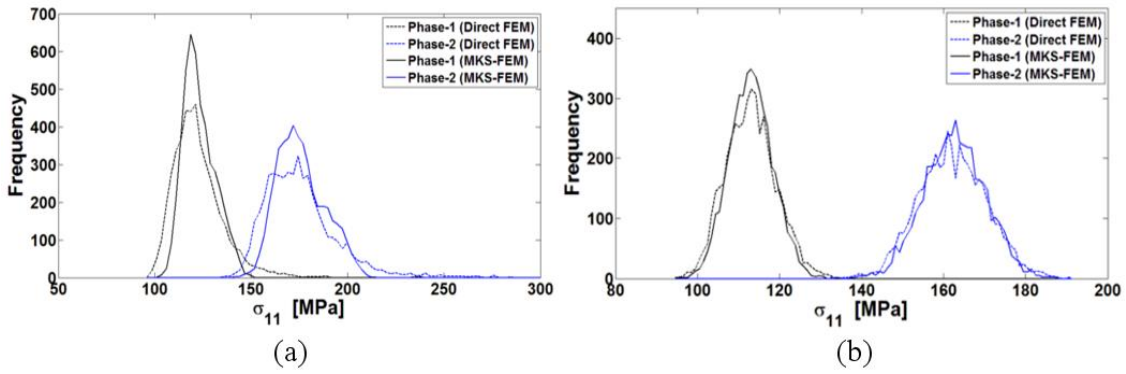

Figure A.6: Comparison of the microscale stress distributions predicted from the MKS-FE model against the corresponding predictions from the direct FE model at (a) location A and (b) location B in the cantilever beam model shown in Figure A.1. Results are for the rod-microstructure shown in Figure A.2 (b).

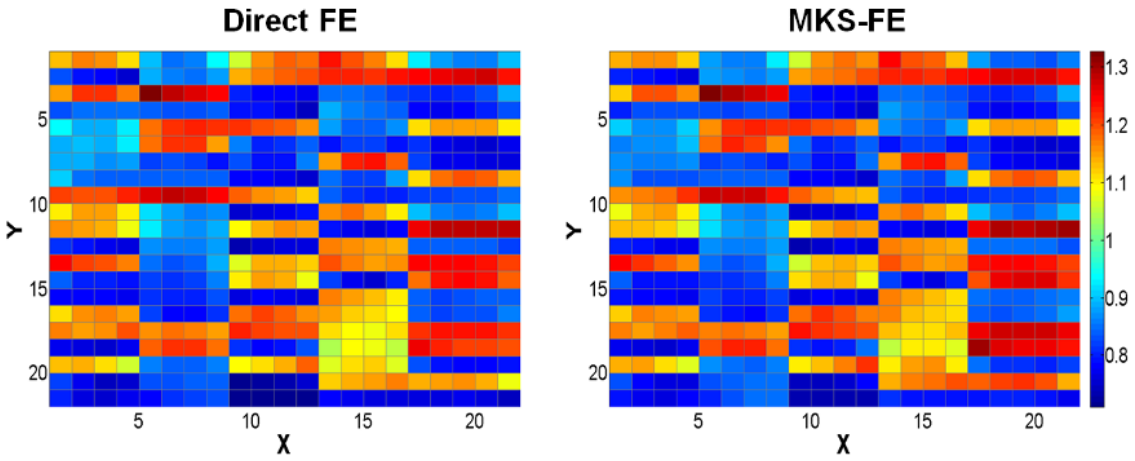

Figure A.7: Comparison of contour maps of the local σ_{11} component of stress (normalized by the macroscopic effective stress component $\langle\sigma_{11}\rangle$) for the mid-plane of a 3-D rod microstructure (Figure 2(b)), calculated using the MKS-FE against the corresponding predictions from the direct FE model at location B in the cantilever beam model shown in Figure A.1.

APPENDIX B

SPECTRAL CRYSTAL PLASTICITY UMAT

```
      MODULE CommonModule
        IMPLICIT NONE
C       ----------------------
        REAL*8,  PARAMETER  :: TOL = 0.0001
        INTEGER, PARAMETER  :: NCOEFF =6874
        INTEGER, PARAMETER  :: MFINE  = 3000000
        INTEGER, PARAMETER  :: isoflag= 1
C       --------------------
        REAL*8, PARAMETER   :: C11=168400
        REAL*8, PARAMETER   :: C12=121400
        REAL*8, PARAMETER   :: C44=75400
        REAL*8, PARAMETER   :: Yng=200000
        REAL*8, PARAMETER   :: pois=0.34
        REAL*8, PARAMETER   :: SO=16
        REAL*8, PARAMETER   :: HO=180
        REAL*8, PARAMETER   :: SS=148
        REAL*8, PARAMETER   :: AEXP=2.25
C       --------------------
        INTEGER, PARAMETER  :: NCRYSINITIAL =1
        INTEGER, PARAMETER  :: MAXCRYS = 4000
        INTEGER, PARAMETER  :: KELMFLAG = 0
        INTEGER, PARAMETER  :: NELEM = 500
        INTEGER, PARAMETER  :: NINTG = 8
        INTEGER, PARAMETER  :: LRIGID = 0
C       -------------------
        INTEGER             :: I,J,K,L,M,N
        INTEGER             :: NCRYS,INIT,JFLAG
        REAL*8, PARAMETER   :: GDO= 0.001
        REAL*8, PARAMETER   :: XM= 0.01
        REAL*8, PARAMETER   :: SPACESIZE=(120.0)**4.0
C
        COMPLEX*8,PARAMETER :: COMPLXI=(0.0D0,1.0D0)
C
        REAL*8, PARAMETER   :: PI=DACOS(-1.0D0)
        REAL*8, PARAMETER   :: DEGRAD=PI/180.0D0
        REAL*8, PARAMETER   :: RADDEG=180.0D0/PI
        REAL*8, PARAMETER   :: ZERO = 0.0D0
        REAL*8, PARAMETER   :: ONE  = 1.0D0
```

```
      REAL*8, PARAMETER   :: TWO  = 2.0D0
      REAL*8, PARAMETER   :: THREE= 3.0D0
      REAL*8, PARAMETER   :: HALF = ONE/TWO
C
      REAL*8              :: Bulk,TFLAG
C     ------------------
      COMPLEX*8, DIMENSION(NCOEFF) :: FS11,FS22,FS12,FS13,FS23,
     .                        FWS12,FWS13,FWS23,FGD
C
      INTEGER, DIMENSION(NCOEFF)   :: SUPER1,SUPER2,SUPER3,SUPER4
C
      COMPLEX*8, DIMENSION(NCOEFF) :: thetaFS11,thetaFS22,thetaFS12,
     .                        thetaFS13,thetaFS23
      COMPLEX*8, DIMENSION(NCOEFF) :: phi1FS11,phi1FS22,phi1FS12,
     .                        phi1FS13,phi1FS23
      COMPLEX*8, DIMENSION(NCOEFF) :: phiFS11,phiFS22,phiFS12,
     .                        phiFS13,phiFS23
      COMPLEX*8, DIMENSION(NCOEFF) :: phi2FS11,phi2FS22,phi2FS12,
     .                        phi2FS13,phi2FS23
      COMPLEX*8, DIMENSION(NCOEFF) :: phi1GD,phiGD,phi2GD,thetaGD
C     ----------------------
      REAL*8, DIMENSION(MAXCRYS)   :: phi1,phi,phi2
C     ----------------------
      REAL*8, DIMENSION(6,6)       :: ELASiso, ELASisoINV
      REAL*8, DIMENSION(5,5)       :: ELASiso55, ELASiso55inv
C     ----------------------
      CONTAINS
C     ----------------------
C     Load Spectral databases
      SUBROUTINE LOADDATABASE()
      IMPLICIT NONE
      INTEGER ::I,J,K,L,M,N
C
      OPEN(UNIT=101,FILE='/nv/hp22/halharbi3/scratch/CRYSP/
     .COEFF_NoSpace.inp',STATUS ='OLD')
      OPEN(UNIT=102,FILE='/nv/hp22/halharbi3/scratch/CRYSP/
     .SUPERSET_NoSpace.inp',STATUS ='OLD')
      OPEN(UNIT=103,FILE='/nv/hp22/halharbi3/scratch/CRYSP/
     .thetaderiv_NoSpace.inp',STATUS ='OLD')
      OPEN(UNIT=104,FILE='/nv/hp22/halharbi3/scratch/CRYSP/
     .phi1deriv_NoSpace.inp',STATUS ='OLD')
      OPEN(UNIT=105,FILE='/nv/hp22/halharbi3/scratch/CRYSP/
     .phideriv_NoSpace.inp',STATUS ='OLD')
      OPEN(UNIT=106,FILE='/nv/hp22/halharbi3/scratch/CRYSP/
     .phi2deriv_NoSpace.inp',STATUS ='OLD')
      OPEN(UNIT=107,FILE='/nv/hp22/halharbi3/scratch/CRYSP/
```

```
     .Gammaderiv_NoSpace.inp',STATUS ='OLD')
C
      DO J=1,NCOEFF
        READ(101,*) FS11(J),FS22(J),FS12(J),FS13(J),FS23(J),FWS12(J),
     .          FWS13(J),FWS23(J),FGD(J)
        READ(102,*) SUPER1(J),SUPER2(J),SUPER3(J),SUPER4(J)
        READ(103,*) thetaFS11(J),thetaFS22(J),thetaFS12(J),
     .          thetaFS13(J),thetaFS23(J)
        READ(104,*) phi1FS11(J),phi1FS22(J),phi1FS12(J),
     .          phi1FS13(J),phi1FS23(J)
        READ(105,*) phiFS11(J),phiFS22(J),phiFS12(J),
     .          phiFS13(J),phiFS23(J)
        READ(106,*) phi2FS11(J),phi2FS22(J),phi2FS12(J),
     .          phi2FS13(J),phi2FS23(J)
        READ(107,*)phi1GD(J),phiGD(J),phi2GD(J),thetaGD(J)
      END DO
C
      CLOSE(101)
      CLOSE(102)
      CLOSE(103)
      CLOSE(104)
      CLOSE(105)
      CLOSE(106)
      CLOSE(107)
      END SUBROUTINE
C     ----------------------------
C     Load Texture (in terms of Bunge-Euler Angles given in degree)
      SUBROUTINE LOADDATEXTURE()
      IMPLICIT NONE
      INTEGER ::I,J,K,L,M,N
C
      OPEN(UNIT=108,FILE='/nv/hp22/halharbi3/scratch/CRYSP/
     .euler_NoSpace.inp',STATUS ='OLD')
C
      DO J=1,MAXCRYS
        READ(108,*)phi1(J),phi(J),phi2(J)
      ENDDO
      CLOSE(108)
      RETURN
      END SUBROUTINE
C     --------------------------
      END MODULE CommonModule
CCCCCCCCCCCCCCCCCCCCCCCCCCCCCCCCCCCCCCCCCCCCCCCCCCCCC
CCCC
C     SPECTRAL CRYSTAL PLASTICITY UMAT FOR CUBIC MATERIALS
C     AUTHOR: HAMAD F. ALHARBI, GEORGIA TECH, ME DEPT.
```

```
C     EMAIL: ALHARBIHAMAD@GMAIL.COM
C     NOTE: NOT ALL SUBROUTINES INCLUDIED IN THIS VERSION
CCCCCCCCCCCCCCCCCCCCCCCCCCCCCCCCCCCCCCCCCCCCCCCCCCCC
CCCC
      SUBROUTINE UMAT(STRESS,STATEV,DDSDDE,SSE,SPD,SCD,
     1  RPL,DDSDDT,DRPLDE,DRPLDT,
     2  STRAN,DSTRAN,TIM,DTIME,TEMP,DTEMP,PREDEF,DPRED, CMNAME,
     3  NDI,NSHR,NTENS,NSTATV,PROPS,NPROPS,COORDS,DROT,PNEWDT,
     4  CELENT,DFGRD0,DFGRD1,NOEL,NPT,LAYER,KSPT,KSTEP,KINC)
C     ----------------------------------
      USE CommonModule
C     ---------------------------------
      IMPLICIT NONE
      CHARACTER*8 CMNAME
      INTEGER                      :: NDI, NSHR, NTENS, NSTATV, NPROPS,
     .                            NOEL, NPT, LAYER,KSPT,KSTEP,KINC
      REAL*8                      :: SSE,SPD,SCD,RPL,DTIME,TEMP,DTEMP,
     .                            PNEWDT,CELENT,DRPLDT,PREDEF
      REAL*8, DIMENSION(1)          :: REDEF,DPRED
      REAL*8, DIMENSION(2)          :: TIM,TIME
      REAL*8, DIMENSION(3)          :: COORDS
      REAL*8, DIMENSION(3,3)        :: DROTTRANS, DFGRD0,DFGRD1, DROT
      REAL*8, DIMENSION(NTENS)      ::
STRESS,DDSDDT,DRPLDE,STRAN,DSTRAN
      REAL*8, DIMENSION(NPROPS)     :: PROPS
      REAL*8, DIMENSION(NSTATV)     :: STATEV
      REAL*8, DIMENSION(NTENS,NTENS):: DDSDDE
C     --------------------------------
      CHARACTER*14                 FLAG_DECOMP
      INTEGER                     :: ICRYS, ITERFLAG,IND, INITIALGUESS,
     .                           NRmodFLAG, NRFLAG, II, NOITER_ALL,
     .                           NRFLAG_ALL,NR_FLAG
      REAL*8                     :: CHK,PT,DHYD,DDEVNORM,DtauNORM,
     .                           SLIPHARDt,SLIPHARD,PTAU
      REAL*8, DIMENSION(3)         :: WSTARS, W_TEMP
      REAL*8, DIMENSION(5)         :: SumDevStress,SIGDFT,SIGDEVT,
     .                           DSDEV1,DDEVV,ElasDevStrain_t,
     .                           ElasDevStrain_tau
      REAL*8, DIMENSION(3,3)       :: QCRSA, QCRSA_NEW, RSTART, FDOT,
     .                           FTAUINV,HLTAU,DTAU,WTAU,DDEV
      REAL*8, DIMENSION(5,5)       ::dDFTSIGdDP,ELAS55INV,XMAT55,XMATINV
      REAL*8, DIMENSION(6,6)       :: SumJAC, OLDJAC,dSIGdEt,ELAS
C     --------------------------------
      INTEGER                     :: LnewJacob
      REAL*8, DIMENSION(5,5)       :: dDstardSig,
     .                           AAjac, AAjacinv,
```

```
     .                     dDevSIGdDevD
      REAL*8, DIMENSION(5,6)      :: dDevDdEt56, dDevDdD
      REAL*8, DIMENSION(6,5)      :: dDevSIGdDevD65
      REAL*8, DIMENSION(6,6)      :: dDdEt, dpdEt, dDevSIGdEt,
     .                     dpdD, dDevSIGdD
C     ==============================
!     Read user's inputs from ABAQUS input file:
      NCRYS = PROPS(1)      ! No. of crystals per integration point
C
C     COMPUTE FDOT
      DO J = 1,3
       DO I = 1,3
         FDOT(I,J)=(DFGRD1(I,J)-DFGRD0(I,J))/DTIME
       ENDDO
      ENDDO
C
C     COMPUTE FTAU INVERSE
      CALL MAT3INV(DFGRD1,FTAUINV)
C
C     COMPUTE L
      CALL MULTIP(FDOT,FTAUINV,HLTAU)
C
C     COMPUTE D
      DTAU(1,1)=HLTAU(1,1)
      DTAU(2,2)=HLTAU(2,2)
      DTAU(3,3)=HLTAU(3,3)
      DTAU(1,2)=HALF*(HLTAU(1,2)+HLTAU(2,1))
      DTAU(1,3)=HALF*(HLTAU(1,3)+HLTAU(3,1))
      DTAU(2,3)=HALF*(HLTAU(2,3)+HLTAU(3,2))
      DTAU(2,1)=DTAU(1,2)
      DTAU(3,1)=DTAU(1,3)
      DTAU(3,2)=DTAU(2,3)
C
C     COMPUTE NORM OF D
      DtauNORM=DSQRT(DTAU(1,1)*DTAU(1,1) + 2.0*DTAU(1,2)*DTAU(1,2)+
     .          2.0*DTAU(1,3)*DTAU(1,3) + DTAU(2,2)*DTAU(2,2)+
     .          2.0*DTAU(2,3)*DTAU(2,3) + DTAU(3,3)*DTAU(3,3))
C
C     COMPUTE W
      WTAU(1,1)=ZERO
      WTAU(2,2)=ZERO
      WTAU(3,3)=ZERO
      WTAU(1,2)=HALF*(HLTAU(1,2)-HLTAU(2,1))
      WTAU(1,3)=HALF*(HLTAU(1,3)-HLTAU(3,1))
      WTAU(2,3)=HALF*(HLTAU(2,3)-HLTAU(3,2))
      WTAU(2,1)=-WTAU(1,2)
```

```
      WTAU(3,1)=-WTAU(1,3)
      WTAU(3,2)=-WTAU(2,3)
C
C     COMPUTE DEVATORIC PART OF DTAU (TRACELESS D)
      DHYD=(DTAU(1,1)+DTAU(2,2)+DTAU(3,3))/THREE
      DDEV(1,1)=DTAU(1,1)-DHYD
      DDEV(2,2)=DTAU(2,2)-DHYD
      DDEV(3,3)=DTAU(3,3)-DHYD
      DDEV(1,2)=DTAU(1,2)
      DDEV(1,3)=DTAU(1,3)
      DDEV(2,3)=DTAU(2,3)
      DDEV(2,1)=DDEV(1,2)
      DDEV(3,1)=DDEV(1,3)
      DDEV(3,2)=DDEV(2,3)
C
C     COMPUTE NORM OF D'
      DDEVNORM=DSQRT(2*(DDEV(1,1)*DDEV(1,1)+DDEV(2,2)*DDEV(2,2)+
     .               DDEV(1,1)*DDEV(2,2)+DDEV(1,2)*DDEV(1,2)+
     .               DDEV(1,3)*DDEV(1,3)+DDEV(2,3)*DDEV(2,3)))
C
C     Calculate pressure and stress at time t
      PT=(STRESS(1)+STRESS(2)+STRESS(3))/THREE   ! Pressure at time t
      SIGDEVT(1)=STRESS(1)-PT                    ! Devatoric stress at time t, 11
      SIGDEVT(2)=STRESS(2)-PT                    ! Devatoric stress at time t, 22
      SIGDEVT(3)=STRESS(4)                     ! Devatoric stress at time t, 12
      SIGDEVT(4)=STRESS(5)                     ! Devatoric stress at time t, 13
      SIGDEVT(5)=STRESS(6)                     ! Devatoric stress at time t, 23
C
C     COMPUTE THE PRESSURE AT TIME TAU
      PTAU=Bulk*DHYD*THREE*DTIME+PT
C
C     RETRIEVE THE PREVIOUS DEVIATORIC ELASTIC STRAIN
      ind=(1+9)*NCRYS+36+1
      ElasDevStrain_t(1)=STATEV(ind)
      ElasDevStrain_t(2)=STATEV(ind+1)
      ElasDevStrain_t(3)=STATEV(ind+2)
      ElasDevStrain_t(4)=STATEV(ind+3)
      ElasDevStrain_t(5)=STATEV(ind+4)
C
C
C     Start Loop over all crystals for each integration point
      DO J=1,5
        SumDevStress(J)=ZERO     !Initialize the sum of devatoric stress
      ENDDO
      DO J = 1,6
        DO K = 1,6
```

```
          SumJAC(K,J) = ZERO   !Initialize the sum of Jacobian
        ENDDO
      ENDDO
C     ---------------------------------
      ind=1
      CrystalLoop: DO II=1,NCRYS
          SLIPHARDt=STATEV(ind)
          QCRSA(1,1)=STATEV(ind+1)
          QCRSA(1,2)=STATEV(ind+2)
          QCRSA(1,3)=STATEV(ind+3)
          QCRSA(2,1)=STATEV(ind+4)
          QCRSA(2,2)=STATEV(ind+5)
          QCRSA(2,3)=STATEV(ind+6)
          QCRSA(3,1)=STATEV(ind+7)
          QCRSA(3,2)=STATEV(ind+8)
          QCRSA(3,3)=STATEV(ind+9)
C         ========================
C         DECOMPOSE D' INTO ELASTIC (D*') AND PLASTIC (Dp') PARTS
C
C         Modified Newton-Raphson
          NR_FLAG=0
          CALL DECOMPDNR(SLIPHARDt,DTIME,DDEV,WTAU,SIGDEVT,
     .                   QCRSA,DDEVNORM,ElasDevStrain_t,
     .                   SIGDFT, RSTART, SLIPHARD,NOITER_ALL,
     .                   ElasDevStrain_tau,ELAS55INV,XMAT55,
     .                   dDFTSIGdDP,NR_FLAG)
          FLAG_DECOMP='DECOMPDNR'
          NRFLAG_ALL=NR_FLAG
          IF (NR_FLAG .EQ. 1) GO TO 300
C         ---------------------------------
          WRITE(*,*)'*****************************************'
          WRITE(*,*) 'ERROR, MANY ITERATIONS FOR DECOMPOSING D'
          WRITE(*,*) 'CHECK ERROR FILE '
          WRITE(*,*)'*****************************************'
          CALL XIT
C
300       CONTINUE
C         UPDATE JACOBIAN IF REQUIRED
C         -----------------------------------
          IF (isoflag .EQ. 1) THEN
           DO 5 I=1,5
             DO 5 J=1,5
             dDstardSig(I,J) = ZERO
             DO 5 K=1,5
5               dDstardSig(I,J)=dDstardSig(I,J)+
     .                     ELASiso55inv(I,K)*XMAT55(K,J)
```

```
      ELSE  !for anisotropic
        DO 10 I=1,5
        DO 10 J=1,5
         dDstardSig(I,J) = ZERO
         DO 10 K=1,5
10         dDstardSig(I,J)=dDstardSig(I,J)+
     .                ELAS55INV(I,K)*XMAT55(K,J)
      ENDIF
C
      CALL dDdEtboth(DTIME, DFGRD0, DFGRD1,
     .           dDdEt,dDevDdEt56)
C      ---------------------------------
      DO 15 J=1,6
15      dpdEt(1,J)=Bulk*DTIME*(dDdEt(1,J)+dDdEt(2,J)+dDdEt(3,J))
      DO 20 J=2,3
        DO 20 K=1,6
20        dpdEt(J,K) = dpdEt(1,K)
      DO 25 J=4,6
        DO 25 K=1,6
25        dpdEt(J,K) = ZERO
C
C
      DO 35 I=1,5
        DO 35 J=1,5
        AAjac(I,J) = ZERO
        DO 35 K=1,5
35        AAjac(I,J)=AAjac(I,J)+dDFTSIGdDP(I,K)*dDstardSig(K,J)
      AAjac(1,1)=AAjac(1,1)+ONE
      AAjac(2,2)=AAjac(2,2)+ONE
      AAjac(3,3)=AAjac(3,3)+ONE
      AAjac(4,4)=AAjac(4,4)+ONE
      AAjac(5,5)=AAjac(5,5)+ONE
      CALL MATINV55(AAjac,AAjacinv)
C
C
      DO 40 I=1,5
        DO 40 J=1,5
          dDevSIGdDevD(I,J)=ZERO
          DO 40 K=1,5
40          dDevSIGdDevD(I,J)=dDevSIGdDevD(I,J)+
     .                AAjacinv(I,K)*dDFTSIGdDP(K,J)
C
C
      DO 45 J=1,5
        dDevSIGdDevD65(1,J)=dDevSIGdDevD(1,J)
        dDevSIGdDevD65(2,J)=dDevSIGdDevD(2,J)
```

```
          dDevSIGdDevD65(3,J)=-dDevSIGdDevD(1,J)-dDevSIGdDevD(2,J)
          dDevSIGdDevD65(4,J)=dDevSIGdDevD(3,J)
          dDevSIGdDevD65(5,J)=dDevSIGdDevD(4,J)
45          dDevSIGdDevD65(6,J)=dDevSIGdDevD(5,J)
C
        DO 60 I=1,6
         DO 60 J=1,6
          dDevSIGdEt(I,J) = ZERO
          DO 50 K=1,5
50            dDevSIGdEt(I,J)=dDevSIGdEt(I,J)+
     .                  dDevSIGdDevD65(I,K)*dDevDdEt56(K,J)
          dSIGdEt(I,J) = dDevSIGdEt(I,J)+dpdEt(I,J)
60       CONTINUE
C
C        COMPUTE SUM OF DEVATORIC STRESS AND JACOBIAN
        DO J = 1,5
           SumDevStress(J)=SumDevStress(J)+SIGDFT(J)
        ENDDO
        DO J = 1,6
          DO K = 1,6
           SumJAC(K,J) = SumJAC(K,J)+dSIGdEt(K,J)
          ENDDO
        ENDDO
C    ------------------------------
C        UPDATE STATE VARIABLES: SLIPHARDt & QCRSA
        STATEV(ind)=SLIPHARD
        CALL MULTIPT(RSTART,QCRSA,QCRSA_NEW)
        STATEV(ind+1)=QCRSA_NEW(1,1)
        STATEV(ind+2)=QCRSA_NEW(1,2)
        STATEV(ind+3)=QCRSA_NEW(1,3)
        STATEV(ind+4)=QCRSA_NEW(2,1)
        STATEV(ind+5)=QCRSA_NEW(2,2)
        STATEV(ind+6)=QCRSA_NEW(2,3)
        STATEV(ind+7)=QCRSA_NEW(3,1)
        STATEV(ind+8)=QCRSA_NEW(3,2)
        STATEV(ind+9)=QCRSA_NEW(3,3)
!    ----------------------------------
222       CONTINUE
        ind=ind+10
    ENDDO CrystalLoop
C
450  CONTINUE
C
C    COMPUTE AND PASS THE FINAL STRESS AND JACOBIAN TO ABAQUS
    STRESS(1)=SumDevStress(1)/NCRYS+PTAU
    STRESS(2)=SumDevStress(2)/NCRYS+PTAU
```

```
      STRESS(3)=-STRESS(1)-STRESS(2)+THREE*PTAU
      STRESS(4)=SumDevStress(3)/NCRYS
      STRESS(5)=SumDevStress(4)/NCRYS
      STRESS(6)=SumDevStress(5)/NCRYS
      DO J = 1,6
        DO K = 1,6
          OLDJAC(K,J) = SumJAC(K,J)/NCRYS
        ENDDO
      ENDDO
C
600   CONTINUE
C
      ind=(1+9)*NCRYS+1
      DO I = 1,6
         DO J = 1,6
           DDSDDE(J,I) = OLDJAC(J,I)
C
           STATEV(ind)  = OLDJAC(J,I)
           ind=ind+1
         ENDDO
      ENDDO
C
      ind=(1+9)*NCRYS+36+1
      STATEV(ind)  =ElasDevStrain_tau(1)
      STATEV(ind+1)=ElasDevStrain_tau(2)
      STATEV(ind+2)=ElasDevStrain_tau(3)
      STATEV(ind+3)=ElasDevStrain_tau(4)
      STATEV(ind+4)=ElasDevStrain_tau(5)
C
      RETURN   ! END OF UMAT SUBROUTINE
      END
CCCCCCCCCCCCCCCCCCCCCCCCCCCCCCCCCCCCCCCCCCCC
      SUBROUTINE DECOMPDNR(SLIPHARDt,DTIME,DEVD,WAPP,SIGDEVT,
     .           QCRSA,DDEVNORM,ElasDevStrain_t,
     .           DFTSIG, RSTART, SLIPHARD,NOITER,ElasDevStrain_tau,
     .           ELAS55INV,XMAT55,dDFTSIGdDP,NR_FLAG)
C     ----------------------------
      USE CommonModule
C     ----------------------------
      IMPLICIT NONE
      INTEGER               :: NR_FLAG, NOITER,LFLAG1
      REAL*8                :: SLIPHARD, SLIPHARDt,eps_incr,
     .                     check, DDEVNORM,DTIME,eps,lambda,
     .                     VM_DFTSIG,eps_Max,eta,eps_incr_Max,
     .                     alpha,DSDEV_NORM,VM_HPRSIG,Beta,gamm
      REAL*8, DIMENSION(3)      :: WSTARS
```

```
      REAL*8, DIMENSION(5)     :: DFTSIG, SIGDFT1, SIGDEVT, SIGJM,
     .                    DSDEV, DSDEV1,Gfun,HPRSIG,
     .                    delDstar,gradf,ElasDevStrain_t,
     .                    ElasDevStrain_tau,ElasDevStrain_incr
     .
      REAL*8, DIMENSION(3,3)    :: DP, DP1,QCRSA,DEVD,
     .                    WAPP, RSTART, QCRDEF
      REAL*8, DIMENSION(5,5)    :: ELAS55, ELAS55INV, XMAT55,XMATINV,
     .                    dDFTSIGdDP,dSIGdDstar,DSJACOB,
     .                    DSJACOBINV
      REAL*8, DIMENSION(6,6)    :: ELAS
C
C     INITIAL GUESS: D'*
C
      LFLAG1=0
      CALL FFT_STRESS_JAC(LFLAG1,DTIME,DEVD,WAPP,SLIPHARDt,QCRSA,
     .                DFTSIG,SLIPHARD,WSTARS,dDFTSIGdDP)
C
      VM_DFTSIG=DSQRT(3*(DFTSIG(1)**2+DFTSIG(2)**2+DFTSIG(1)*DFTSIG(2)
     .          + DFTSIG(3)**2+DFTSIG(4)**2+DFTSIG(5)**2))
      eps_Max=VM_DFTSIG/Yng
      eta=0.1
      eps_incr_Max=eta*eps_Max
C
C
      SIGJM(1)=-2*DFTSIG(3)*WSTARS(1)/DTIME-2*DFTSIG(4)*
     .        WSTARS(2)/DTIME+
     .        (DFTSIG(1) - SIGDEVT(1))/DTIME
C
      SIGJM(2)=-2*DFTSIG(5)*WSTARS(3)/DTIME+2*DFTSIG(3)*
     .       WSTARS(1)/DTIME+
     .       (DFTSIG(2) - SIGDEVT(2))/DTIME
C
      SIGJM(3)=-DFTSIG(2)*WSTARS(1)/DTIME + DFTSIG(1)*
     .        WSTARS(1)/DTIME - DFTSIG(4)*WSTARS(3)/DTIME-
     .        DFTSIG(5)*WSTARS(2)/DTIME+(DFTSIG(3) -
     .        SIGDEVT(3))/DTIME
C
      SIGJM(4)=-DFTSIG(5)*WSTARS(1)/DTIME + DFTSIG(3)*
     .        WSTARS(3)/DTIME + DFTSIG(2)*WSTARS(2)/DTIME+
     .        2*DFTSIG(1)*WSTARS(2)/DTIME+(DFTSIG(4)-
     .        SIGDEVT(4))/DTIME
C
      SIGJM(5)=(DFTSIG(5) - SIGDEVT(5))/DTIME +
     .       DFTSIG(4)*WSTARS(1)/DTIME +DFTSIG(1)*WSTARS(3)/DTIME+
     .       2*DFTSIG(2)*WSTARS(3)/DTIME + DFTSIG(3)*
```

```
     .       WSTARS(2)/DTIME
C
C
      IF (isoflag .EQ. 1) THEN
        DO 49 J=1,5
          DSDEV(J)=0.0
          DO 49 K=1,5
49          DSDEV(J)=DSDEV(J)+ELASiso55inv(J,K)*SIGJM(K)
      ELSE
        CALL ROTMAT(-WSTARS(1),-WSTARS(2),-WSTARS(3),RSTART)
        CALL MULTIPT(RSTART,QCRSA,QCRDEF)
        CALL ELAST(QCRDEF,ELAS)
        CALL ELAST55(ELAS,ELAS55)
        CALL MATINV55(ELAS55,ELAS55INV)
        DO 50 J=1,5
          DSDEV(J)=0.0
          DO 50 K=1,5
50          DSDEV(J)=DSDEV(J)+ELAS55INV(J,K)*SIGJM(K)
      ENDIF
C
      DSDEV_NORM=DSQRT(2.0*(DSDEV(1)**2+DSDEV(2)**2+DSDEV(1)*
     .       DSDEV(2)+DSDEV(3)**2+DSDEV(4)**2+DSDEV(5)**2))
C
      alpha=0.1
      IF (DSDEV_NORM .LT. alpha*DDEVNORM) GO TO 570
C
      WSTARS(1)= WAPP(1,2)*DTIME
      WSTARS(2)= WAPP(1,3)*DTIME
      WSTARS(3)= WAPP(2,3)*DTIME
      CALL ElastEqn(DTIME,DEVD,WSTARS,QCRSA,SIGDEVT,
     .            RSTART,HPRSIG,XMATINV)
C

VM_HPRSIG=DSQRT(3*(HPRSIG(1)**2+HPRSIG(2)**2+HPRSIG(1)*HPRSIG(2)
     .          + HPRSIG(3)**2+HPRSIG(4)**2+HPRSIG(5)**2))
C     ---------------------------------------
      IF (VM_DFTSIG .GT. VM_HPRSIG) THEN
        DSDEV(1)=DEVD(1,1)
        DSDEV(2)=DEVD(2,2)
        DSDEV(3)=DEVD(1,2)
        DSDEV(4)=DEVD(1,3)
        DSDEV(5)=DEVD(2,3)
      ELSE
        Beta=VM_DFTSIG/VM_HPRSIG
        DSDEV(1)=Beta*DEVD(1,1)
        DSDEV(2)=Beta*DEVD(2,2)
```

```
        DSDEV(3)=Beta*DEVD(1,2)
        DSDEV(4)=Beta*DEVD(1,3)
        DSDEV(5)=Beta*DEVD(2,3)
      ENDIF
C     ---------------------------------
      DO I=1,5
        ElasDevStrain_tau(I)=ElasDevStrain_t(I)+DSDEV(I)*dtime
      ENDDO
      eps=DSQRT(2.0*(ElasDevStrain_tau(1)**2+ElasDevStrain_tau(2)**2+
     .ElasDevStrain_tau(1)*ElasDevStrain_tau(2)+ElasDevStrain_tau(3)**2+
     .ElasDevStrain_tau(4)**2+ElasDevStrain_tau(5)**2))
C
      IF (eps .GT. eps_Max) THEN
        gamm=eps_Max/eps
        DO I=1,5
          DSDEV(I)=gamm*DSDEV(I)
        ENDDO
      ENDIF
C
570   CONTINUE
C
C     Start NR method
      NR_FLAG=1
      NOITER=1
400   CONTINUE
C
      DSDEV1(1)=DSDEV(1)
      DSDEV1(2)=DSDEV(2)
      DSDEV1(3)=DSDEV(3)
      DSDEV1(4)=DSDEV(4)
      DSDEV1(5)=DSDEV(5)
C     CALCULATE DP
      DP(1,1)=DEVD(1,1)-DSDEV(1)
      DP(2,2)=DEVD(2,2)-DSDEV(2)
      DP(3,3)=-DP(1,1)-DP(2,2)
      DP(1,2)=DEVD(1,2)-DSDEV(3)
      DP(1,3)=DEVD(1,3)-DSDEV(4)
      DP(2,3)=DEVD(2,3)-DSDEV(5)
      DP(2,1)=DP(1,2)
      DP(3,1)=DP(1,3)
      DP(3,2)=DP(2,3)
C
C     1] Calculate the function G
      LFLAG1=1
      CALL FFT_STRESS_JAC(LFLAG1,DTIME,DP,WAPP,SLIPHARDt,QCRSA,
     .                    DFTSIG,SLIPHARD,WSTARS,dDFTSIGdDP)
```

```
C
      CALL ElastEqn(DTIME,DSDEV,WSTARS,QCRSA,SIGDEVT,
     .            RSTART,HPRSIG,XMATINV)
C
      Do 30 K=1,5
30     Gfun(K)=DFTSIG(K)-HPRSIG(K)
C
C     2] CALCULATE THE JACOBIAN: J=d(GFUN)/d(D*')
C
C     2.1] d(DFTSIG)/d(Dp)
C         ALREADY CALCULATED ABOVE IN SUBROUTINE FFT_STRESS_JAC
C     2.2] d(HPRSIG)/d(D*')
      DO 40 I=1,5
       DO 40 J=1,5
        dSIGdDstar(I,J) = ZERO
        DO 40 K=1,5
         IF (isoflag .eq. 1) then
          dSIGdDstar(I,J)=dSIGdDstar(I,J)+XMATINV(I,K)*ELASiso55(K,J)
         ELSE
          dSIGdDstar(I,J)=dSIGdDstar(I,J)+XMATINV(I,K)*ELAS55(K,J)
         ENDIF
40     CONTINUE
      DO 70, J=1,5
       DO 70, K=1,5
70       DSJACOB(J,K)=-dDFTSIGdDP(J,K)-dSIGdDstar(J,K)
C
C     3] MODIFY D*':  [D*'](n+1)=[D*'](n)-inv[DSJACOB]*G
C
      CALL MATINV55(DSJACOB,DSJACOBINV)
C
      DO J=1,5
        delDstar(J)=ZERO
        DO K=1,5
          delDstar(J)=delDstar(J)-DSJACOBINV(J,K)*Gfun(K)
        ENDDO
        DSDEV(J)=DSDEV1(J)+delDstar(J)
      ENDDO
C
C
      DO I=1,5
        ElasDevStrain_incr(I)=DSDEV(I)*dtime
        ElasDevStrain_tau(I)=ElasDevStrain_t(I)+ElasDevStrain_incr(I)
      ENDDO
      eps_incr=DSQRT(2.0*(ElasDevStrain_incr(1)**2+
     .        ElasDevStrain_incr(2)**2+ElasDevStrain_incr(1)*
     .        ElasDevStrain_incr(2)+ElasDevStrain_incr(3)**2+
```

```
     .       ElasDevStrain_incr(4)**2+ElasDevStrain_incr(5)**2))
C
      IF (eps_incr .GE. eps_incr_Max) THEN
        lambda=eps_incr_Max/eps_incr
        DO J=1,5
          DSDEV(J)=DSDEV1(J)+lambda*delDstar(J)
        ENDDO
      ENDIF
C
C     CONVERGENCE CRITERION BASED ON D*'
      check=DMAX1(    DABS(DSDEV(1)-DSDEV1(1)),
     &                DABS(DSDEV(2)-DSDEV1(2)),
     &                DABS(DSDEV(3)-DSDEV1(3)),
     &                DABS(DSDEV(4)-DSDEV1(4)),
     &                DABS(DSDEV(5)-DSDEV1(5)))/DDEVNORM
C
      IF (check .LE. TOL) THEN
          IF (isoflag .EQ. 1) THEN
            CALL ROTMAT(-WSTARS(1),-WSTARS(2),-WSTARS(3),RSTART)
          ENDIF
          GO TO 500
      ENDIF
C
      IF (NOITER .GT. 50) THEN
          NR_FLAG=0
          RETURN
      ENDIF
C
      NOITER=NOITER+1
      GO TO 400
500   CONTINUE
C
      NR_FLAG=1
      RETURN
      END
CCCCCCCCCCCCCCCCCCCCCCCCCCCCCC
      SUBROUTINE
FFT_STRESS_JAC(LFLAG1,DTIME,DP,WAPP,SLIPHARDt,QCRSA,
     .                    DFTSIG,SLIPHARD,WSTARS,dDFTSIGdDP)
      USE CommonModule
      IMPLICIT NONE
      INTEGER                 :: LFLAG1, indTHETA,
     .                        indphi1, indphi, indphi2
      REAL*8                  :: DPNORM,THETA,ABSSTRRATE,SLIPHARDt,
     .                        SP11,SP22,SP12,SP13,SP23,SLIPHARD,
     .                        WPPRIN12,WPPRIN13,WPPRIN23,
```

```
     .                    TEMP1, TEM1, TEM2, TEM3, TEM4,
     .                    TEM5, phi1D, phiD, phi2D,CONST,
     .                    ZA,ZB,ZC,ZD,ZE,ZF,ZG,ZH,ZI,
     .                    Z0,Z1,Z2,Z3,Z4,Z5,Z6,Z7,Z8,Z9,Z10,
     .                    Z11,Z12,Z13,Z14,Z15,Z16,Z17,Z18,
     .                    Z19,Z20,Z21,Z22,Z23,Z24,Z25,Z26,
     .                    Z27,Z28,Z29,Z30,Z31,Z32,Z33,Z34,
     .                    C1,C2,C3,S1,S2,S3,C1C1,C2C2,C3C3,
     .                    S1S1,S2S2,S3S3,C1C3,C2C3,C2C1,
     .                    S2S1,S1S3,S2S3,TOTGAMMA,SS1,SS3,
     .                    SS5,SS6,SS7,SS9,SS10,SS11,DTIME,
     .                    phi1p,phip,phi2p
      REAL*8, DIMENSION(3)       :: EIGDP, TEMP3, dgDdD11, dgDdD22,
     .                    dgDdD12, dgDdD13, dgDdD23,WPSA,
     .                    WSTARS
      REAL*8, DIMENSION(5)       :: AA1, DFTSIG, AA2, CC3, dSIGTHETA,
     .                    CC1, CC2, DD1, DD2, DD3, DD6,
     .                    DD7, DD8, DD5, EE1, FF1,SSFINAL,
     .                    ZZ
      REAL*8, DIMENSION(6)       :: DD4
      REAL*8, DIMENSION(3,3)      :: DP,WAPP,EIGVDP,QCRSA,QCRPR,TEMP33
      REAL*8, DIMENSION(5,5)      :: AAFINAL, CCFINAL,DDFINAL,ZZFINAL,
     .                    EEFINAL, FFFINAL, dDFTSIGdDP
      COMPLEX*8, DIMENSION(NCOEFF) :: SUPERMAT
C
      TEMP33(1,1)=DP(1,1)
      TEMP33(2,1)=DP(2,1)
      TEMP33(3,1)=DP(3,1)
      TEMP33(1,2)=DP(1,2)
      TEMP33(2,2)=DP(2,2)
      TEMP33(3,2)=DP(3,2)
      TEMP33(1,3)=DP(1,3)
      TEMP33(2,3)=DP(2,3)
      TEMP33(3,3)=DP(3,3)
      CALL JACOBI(TEMP33,EIGDP,EIGVDP)
      CALL EIGSORT(EIGDP,EIGVDP)
      CALL COLNORM(EIGVDP)
      DPNORM=DSQRT(EIGDP(1)**2+EIGDP(2)**2+EIGDP(3)**2)
C
      THETA=DATAN2((-TWO*EIGDP(1)-EIGDP(3))/DPNORM,
     .     DSQRT(THREE)*EIGDP(3)/DPNORM)
       IF (THETA .LT. ZERO) THETA=THETA+PI
C
      CALL MULTIPT(EIGVDP,QCRSA,QCRPR)
C
      CALL MATEUL1(QCRPR,phi1p,phip,phi2p)
```

```
C
      indphi1=IDNINT(phi1p*RADDEG*MFINE/THREE)
      indphi=IDNINT(phip*RADDEG*MFINE/THREE)
      indphi2=IDNINT(phi2p*RADDEG*MFINE/THREE)
      indTHETA=IDNINT(THETA*RADDEG*MFINE/THREE)
C
C     USE THE SPECTRAL APPROACH TO COMPUTE STRESS, WSTAR, TOTAL
SHEAR RATE
      ABSSTRRATE=DABS(DPNORM/GDO)
      SUPERMAT=TWO*CDEXP(TWO*PI*COMPLXI/(120*MFINE)*
     . ((SUPER1-ONE)*indphi2+
     . (SUPER2-ONE)*indphi+
     . (SUPER3-ONE)*indphi1+
     . (SUPER4-ONE)*indTHETA))

C     COMPUTE THE TOTAL SHEAR RATE
      TOTGAMMA=ABSSTRRATE*sum(FGD*SUPERMAT)/SPACESIZE
C
C     COMPUTE THE SLIP HARDENING
      SLIPHARD=SLIPHARDt+HO*(1-
(SLIPHARDt/SS))**AEXP*TOTGAMMA*DTIME
C
C     COMPUTE THE STRESS IN THE PRINCIPAL FRAME
      SP11=DSIGN(ONE,ABSSTRRATE)*SLIPHARD/100.0D0*ABSSTRRATE**XM*
     .        sum(FS11*SUPERMAT)/SPACESIZE
      SP22=DSIGN(ONE,ABSSTRRATE)*SLIPHARD/100.0D0*ABSSTRRATE**XM*
     .        sum(FS22*SUPERMAT)/SPACESIZE
      SP12=DSIGN(ONE,ABSSTRRATE)*SLIPHARD/100.0D0*ABSSTRRATE**XM*
     .        sum(FS12*SUPERMAT)/SPACESIZE
      SP13=DSIGN(ONE,ABSSTRRATE)*SLIPHARD/100.0D0*ABSSTRRATE**XM*
     .        sum(FS13*SUPERMAT)/SPACESIZE
      SP23=DSIGN(ONE,ABSSTRRATE)*SLIPHARD/100.0D0*ABSSTRRATE**XM*
     .        sum(FS23*SUPERMAT)/SPACESIZE
C
C     TRANSFER THE STRESS INTO THE SAMPLE FRAME
      CALL RANK2TRANS(EIGVDP,SP11,SP22,SP12,SP13,SP23,DFTSIG)
C     ------------------------------------------------------------------------
C     CALCULATE WSTAR IN THE SAMPLE FRAME
C     STEP-A] USE SPECTRAL APPROACH TO CALCULATE WP IN THE
PRINCIPLE FRAME
      WPPRIN12=(DPNORM/GDO)*sum(FWS12*SUPERMAT)/SPACESIZE
      WPPRIN13=(DPNORM/GDO)*sum(FWS13*SUPERMAT)/SPACESIZE
      WPPRIN23=(DPNORM/GDO)*sum(FWS23*SUPERMAT)/SPACESIZE
C
C     STEP-B] TRANSFORM WP FROM THE PRINCIPLE FRAME TO THE SAMPLE
FRAME
```

```
      CALL MULTIPWS(EIGVDP,WPPRIN12,WPPRIN13,WPPRIN23,WPSA)
C
C     STEP-C] GET WSTAR IN THE SAMPLE FRAME
      WSTARS(1)= (WAPP(1,2)-WPSA(1))*DTIME       !W*(1,2)
      WSTARS(2)= (WAPP(1,3)-WPSA(2))*DTIME       !W*(1,3)
      WSTARS(3)= (WAPP(2,3)-WPSA(3))*DTIME       !W*(2,3)
C
C     CALCULATE: d(DFTSIG)/d(Dp)
      IF (LFLAG1 .EQ. 1) THEN
C
C     [d(SIGMA)/d(NORMDP)]
      AA1(1)=XM/DPNORM*DFTSIG(1)
      AA1(2)=XM/DPNORM*DFTSIG(2)
      AA1(3)=XM/DPNORM*DFTSIG(3)
      AA1(4)=XM/DPNORM*DFTSIG(4)
      AA1(5)=XM/DPNORM*DFTSIG(5)
C
C     [d(NORMDP)/d(DP)]
      AA2(1)=(TWO*DP(1,1)+DP(2,2))/DPNORM
      AA2(2)=(TWO*DP(2,2)+DP(1,1))/DPNORM
      AA2(3)=TWO*DP(1,2)/DPNORM
      AA2(4)=TWO*DP(1,3)/DPNORM
      AA2(5)=TWO*DP(2,3)/DPNORM
C
      DO 10 J=1,5
      DO 10 K=1,5
10    AAFINAL(J,K)= AA1(J)*AA2(K)
C
C     [d(SIGMA)/d(THETA)]

CC3(1)=DSIGN(ONE,ABSSTRRATE)*SLIPHARD/100.0D0*ABSSTRRATE**XM*
     .        sum(thetaFS11*SUPERMAT)/SPACESIZE

CC3(2)=DSIGN(ONE,ABSSTRRATE)*SLIPHARD/100.0D0*ABSSTRRATE**XM*
     .        sum(thetaFS22*SUPERMAT)/SPACESIZE

CC3(3)=DSIGN(ONE,ABSSTRRATE)*SLIPHARD/100.0D0*ABSSTRRATE**XM*
     .        sum(thetaFS12*SUPERMAT)/SPACESIZE

CC3(4)=DSIGN(ONE,ABSSTRRATE)*SLIPHARD/100.0D0*ABSSTRRATE**XM*
     .        sum(thetaFS13*SUPERMAT)/SPACESIZE

CC3(5)=DSIGN(ONE,ABSSTRRATE)*SLIPHARD/100.0D0*ABSSTRRATE**XM*
     .        sum(thetaFS23*SUPERMAT)/SPACESIZE
C
C
```

```
      CALL RANK2TRANS(EIGVDP,CC3(1),CC3(2),CC3(3),CC3(4),CC3(5),
     .              dSIGTHETA)
      CC1(1)=dSIGTHETA(1)
      CC1(2)=dSIGTHETA(2)
      CC1(3)=dSIGTHETA(3)
      CC1(4)=dSIGTHETA(4)
      CC1(5)=dSIGTHETA(5)
C
C     [d(THETA)/d(DP)]
      TEMP1=-1/(DSQRT(TWO/THREE)*DSIN(THETA-PI/3))*180.0/PI
      TEM1=DP(1,1)*(DP(1,2)**2-DP(2,2)**2-DP(1,1)*DP(2,2)-
     &     DP(2,3)**2)+DP(2,2)*(DP(1,2)**2-DP(1,3)**2)+
     &     2*DP(1,2)*DP(1,3)*DP(2,3)
      TEM2=(2*(DP(1,1)**2+DP(1,2)**2+DP(1,3)**2+DP(2,2)**2+
     &     DP(2,3)**2+DP(1,1)*DP(2,2)))**(HALF)
      TEM3=TEM2**3
      TEM4=1/TEM3**2
      TEM5=THREE*(EIGDP(1)/DPNORM)**TWO-HALF
C
      CC2(1)=TEMP1*TEM4*((DP(1,2)**2-DP(2,2)**2-2*DP(1,1)*DP(2,2)-
     &      DP(2,3)**2) *TEM3 - (6*DP(1,1)+3*DP(2,2))*TEM2*TEM1)/TEM5
C
      CC2(2)=TEMP1*TEM4*((DP(1,2)**2-DP(1,1)**2-2*DP(1,1)*DP(2,2)-
     &     DP(1,3)**2) *TEM3 - (6*DP(2,2)+3*DP(1,1)) *TEM2*TEM1)/TEM5
C
      CC2(3)=TEMP1*TEM4*((2*DP(1,1)*DP(1,2)+2*DP(2,2)*DP(1,2)+
     &      2*DP(1,3)*DP(2,3)  ) *TEM3 - 6*DP(1,2) *TEM2*TEM1)/TEM5
C
      CC2(4)=TEMP1*TEM4*((-2*DP(2,2)*DP(1,3)+
     &      2*DP(1,2)*DP(2,3)) *TEM3 - 6*DP(1,3) *TEM2*TEM1)/TEM5
C
      CC2(5)=TEMP1*TEM4*((-2*DP(1,1)*DP(2,3)+
     &      2*DP(1,2)*DP(1,3))*TEM3 - 6*DP(2,3) *TEM2*TEM1)/TEM5
C
C
      DO 14 J=1,5
      DO 14 K=1,5
14    CCFINAL(J,K)= CC1(J)*CC2(K)
C
C     dSIGMA/dgD
C
      CALL MATEUL1(EIGVDP,phi1D,phiD,phi2D)
C
      DO 77 J=1,6
77    DD4(J)=ZERO
      TEMP3(1)=DCOS(phiD)*DSIN(phi1D);
```

```
      TEMP3(2)=-DCOS(phiD)*DCOS(phi1D);
      TEMP3(3)=-DSIN(phiD);
C
      TEMP1= -EIGVDP(2,1)*QCRSA(1,3) +
     &EIGVDP(1,1)*QCRSA(2,3)
      TEMP33(1,1)= -EIGVDP(2,2)*QCRSA(1,3) +
     &EIGVDP(1,2)*QCRSA(2,3)
      TEMP33(1,2)=DSIN(phiD)*DSIN(phi1D)*
     &DSIN(phi2D)*QCRSA(1,3)-DCOS(phi1D)*
     &DSIN(phiD)*DSIN(phi2D)*QCRSA(2,3)+DCOS(phiD)*
     &DSIN(phi2D)*QCRSA(3,3)
      TEMP33(1,3)=DCOS(phi2D)*DSIN(phiD)*DSIN(phi1D)*
     &QCRSA(1,3)-DCOS(phi1D)*DCOS(phi2D)*DSIN(phiD)*
     &QCRSA(2,3)+DCOS(phiD)*DCOS(phi2D)*
     &QCRSA(3,3);
      TEMP33(2,1)=-EIGVDP(2,3)*QCRSA(1,3)+
     &EIGVDP(1,3)*QCRSA(2,3)
      TEMP33(2,2)=TEMP3(1)*QCRSA(1,3)+TEMP3(2)*QCRSA(2,3)+
     &TEMP3(3)*QCRSA(3,3)
      TEMP33(2,3)=-EIGVDP(2,3)*QCRSA(1,1)+
     &EIGVDP(1,3)*QCRSA(2,1)
      TEMP33(3,1)=-EIGVDP(2,3)*QCRSA(1,2)+
     &EIGVDP(1,3)*QCRSA(2,2)
      TEMP33(3,2)=TEMP3(1)*QCRSA(1,1)+TEMP3(2)*QCRSA(2,1)+
     &TEMP3(3)*QCRSA(3,1)
      TEMP33(3,3)=TEMP3(1)*QCRSA(1,2)+TEMP3(2)*QCRSA(2,2)+
     &TEMP3(3)*QCRSA(3,2)
C
      DD4(1)=-DCOS(phi1p)**2*(TEMP1/QCRPR(2,3)-TEMP33(1,1)*
     &QCRPR(1,3)*1/QCRPR(2,3)**2)
      DD4(2)=-DCOS(phi1p)**2*(TEMP33(1,2)/QCRPR(2,3)-
     &TEMP33(1,3)*QCRPR(1,3)*1/QCRPR(2,3)**2)
      DD4(3) = -TEMP33(2,1)/DSIN(phip)
      DD4(4) = -TEMP33(2,2)/DSIN(phip)
      DD4(5)= DCOS(phi2p)**2*(TEMP33(2,3)/QCRPR(3,2)-
     &TEMP33(3,1)*QCRPR(3,1)*1/QCRPR(3,2)**2)
      DD4(6) = DCOS(phi2p)**2*(TEMP33(3,2)/QCRPR(3,2)-
     &TEMP33(3,3)*QCRPR(3,1)*1/QCRPR(3,2)**2)
C
C    [d(SIGMA_P)/d(phi1p)]

DD1(1)=DSIGN(ONE,ABSSTRRATE)*SLIPHARD/100.0D0*ABSSTRRATE**XM*
     .        sum(phi1FS11*SUPERMAT)/SPACESIZE

DD1(2)=DSIGN(ONE,ABSSTRRATE)*SLIPHARD/100.0D0*ABSSTRRATE**XM*
     .        sum(phi1FS22*SUPERMAT)/SPACESIZE
```

```
DD1(3)=DSIGN(ONE,ABSSTRRATE)*SLIPHARD/100.0D0*ABSSTRRATE**XM*
     .       sum(phi1FS12*SUPERMAT)/SPACESIZE

DD1(4)=DSIGN(ONE,ABSSTRRATE)*SLIPHARD/100.0D0*ABSSTRRATE**XM*
     .       sum(phi1FS13*SUPERMAT)/SPACESIZE

DD1(5)=DSIGN(ONE,ABSSTRRATE)*SLIPHARD/100.0D0*ABSSTRRATE**XM*
     .       sum(phi1FS23*SUPERMAT)/SPACESIZE
C
C      PART-D2: [d(SIGMA_P)/d(phip)]

DD2(1)=DSIGN(ONE,ABSSTRRATE)*SLIPHARD/100.0D0*ABSSTRRATE**XM*
     .       sum(phiFS11*SUPERMAT)/SPACESIZE

DD2(2)=DSIGN(ONE,ABSSTRRATE)*SLIPHARD/100.0D0*ABSSTRRATE**XM*
     .       sum(phiFS22*SUPERMAT)/SPACESIZE

DD2(3)=DSIGN(ONE,ABSSTRRATE)*SLIPHARD/100.0D0*ABSSTRRATE**XM*
     .       sum(phiFS12*SUPERMAT)/SPACESIZE

DD2(4)=DSIGN(ONE,ABSSTRRATE)*SLIPHARD/100.0D0*ABSSTRRATE**XM*
     .       sum(phiFS13*SUPERMAT)/SPACESIZE

DD2(5)=DSIGN(ONE,ABSSTRRATE)*SLIPHARD/100.0D0*ABSSTRRATE**XM*
     .       sum(phiFS23*SUPERMAT)/SPACESIZE
C
C     [d(SIGMA_P)/d(phi2p)]

DD3(1)=DSIGN(ONE,ABSSTRRATE)*SLIPHARD/100.0D0*ABSSTRRATE**XM*
     .       sum(phi2FS11*SUPERMAT)/SPACESIZE

DD3(2)=DSIGN(ONE,ABSSTRRATE)*SLIPHARD/100.0D0*ABSSTRRATE**XM*
     .       sum(phi2FS22*SUPERMAT)/SPACESIZE

DD3(3)=DSIGN(ONE,ABSSTRRATE)*SLIPHARD/100.0D0*ABSSTRRATE**XM*
     .       sum(phi2FS12*SUPERMAT)/SPACESIZE

DD3(4)=DSIGN(ONE,ABSSTRRATE)*SLIPHARD/100.0D0*ABSSTRRATE**XM*
     .       sum(phi2FS13*SUPERMAT)/SPACESIZE

DD3(5)=DSIGN(ONE,ABSSTRRATE)*SLIPHARD/100.0D0*ABSSTRRATE**XM*
     .       sum(phi2FS23*SUPERMAT)/SPACESIZE
C
C     [d(SIGMA_P)/d(gD)]
      DO 78,K=1,5
```

```
      DD6(K)=(DD1(K)*DD4(1)+DD2(K)*DD4(3)+DD3(K)*DD4(5))*RADDEG
      DD7(K)=(DD1(K)*DD4(2)+DD2(K)*DD4(4)+DD3(K)*DD4(6))*RADDEG
78     DD8(K)=-DD1(K)*RADDEG
C
C     [d(SIGMA)/d(gD)]
      ZA=DSIN(phiD)*DSIN(phi1D)*DSIN(phi2D)
      ZB=DCOS(phi2D)*DSIN(phiD)*DSIN(phi1D)
      ZC=DCOS(phiD)*DSIN(phi1D)
      ZD=-DCOS(phi1D)*DSIN(phiD)*DSIN(phi2D)
      ZE=-DCOS(phi1D)*DCOS(phi2D)*DSIN(phiD)
      ZF=-DCOS(phiD)*DCOS(phi1D)
      ZG= DCOS(phiD)*DSIN(phi2D)
      ZH= DCOS(phiD)*DCOS(phi2D)
      ZI=-DSIN(phiD)
      Z0=(Sp11+Sp22)
      Z1=(Sp11*EIGVDP(1,1)*2.0+Sp12*EIGVDP(1,2)*2.0+Sp13*EIGVDP(1,3)*2.)
      Z2=(Sp12*EIGVDP(1,1)*2.0+Sp22*EIGVDP(1,2)*2.0+Sp23*EIGVDP(1,3)*2.)
      Z3=(Sp13*EIGVDP(2,1)*2.0+Sp23*EIGVDP(2,2)*2.0-EIGVDP(2,3)*Z0*2.0)
      Z4=(Sp11*EIGVDP(2,1)*2.0+Sp12*EIGVDP(2,2)*2.0+Sp13*EIGVDP(2,3)*2.)
      Z5=(Sp12*EIGVDP(2,1)*2.0+Sp22*EIGVDP(2,2)*2.0+Sp23*EIGVDP(2,3)*2.)
      Z6=(Sp13*EIGVDP(1,1)+Sp23*EIGVDP(1,2)-EIGVDP(1,3)*Z0)
      Z7=(Sp13*EIGVDP(2,1)+Sp23*EIGVDP(2,2)-EIGVDP(2,3)*Z0)
      Z8=(Sp13*EIGVDP(3,1)+Sp23*EIGVDP(3,2)-EIGVDP(3,3)*Z0)
      Z9=(Sp13*EIGVDP(1,1)*2.0+Sp23*EIGVDP(1,2)*2.0-EIGVDP(1,3)*Z0*2.0)
      Z10=(Sp11*EIGVDP(1,1)+Sp12*EIGVDP(1,2)+Sp13*EIGVDP(1,3))
      Z11=(Sp12*EIGVDP(1,1)+Sp22*EIGVDP(1,2)+Sp23*EIGVDP(1,3))
      Z12=(Sp11*EIGVDP(2,1)+Sp12*EIGVDP(2,2)+Sp13*EIGVDP(2,3))
      Z13=(Sp12*EIGVDP(2,1)+Sp22*EIGVDP(2,2)+Sp23*EIGVDP(2,3))
      Z14=(Sp12*EIGVDP(3,1)+Sp22*EIGVDP(3,2)+Sp23*EIGVDP(3,3))
      Z15=(Sp11*EIGVDP(3,1)+Sp12*EIGVDP(3,2)+Sp13*EIGVDP(3,3))
      Z16=(EIGVDP(1,2)*EIGVDP(2,3)+EIGVDP(1,3)*EIGVDP(2,2))
      Z17=(EIGVDP(1,2)*EIGVDP(3,3)+EIGVDP(1,3)*EIGVDP(3,2))
      Z18=(EIGVDP(2,2)*EIGVDP(3,3)+EIGVDP(2,3)*EIGVDP(3,2))
      Z19=(EIGVDP(1,1)*EIGVDP(2,2)+EIGVDP(1,2)*EIGVDP(2,1))
      Z20=(EIGVDP(1,1)*EIGVDP(2,1)-EIGVDP(1,3)*EIGVDP(2,3))
      Z21=(EIGVDP(1,1)*EIGVDP(2,3)+EIGVDP(1,3)*EIGVDP(2,1))
      Z22=(EIGVDP(1,2)*EIGVDP(2,2)-EIGVDP(1,3)*EIGVDP(2,3))
      Z23=(EIGVDP(1,1)*EIGVDP(3,2)+EIGVDP(1,2)*EIGVDP(3,1))
      Z24=(EIGVDP(1,1)*EIGVDP(3,1)-EIGVDP(1,3)*EIGVDP(3,3))
      Z25=(EIGVDP(1,1)*EIGVDP(3,3)+EIGVDP(1,3)*EIGVDP(3,1))
      Z26=(EIGVDP(1,2)*EIGVDP(3,2)-EIGVDP(1,3)*EIGVDP(3,3))
      Z27=(EIGVDP(2,1)*EIGVDP(3,2)+EIGVDP(2,2)*EIGVDP(3,1))
      Z28=(EIGVDP(2,1)*EIGVDP(3,1)-EIGVDP(2,3)*EIGVDP(3,3))
      Z29=(EIGVDP(2,1)*EIGVDP(3,3)+EIGVDP(2,3)*EIGVDP(3,1))
      Z30=(EIGVDP(2,2)*EIGVDP(3,2)-EIGVDP(2,3)*EIGVDP(3,3))
      Z31=(EIGVDP(1,1)**2-EIGVDP(1,3)**2)
```

```
      Z32=(EIGVDP(1,2)**2-EIGVDP(1,3)**2)
      Z33=(EIGVDP(2,1)**2-EIGVDP(2,3)**2)
      Z34=(EIGVDP(2,2)**2-EIGVDP(2,3)**2)
C
C     dStressDij_dphi1D
      DD5(1) = DD6(1)*Z31+DD6(2)*Z32-EIGVDP(2,3)*Z9-EIGVDP(2,1)*Z1-
     &     EIGVDP(2,2)*Z2+DD6(3)*EIGVDP(1,1)*EIGVDP(1,2)*2.0+DD6(4)*
     &     EIGVDP(1,1)*EIGVDP(1,3)*2.0+DD6(5)*EIGVDP(1,2)*EIGVDP(1,3)*2.0
      DD5(2) = DD6(1)*Z33+DD6(2)*Z34+EIGVDP(1,3)*Z3+EIGVDP(1,1)*Z4+
     &     EIGVDP(1,2)*Z5+DD6(3)*EIGVDP(2,1)*EIGVDP(2,2)*2.0+DD6(4)*
     &     EIGVDP(2,1)*EIGVDP(2,3)*2.0+DD6(5)*EIGVDP(2,2)*EIGVDP(2,3)*2.0
      DD5(3) = EIGVDP(1,3)*Z6-EIGVDP(2,3)*Z7+EIGVDP(1,1)*Z10+
     &     EIGVDP(1,2)*Z11-EIGVDP(2,1)*Z12-EIGVDP(2,2)*Z13+DD6(3)*
     &     Z19+DD6(1)*Z20+DD6(4)*Z21+DD6(2)*Z22+DD6(5)*Z16
      DD5(4)=-EIGVDP(2,3)*Z8-EIGVDP(2,1)*Z15-EIGVDP(2,2)*Z14+DD6(3)*Z23+
     &     DD6(1)*Z24+DD6(4)*Z25+DD6(2)*Z26+DD6(5)*Z17
      DD5(5)= EIGVDP(1,3)*Z8+EIGVDP(1,1)*Z15+EIGVDP(1,2)*Z14+DD6(3)*Z27+
     &     DD6(1)*Z28+DD6(4)*Z29+DD6(2)*Z30+DD6(5)*Z18
C
C     dStressDij_dphiD
      EE1(1) = DD7(1)*Z31+DD7(2)*Z32+ZC*Z9+ZA*Z1+ZB*Z2+DD7(3)*
     &     EIGVDP(1,1)*EIGVDP(1,2)*2.0+DD7(4)*EIGVDP(1,1)*EIGVDP(1,3)*
     &     2.0+DD7(5)*EIGVDP(1,2)*EIGVDP(1,3)*2.0
      EE1(2) = DD7(1)*Z33+DD7(2)*Z34+ZF*Z3+ZD*Z4+ZE*Z5+DD7(3)*
     &     EIGVDP(2,1)*EIGVDP(2,2)*2.0+DD7(4)*EIGVDP(2,1)*EIGVDP(2,3)*
     &     2.0+DD7(5)*EIGVDP(2,2)*EIGVDP(2,3)*2.0
      EE1(3) = ZF*Z6+ZC*Z7+ZD*Z10+ZE*Z11+ZA*Z12+ZB*Z13+DD7(3)*
     &     Z19+DD7(1)*Z20+DD7(4)*Z21+DD7(2)*Z22+DD7(5)*Z16
      EE1(4) = ZI*Z6+ZC*Z8+ZG*Z10+ZH*Z11+ZA*Z15+ZB*Z14+DD7(3)*Z23+
     &     DD7(1)*Z24+DD7(4)*Z25+DD7(2)*Z26+DD7(5)*Z17
      EE1(5) = ZI*Z7+ZF*Z8+ZG*Z12+ZH*Z13+ZD*Z15+ZE*Z14+DD7(3)*Z27+
     &     DD7(1)*Z28+DD7(4)*Z29+DD7(2)*Z30+DD7(5)*Z18
C
C     dStressDij_dphi2D
      FF1(1) = DD8(1)*Z31+DD8(2)*Z32+EIGVDP(1,2)*Z1-EIGVDP(1,1)*
     &     Z2+DD8(3)*EIGVDP(1,1)*EIGVDP(1,2)*2.0+DD8(4)*EIGVDP(1,1)*
     &     EIGVDP(1,3)*2.0+DD8(5)*EIGVDP(1,2)*EIGVDP(1,3)*2.0
      FF1(2) = DD8(1)*Z33+DD8(2)*Z34+EIGVDP(2,2)*Z4-EIGVDP(2,1)*
     &     Z5+DD8(3)*EIGVDP(2,1)*EIGVDP(2,2)*2.0+DD8(4)*EIGVDP(2,1)*
     &     EIGVDP(2,3)*2.0+DD8(5)*EIGVDP(2,2)*EIGVDP(2,3)*2.0
      FF1(3)=EIGVDP(2,2)*Z10-EIGVDP(2,1)*Z11+EIGVDP(1,2)*Z12-EIGVDP(1,1)
     &     *Z13+DD8(3)*Z19+DD8(1)*Z20+DD8(4)*Z21+DD8(2)*Z22+DD8(5)*Z16
      FF1(4)=EIGVDP(3,2)*Z10-EIGVDP(3,1)*Z11+EIGVDP(1,2)*Z15-EIGVDP(1,1)
     &     *Z14+DD8(3)*Z23+DD8(1)*Z24+DD8(4)*Z25+DD8(2)*Z26+DD8(5)*Z17
      FF1(5)=EIGVDP(3,2)*Z12-EIGVDP(3,1)*Z13+EIGVDP(2,2)*Z15-EIGVDP(2,1)
     &     *Z14+DD8(3)*Z27+DD8(1)*Z28+DD8(4)*Z29+DD8(2)*Z30+DD8(5)*Z18
```

```
C
C    [dgD/dD]
      C1=DCOS(phi1D)
      C2=DCOS(phiD)
      C3=DCOS(phi2D)
      S1=DSIN(phi1D)
      S2=DSIN(phiD)
      S3=DSIN(phi2D)
      C1C1=C1**2
      C2C2=C2**2
      C3C3=C3**2
      S1S1=S1**2
      S2S2=S2**2
      S3S3=S3**2
      C1C3=C1*C3
      C2C3=C2*C3
      C2C1=C2*C1
      S2S1=S2*S1
      S1S3=S1*S3
      S2S3=S2*S3
C
      TEMP33(1,1) = DP(1,2)*(C2C1*S1*4.0+C3*S3*2.0-C2C1*C3C3*S1*8.0-
     &C1C1*C3*S3*4.0+C2C2*C3*S3*2.0-C1C1*C2C2*C3*S3*4.0)-DP(1,3)*
     &(-S2S1+C3C3*S2S1*2.0+C1C3*C2*S2S3*2.0)-DP(2,3)*(C1*S2-C1*C3C3*S2*
     &2.0+C2C3*S2S1*S3*2.0)+DP(1,1)*(-C2+C1C1*C2*2.0+C2*C3C3*2.0+
     &C1C3*S1S3*2.0-C1C1*C2*C3C3*4.0+C1C3*C2C2*S1S3*2.0)-DP(2,2)*
     &(-C2+C1C1*C2*2.0+C2*C3C3*2.0+C1C3*S1S3*2.0-C1C1*C2*C3C3*4.0+
     &C1C3*C2C2*S1S3*2.0)
C
      TEMP33(1,2)= -DP(1,3)*(C2C1-C2C1*C3C3*2.0-C3*S1S3*2.0+
     &C2C2*C3*S1S3*4.0)-DP(2,3)*(C2*S1+C1C3*S3*2.0-C2*C3C3*S1*2.0-
     &C1C3*C2C2*S3*4.0)-DP(1,1)*(C1*S2S1+C2C3*S2S3*4.0-C1*C3C3*S2S1*2.0
     &-C1C1*C2*C3*S2S3*2.0)-DP(2,2)*(-C1*S2S1+C2C3*S2S3*2.0+
     &C1*C3C3*S2S1*2.0+C1C1*C2*C3*S2S3*2.0)+DP(1,2)*(-S2+C1C1*S2*2.0+
     &C3C3*S2*2.0-C1C1*C3C3*S2*4.0+C1C3*C2*S2S1*S3*4.0)
C
      TEMP33(1,3)= DP(1,1)*(C1C1-C2C2*2.0-C3C3*2.0+C1C1*C2C2-C1C1*C3C3*
     &2.0+C2C2*C3C3*4.0-C1C1*C2C2*C3C3*2.0+C1C3*C2*S1S3*4.0+1.0)+
     &DP(1,2)*(C1*S1*2.0+C2C3*S3*4.0+C1*C2C2*S1*2.0-C1*C3C3*S1*4.0-
     &C1*C2C2*C3C3*S1*4.0-C1C1*C2*C3*S3*8.0)-DP(1,3)*(C1C3*S2S3*4.0-
     &C2*S2S1*2.0+C2*C3C3*S2S1*4.0)-DP(2,3)*(C2C1*S2*2.0-C2C1*C3C3*S2*
     &4.0+C3*S2S1*S3*4.0)-DP(2,2)*(C1C1+C2C2+C3C3*4.0+C1C1*C2C2-
     &C1C1*C3C3*2.0-C2C2*C3C3*2.0-C1C1*C2C2*C3C3*2.0+
     &C1C3*C2*S1S3*4.0-2.0)
C
      TEMP33(2,1)= DP(1,2)*(C1C3*S2S1*4.0-C2*S2S3*2.0+C1C1*C2*S2S3*4.0)
```

```
     &-DP(1,3)*(C2C3*S1-C1*S3+C1*C2C2*S3*2.0)-DP(1,1)*(C3*S2-
     &C1C1*C3*S2*2.0+C2C1*S2S1*S3*2.0)+DP(2,2)*(C3*S2-C1C1*C3*S2*2.0+
     &C2C1*S2S1*S3*2.0)+DP(2,3)*(S1S3+C1C3*C2-C2C2*S1S3*2.0)
C
      TEMP33(2,2)= -DP(1,3)*(C1C3*S2-C2*S2S1*S3*4.0)-DP(2,3)*
     &(C2C1*S2S3*4.0+C3*S2S1)+DP(1,1)*(S3*2.0-C1C1*S3-C2C2*S3*4.0+
     &C1C3*C2*S1+C1C1*C2C2*S3*2.0)+DP(1,2)*(C2C3-C1*S1S3*2.0-C1C1*C2*
     &C3*2.0+C1*C2C2*S1S3*4.0)-DP(2,2)*(-S3-C1C1*S3+C2C2*S3*2.0+
     &C1C3*C2*S1+C1C1*C2C2*S3*2.0)
C
      TEMP33(2,3)= DP(1,2)*(-S2S3+C1C1*S2S3*2.0+C1C3*C2*S2S1*2.0)-
     &DP(1,3)*(-C3*S1+C2C1*S3+C2C2*C3*S1*2.0)-DP(2,2)*(C2C3*S2-
     &C1*S2S1*S3+C1C1*C2*C3*S2)-DP(2,3)*(C1C3-C1C3*C2C2*2.0+C2*S1S3)-
     &DP(1,1)*(C2C3*S2*2.0+C1*S2S1*S3-C1C1*C2*C3*S2)

      TEMP33(3,1)= -DP(1,1)*(-S2S3+C1C1*S2S3*2.0+C1C3*C2*S2S1*2.0)+
     &DP(2,2)*(-S2S3+C1C1*S2S3*2.0+C1C3*C2*S2S1*2.0)-DP(2,3)*(-C3*S1+
     &C2C1*S3+C2C2*C3*S1*2.0)+DP(1,3)*(C1C3-C1C3*C2C2*2.0+C2*S1S3)-
     &DP(1,2)*(C2C3*S2*2.0+C1*S2S1*S3*4.0-C1C1*C2*C3*S2*4.0)
C
      TEMP33(3,2)= DP(2,3)*(S2S1*S3-C1C3*C2*S2*4.0)-DP(1,2)*(C1C3*S1*
     &2.0+C2*S3-C1C3*C2C2*S1*4.0-C1C1*C2*S3*2.0)+DP(1,3)*(C1*S2S3+C2C3*
     &S2S1*4.0)-DP(1,1)*(C3*-2.0+C1C1*C3+C2C2*C3*4.0+C2C1*S1S3-C1C1*
     &C2C2*C3*2.0)+DP(2,2)*(C3+C1C1*C3-C2C2*C3*2.0+C2C1*S1S3-
C1C1*C2C2*
     &C3*2.0)
C
      TEMP33(3,3)=  DP(2,2)*(C1C3*S2S1+C2*S2S3+C1C1*C2*S2S3)-DP(2,3)*
     &(C2C3*S1-C1*S3+C1*C2C2*S3*2.0)-DP(1,2)*(C3*S2-C1C1*C3*S2*2.0+
     &C2C1*S2S1*S3*2.0)-DP(1,1)*(C1C3*S2S1-C2*S2S3*2.0+C1C1*C2*S2S3)-
     &DP(1,3)*(S1S3+C1C3*C2-C2C2*S1S3*2.0)
C
      TEMP1 = TEMP33(1,1)*(TEMP33(2,2)*TEMP33(3,3)-
     &                TEMP33(2,3)*TEMP33(3,2))-
     &       TEMP33(1,2)*(TEMP33(2,1)*TEMP33(3,3)-
     &                TEMP33(3,1)*TEMP33(2,3))+
     &       TEMP33(1,3)*(TEMP33(2,1)*TEMP33(3,2)-
     &                TEMP33(3,1)*TEMP33(2,2))
C
      CALL MAT3INV(TEMP33,TEMP33)
C     dgDdD11
      TEMP3(1)= C1C1*C3*S3+C3*S2S2*S3+C2C1*C3C3*S1-C2C1*S1*S3S3-
     &          C2C2*C3*S1S1*S3
      TEMP3(2)= C2*S2S3+C2*S2*S1S1*S3-C1C3*S2S1
      TEMP3(3)= C2C3*S2+C2C3*S2*S1S1+C1*S2S1*S3
      DO 15 J=1,3
```

```
15    dgDdD11(J)=(TEMP33(J,1)*TEMP3(1)+TEMP33(J,2)*TEMP3(2)+
     &          TEMP33(J,3)*TEMP3(3))
C
C     dgDdD22
      TEMP3(1) =C3*S2S2*S3+C3*S1S1*S3-C2C1*C3C3*S1+C2C1*S1*S3S3-
     &      C2C2*C1C1*C3*S3
      TEMP3(2)=  C2*S2S3+C2*C1C1*S2S3+C1C3*S2S1
      TEMP3(3)= C2C3*S2+C2*C1C1*C3*S2-C1*S2S1*S3
      DO 16 J=1,3
16    dgDdD22(J)=(TEMP33(J,1)*TEMP3(1)+TEMP33(J,2)*TEMP3(2)+
     &          TEMP33(J,3)*TEMP3(3))
C
C     dgDdD12
      TEMP3(1)=-C2*C1C1*C3C3+C2*C1C1*S3S3+C2*C3C3*S1S1-C2*S1S1*S3S3+
     &         C1C3*S1S3*2.0+C2C2*C1C3*S1S3*2.0
      TEMP3(2)=C1C1*C3*S2-C3*S2*S1S1-C2C1*S2S1*S3*2.0
      TEMP3(3)=-C1C1*S2S3+S2*S1S1*S3-C2*C1C3*S2S1*2.0
      DO 18 J=1,3
18    dgDdD12(J)=(TEMP33(J,1)*TEMP3(1)+TEMP33(J,2)*TEMP3(2)+
     &          TEMP33(J,3)*TEMP3(3))
C
C     dgDdD13
      TEMP3(1) =-C1*C3C3*S2+C1*S2*S3S3+C2C3*S2S1*S3*2.0
      TEMP3(2)=  C2C2*S1S3-S2S2*S1S3-C2*C1C3
      TEMP3(3)=  C2C2*C3*S1-C3*S2S2*S1+C2C1*S3
      DO 21 J=1,3
21    dgDdD13(J)=(TEMP33(J,1)*TEMP3(1)+TEMP33(J,2)*TEMP3(2)+
     &          TEMP33(J,3)*TEMP3(3))
C
C     dgDdD23
      TEMP3(1) =-C3C3*S2S1+S2S1*S3S3-C2*C1C3*S2S3*2.0
      TEMP3(2)=-C2C2*C1*S3+C1*S2S2*S3-C2C3*S1
      TEMP3(3)= -C2C2*C1C3+C1C3*S2S2+C2*S1S3
      DO 22 J=1,3
22    dgDdD23(J)=(TEMP33(J,1)*TEMP3(1)+TEMP33(J,2)*TEMP3(2)+
     &          TEMP33(J,3)*TEMP3(3))
C
C
      DO 23 J=1,5
      DDFINAL(J,1)= DD5(J)*dgDdD11(1)
      DDFINAL(J,2)= DD5(J)*dgDdD22(1)
      DDFINAL(J,3)= DD5(J)*dgDdD12(1)
      DDFINAL(J,4)= DD5(J)*dgDdD13(1)
      DDFINAL(J,5)= DD5(J)*dgDdD23(1)
C
      EEFINAL(J,1)= EE1(J)*dgDdD11(2)
```

```
      EEFINAL(J,2)= EE1(J)*dgDdD22(2)
      EEFINAL(J,3)= EE1(J)*dgDdD12(2)
      EEFINAL(J,4)= EE1(J)*dgDdD13(2)
      EEFINAL(J,5)= EE1(J)*dgDdD23(2)
C
      FFFINAL(J,1)= FF1(J)*dgDdD11(3)
      FFFINAL(J,2)= FF1(J)*dgDdD22(3)
      FFFINAL(J,3)= FF1(J)*dgDdD12(3)
      FFFINAL(J,4)= FF1(J)*dgDdD13(3)
23    FFFINAL(J,5)= FF1(J)*dgDdD23(3)
C
C     DERIVATIVES OF Slip resistance W.R.T DP
      IF (DABS(HO-0.0) .GE. 1.0D-8) THEN   !(i.e. with hardening, HO .NE. ZERO)
C
        SS1=TOTGAMMA/DPNORM
C
        SS3=ABSSTRRATE*sum(thetaGD*SUPERMAT)/SPACESIZE
C
C       d(gammaddot)/d(gp)
        SS5=ABSSTRRATE*sum(phi1GD*SUPERMAT)/SPACESIZE
        SS6=ABSSTRRATE*sum(phiGD*SUPERMAT)/SPACESIZE
        SS7=ABSSTRRATE*sum(phi2GD*SUPERMAT)/SPACESIZE
C
C       d(gammaddot)/d(gD)
        SS9 = (SS5*DD4(1)+ SS6*DD4(3)+ SS7*DD4(5))*RADDEG
        SS10 =(SS5*DD4(2)+ SS6*DD4(4)+ SS7*DD4(6))*RADDEG
        SS11 =-SS5*RADDEG
C
        CONST=HO*(1-(SLIPHARDt/SS))**AEXP*DTIME
C
        SSFINAL(1) = CONST*(SS1*AA2(1) + SS3*CC2(1) +
     .          SS9*dgDdD11(1)+ SS10*dgDdD11(2) + SS11*dgDdD11(3))
        SSFINAL(2) = CONST*(SS1*AA2(2) + SS3*CC2(2) +
     .          SS9*dgDdD22(1)+ SS10*dgDdD22(2) + SS11*dgDdD22(3))
        SSFINAL(3) = CONST*(SS1*AA2(3) + SS3*CC2(3) +
     .          SS9*dgDdD12(1)+ SS10*dgDdD12(2) + SS11*dgDdD12(3))
        SSFINAL(4) = CONST*(SS1*AA2(4) + SS3*CC2(4) +
     .          SS9*dgDdD13(1)+ SS10*dgDdD13(2) + SS11*dgDdD13(3))
        SSFINAL(5) = CONST*(SS1*AA2(5) + SS3*CC2(5) +
     .          SS9*dgDdD23(1)+ SS10*dgDdD23(2) + SS11*dgDdD23(3))
C
        ZZ(1)=DFTSIG(1)/SLIPHARD
        ZZ(2)=DFTSIG(2)/SLIPHARD
        ZZ(3)=DFTSIG(3)/SLIPHARD
        ZZ(4)=DFTSIG(4)/SLIPHARD
        ZZ(5)=DFTSIG(5)/SLIPHARD
```

```
C
C
      DO 35,I=1,5
      DO 35,J=1,5
35     dDFTSIGdDP(I,J)=AAFINAL(I,J)+CCFINAL(I,J)+DDFINAL(I,J)+
     .               EEFINAL(I,J)+FFFINAL(I,J)+
     .               SSFINAL(I)*ZZ(J)
C
    ELSE
      DO 36,I=1,5
      DO 36,J=1,5
36     dDFTSIGdDP(I,J)=AAFINAL(I,J)+CCFINAL(I,J)+DDFINAL(I,J)+
     .               EEFINAL(I,J)+FFFINAL(I,J)
C
    ENDIF
C
    RETURN
    END
CCCCCCCCCCCCCCCCCCCC
    SUBROUTINE ROTMAT(WS12,WS13,WS23,rot)
    IMPLICIT REAL*8(A-H,O-Z)
    DIMENSION tmp(3),rot(3,3),axis2(3)
C
    tmp(1)=WS23          !This is ws32 and not ws23
    tmp(2)=-WS13         !This is ws31 and not ws13
    tmp(3)=WS12          !This is ws21 and not ws12
    rnorm=dsqrt(tmp(1)**2+tmp(2)**2+tmp(3)**2)
C
    do 55, i=1,3
     tmp(i)=tmp(i)/rnorm
     axis2(i)=tmp(i)**2
55    continue
C
      cc=dcos(rnorm)
      ss=dsin(rnorm)
      rot(1,1)=axis2(1)+cc*(1-axis2(1))
      rot(2,2)=axis2(2)+cc*(1-axis2(2))
      rot(3,3)=axis2(3)+cc*(1-axis2(3))
      rot(1,2)=(1.-cc)*tmp(1)*tmp(2)+ss*tmp(3)
      rot(2,1)=(1.-cc)*tmp(1)*tmp(2)-ss*tmp(3)
      rot(2,3)=(1.-cc)*tmp(2)*tmp(3)+ss*tmp(1)
      rot(3,2)=(1.-cc)*tmp(2)*tmp(3)-ss*tmp(1)
      rot(3,1)=(1.-cc)*tmp(1)*tmp(3)+ss*tmp(2)
      rot(1,3)=(1.-cc)*tmp(1)*tmp(3)-ss*tmp(2)
C
      RETURN
```

```
      END
CCCCCCCCCCCCCCCCCC
      SUBROUTINE MATEUL1(AA,pphi1,pphi,pphi2)
      IMPLICIT REAL*8(A-H,O-Z)
      REAL*8 AA,pphi1,pphi,pphi2
      DIMENSION AA(3,3)
     PI = 4.0*DATAN(1.0D0)
     SMALL=1.0D-12
     IF (DABS(DABS(AA(3,3))-1.0D0).LT. SMALL) THEN
      pphi1=DATAN2(AA(2,1),AA(1,1))
      pphi=0.0D0
      pphi2=0.0D0
      IF (AA(3,3).LT. ZERO) pphi=PI
      IF (pphi1 .LT. ZERO) pphi1=2*PI+pphi1
      RETURN
      ENDIF
C
      pphi=DACOS(AA(3,3))
      pphi1=DATAN2(AA(1,3)/DSIN(pphi),
     &  -AA(2,3)/DSIN(pphi))
      pphi2=DATAN2(AA(3,1)/DSIN(pphi),
     &  AA(3,2)/DSIN(pphi))
      if (pphi .lt. ZERO) pphi=2*PI+pphi
      if (pphi1 .lt. ZERO) pphi1=2*PI+pphi1
      if (pphi2 .lt. ZERO) pphi2=2*PI+pphi2
C
54     CONTINUE
      RETURN
      END
CCCCCCCCCCCCCCCCCC
      SUBROUTINE EULMAT(ANG1,ANG2,ANG3,QQ)
C
      IMPLICIT NONE
      REAL*8          :: SOM, COM, STH, CTH, SPH, CPH, ANG1,ANG2,ANG3
      REAL*8, DIMENSION(3,3)        :: QQ
C
     SPH = DSIN(ANG1)
     CPH = DCOS(ANG1)
     STH = DSIN(ANG2)
     CTH = DCOS(ANG2)
     SOM = DSIN(ANG3)
     COM = DCOS(ANG3)
C
     QQ(1,1) = CPH*COM-SPH*SOM*CTH
     QQ(1,2) = -CPH*SOM-SPH*COM*CTH
     QQ(1,3) = STH*SPH
```

```
      QQ(2,1) = SPH*COM+SOM*CPH*CTH
      QQ(2,2) = -SPH*SOM+CPH*COM*CTH
      QQ(2,3) = -STH*CPH
      QQ(3,1) = STH*SOM
      QQ(3,2) = STH*COM
      QQ(3,3) = CTH
C
      RETURN
      END
CCCCCCCCCCCCCCCCCC
      SUBROUTINE SDVINI(STATEV,COORDS,NSTATV,NCRDS,NOEL,NPT,
     1  LAYER,KSPT)
      USE CommonModule
      IMPLICIT NONE
      INTEGER                  :: NSTATV,NCRDS,NOEL,NPT,LAYER,KSPT
      REAL*8, DIMENSION(NSTATV)     :: STATEV
      REAL*8, DIMENSION(NCRDS)      :: COORDS
      INTEGER                  :: ICRYS, IND
      REAL*8, DIMENSION(3,3)        :: QCRSA
      REAL*8, DIMENSION(6,6)        :: SumJAC, OLDJAC,ELAS
C
C     INITIALZE STATE VARIABLES
C     FIRST, SET SumJAC(:,:)=0
      DO J = 1,6
        DO K = 1,6
          SumJAC(K,J) = ZERO
        ENDDO
      ENDDO
      ind=1
      InitialCrystalLoop: DO K=1,NCRYSINITIAL
        ICRYS=K
        IF (KELMFLAG .EQ. 1) THEN
          ICRYS =(NOEL-1)*NINTG+NPT
        ENDIF
!
        CALL EULMAT(phi1(ICRYS)*DEGRAD,
     .              phi(ICRYS)*DEGRAD,
     .              phi2(ICRYS)*DEGRAD,
     .              QCRSA)
        STATEV(ind)=SO
        STATEV(ind+1)=QCRSA(1,1)
        STATEV(ind+2)=QCRSA(1,2)
        STATEV(ind+3)=QCRSA(1,3)
        STATEV(ind+4)=QCRSA(2,1)
        STATEV(ind+5)=QCRSA(2,2)
        STATEV(ind+6)=QCRSA(2,3)
```

```
      STATEV(ind+7)=QCRSA(3,1)
      STATEV(ind+8)=QCRSA(3,2)
      STATEV(ind+9)=QCRSA(3,3)
!
      DO I = 1,6
        DO J = 1,6
          IF (isoflag .EQ. 1) THEN
            OLDJAC(I,J)=ELASiso(I,J)
          ELSE
          CALL ELAST(QCRSA,OLDJAC)
          ENDIF
          IF(I.GT.3)THEN
           OLDJAC(I,J) = OLDJAC(I,J)*HALF
          ENDIF
        SumJAC(I,J) = SumJAC(I,J)+OLDJAC(I,J)
        ENDDO
      ENDDO
      ind=ind+10
    ENDDO InitialCrystalLoop
!
    DO J = 1,6
      DO K = 1,6
        STATEV(ind)  = SumJAC(K,J)/NCRYSINITIAL
        ind=ind+1
      ENDDO
    ENDDO
C
    RETURN
    END
CCCCCCCCCCCCCCCCCC
    SUBROUTINE UEXTERNALDB(LOP,LRESTART,TIME,DTIME,KSTEP,KINC)
    USE CommonModule
    IMPLICIT NONE
    INTEGER                  :: LOP, LRESTART,KSTEP,KINC
    REAL*8                   :: DTIME
    REAL*8, DIMENSION(2)         :: TIME
C    -----------
C    LOAD SPECTRAL DATABASES AND TEXTURE AT THE BEGINNING OF
THE ANALYSIS (LOP=0)
    IF(LOP.EQ.0)THEN
     CALL LOADDATABASE()
     CALL LOADDATEXTURE()
C    ----------
    RETURN
    END
```

REFERENCES

ABAQUS, 2010. © Dassault Systèmes Simulia Corp., Providence, RI, USA.

Adams, B.L., Gao, X., Kalidindi, S.R., 2005. Finite approximations to the second-order properties closure in single phase polycrystals. Acta Materialia 53, 3563-3577.

Adams, B.L., Henrie, A., Henrie, B., Lyon, M., Kalidindi, S.R., Garmestani, H., 2001. Microstructure-sensitive design of a compliant beam. Journal of the Mechanics and Physics of Solids 49, 1639-1663.

Adams, B.L., Lyon, M., Henrie, B., 2004. Microstructures by design: linear problems in elastic-plastic design. Int J Plasticity 20, 1577-1602.

Al-Harbi, H.F., Knezevic, M., Kalidindi, S.R., 2010. Spectral Approaches for the Fast Computation of Yield Surfaces and First-Order Plastic Property Closures for Polycrystalline Materials with Cubic-Triclinic Textures. Cmc-Computers Materials & Continua 15, 153-172.

Al-Harbi, H.F., Landi, G., Kalidindi, S.R., 2012. Multi-scale modeling of the elastic response of a structural component made from a composite material using the materials knowledge system. Modelling and Simulation in Materials Science and Engineering 20.

Allison, J., 2011. Integrated Computational Materials Engineering: a Perspective on Progress and Future Steps. Jom 63, 15-18.

Asaro, R.J., Needleman, A., 1985a. Overview no. 42 Texture development and strain hardening in rate dependent polycrystals. Acta Metallurgica 33, 923-953.

Asaro, R.J., Needleman, A., 1985b. Texture development and strain hardening in rate dependent polycrystals. Acta Metallurgica et Materialia 33, 923-953.

ASTM-E562-02, 2002. Standard Test Method for Determining Volume Fraction by Systematic Manual Point
Count. ASTM International, 100 Barr Harbor Dr. P.O. box C-700 West Conshohocken, Pennsylvania 19428-2959, United States.

Bachu, V., Kalidindi, S.R., 1998. On the accuracy of the predictions of texture evolution by the finite element technique for fcc polycrystals. Materials Science and Engineering a-Structural Materials Properties Microstructure and Processing 257, 108-117.

Barlat, F., 1987. Crystallographic texture, anisotropic yield surfaces and forming limits of sheet metals Materials Science and Engineering - 91, - 72.

Barlat, F., Lian, K., 1989. Plastic behavior and stretchability of sheet metals. Part I: A yield function for orthotropic sheets under plane stress conditions International Journal of Plasticity - 5, - 66.

Bhattacharyya, A., El-Danaf, E., Kalidindi, S.R., Doherty, R.D., 2001. Evolution of grain-scale microstructure during large strain simple compression of polycrystalline aluminum with quasi-columnar grains: OIM measurements and numerical simulations. International Journal of Plasticity 17, 861-883.

BIELER, S.L.S.a.T.R., 2001. Effect of Texture Changes on Flow Softening during Hot Working of Ti-6Al-4V. METALLURGICAL AND MATERIALS TRANSACTIONS A 32A, 1871-1875.

Binci, M., Fullwood, D., Kalidindi, S.R., 2008. A new spectral framework for establishing localization relationships for elastic behavior of composites and their calibration to finite-element models. Acta Materialia 56, 2272-2282.

Bonilla, L.L., Carpio, A., Plans, I., 2007. Dislocations in cubic crystals described by discrete models. Physica A: Statistical Mechanics and its Applications 376, 361-377.

Bridier, F., McDowell, D.L., Villechaise, P., Mendez, J., 2009. Crystal plasticity modeling of slip activity in Ti–6Al–4V under high cycle fatigue loading. International Journal of Plasticity 25, 1066-1082.

Briggs, W.L., Henson, V.E., 1995. The DFT : an owner's manual for the discrete Fourier transform. Society for Industrial and Applied Mathematics, Philadelphia.

Brigham, E.O., 1988a. The fast Fourier transform and applications. Prentice Hall, Englewood Cliffs, NJ.

Brigham, E.O., 1988b. The fast Fourier transform and its applications. Prentice Hall, Englewood Cliffs.

Bronkhorst, C.A., Kalidindi, S.R., Anand, L., 1992a. POLYCRYSTALLINE PLASTICITY AND THE EVOLUTION OF CRYSTALLOGRAPHIC TEXTURE IN FCC METALS. Philosophical Transactions of the Royal Society of London Series a-Mathematical Physical and Engineering Sciences 341, 443-477.

Bronkhorst, C.A., Kalidindi, S.R., Anand, L., 1992b. Polycrystalline plasticity and the evolution of crystallographic texture in FCC metals. Philosophical Transactions of the Royal Society of London Series A –Mathematical Physical and Engineering Sciences 341, 443–477.

Brown, S.B., Kim, K.H., Anand, L., 1989. An internal variable constitutive model for hot working of metals. International Journal of Plasticity 5, 95-130.

Bunge, H.-J., 1993a. Texture Analysis in Materials Science. Mathematical Methods, Cuvillier Verlag, Göttingen.

Bunge, H.-J., 1993b. Texture analysis in materials science. Mathematical Methods. Cuvillier Verlag, Göttingen.

Bunge, H.J., Esling, C., 1984. Texture development by plastic deformation. Scripta Metallurgica 18, 191-195.

Calcagnotto, M., Ponge, D., Demir, E., Raabe, D., 2010. Orientation gradients and geometrically necessary dislocations in ultrafine grained dual-phase steels studied by 2D and 3D EBSD. Materials Science and Engineering: A 527, 2738-2746.

Cazacu, O., Plunkett, B., Barlat, F., 2006. Orthotropic yield criterion for hexagonal closed packed metals International Journal of Plasticity - 22, - 1194.

Choi, S.H., Kim, D.W., Seong, B.S., Rollett, A.D., 2011. 3-D simulation of spatial stress distribution in an AZ31 Mg alloy sheet under in-plane compression. International Journal of Plasticity 27, 1702-1720.

Choi, S.H., Kim, E.Y., Woo, W., Han, S.H., Kwak, J.H., 2013. The effect of crystallographic orientation on the micromechanical deformation and failure behaviors of DP980 steel during uniaxial tension. International Journal of Plasticity 45, 85-102.

Christian, J.W., Mahajan, S., 1995. Deformation twinning. Progress in Materials Science 39, 1-157.

Chun, Y.B., Yu, S.H., Semiatin, S.L., Hwang, S.K., 2005. Effect of deformation twinning on microstructure and texture evolution during cold rolling of CP-titanium. Materials Science and Engineering: A 398, 209-219.

Clément, A., Coulomb, P., 1979. Eulerian simulation of deformation textures. Scripta Metallurgica 13, 899-901.

Conrad, H., 1981. Effect of interstitial solutes on the strength and ductility of titanium. Progress in Materials Science 26, 123-403.

Cooley, J.W., Tukey, J.W., 1965. Algorithm for the machine computation of complex Fourier series. Mathematics of Computation 19, 297-301.

Cuitino, A.M., Ortiz, M., 1993. Computational modelling of single crystals. Modelling and Simulation in Materials Science and Engineering 1, 225.

Delaire, F., Raphanel, J.L., Rey, C., 2000. Plastic heterogeneities of a copper multicrystal deformed in uniaxial tension: experimental study and finite element simulations. Acta Materialia 48, 1075-1087.

Delannay, L., Jacques, P.J., Kalidindi, S.R., 2006. Finite element modeling of crystal plasticity with grains shaped as truncated octahedrons. International Journal of Plasticity 22, 1879-1898.

Delannay, L., Kalidindi, S.R., Van Houtte, P., 2002. Quantitative prediction of textures in aluminium cold rolled to moderate strains. Materials Science and Engineering A 336, 233-244.

Duhamel, P., Vetterli, M., 1990a. Fast Fourier Transforms: A Tutorial Review and a State of the Art. Signal Processing 19, 259-299.

Duhamel, P., Vetterli, M., 1990b. Fast fourier transforms: A tutorial review and a state of the art. Signal Processing 19, 259-299.

Elmustafa, A.A., Stone, D.S., 2003. Nanoindentation and the indentation size effect: Kinetics of deformation and strain gradient plasticity. Journal of the Mechanics and Physics of Solids 51, 357-381.

Erieau, P., Rey, C., 2004. Modeling of deformation and rotation bands and of deformation induced grain boundaries in IF steel aggregate during large plane strain compression. International Journal of Plasticity 20, 1763-1788.

Fast, T., Kalidindi, S.R., 2011. Formulation and calibration of higher-order elastic localization relationships using the MKS approach. Acta Materialia 59, 4595-4605.

Fast, T., Knezevic, M., Kalidindi, S.R., 2008. Application of microstructure sensitive design to structural components produced from hexagonal polycrystalline metals. Computational Materials Science 43, 374-383.

Fast, T., Niezgoda, S.R., Kalidindi, S.R., 2011. A new framework for computationally efficient structure-structure evolution linkages to facilitate high-fidelity scale bridging in multi-scale materials models. Acta Materialia 59, 699-707.

Fullwood, D.T., Adams, B.L., Kalidindi, S.R., 2007. Generalized Pareto front methods applied to second-order material property closures. Computational Materials Science 38, 788-799.

Garmestani, H., Kalidindi, S.R., Williams, L., Bacaltchuk, C.M., Fountain, C., Lee, E.W., Es-Said, O.S., 2002. Modeling the evolution of anisotropy in Al–Li alloys: application to Al–Li 2090-T8E41. International Journal of Plasticity 18, 1373-1393.

Goh, C.-H., Neu, R.W., McDowell, D.L., 2003. Crystallographic plasticity in fretting of Ti–6AL–4V. International Journal of Plasticity 19, 1627-1650.

Grushko, B., Weiss, B.Z., 1989. Yield behaviour of dual-phase steel. Scripta Metallurgica 23, 865-870.

Héripré, E., Dexet, M., Crépin, J., Gélébart, L., Roos, A., Bornert, M., Caldemaison, D., 2007. Coupling between experimental measurements and polycrystal finite element calculations for micromechanical study of metallic materials. International Journal of Plasticity 23, 1512-1539.

Hertz, 1896. Miscellaneous papers. New York: Macmillan & Co. Ltd.

Hill, R., 1948. A Theory of the Yielding and Plastic Flow of Anisotropic Metals. Proceedings of the Royal Society of London. Series A, Mathematical and Physical Sciences 193, 281-297.

Hill, R., 1990. Constitutive modelling of orthotropic plasticity in sheet metals. Journal of the Mechanics and Physics of Solids 38, 405-417.

Hosford, W.F., Caddell, R.M., 1993. Metal forming mechanics and metallurgy. Prentice-Hall, Inc.

Houskamp, J.R., Proust, G., Kalidindi, S.R., 2007. Integration of microstructure-sensitive design with finite element methods: Elastic-plastic case studies in FCC polycrystals. International Journal for Multiscale Computational Engineering 5, 261-272.

Hutchinson, J.W., 1976. Bounds and Self-Consistent Estimates for Creep of Polycrystalline Materials. Proceedings of the Royal Society of London. A. Mathematical and Physical Sciences 348, 101-127.

Johnson, K.L., 1985. Indentation contact mechanics. Cambridge University Press, Cambridge.

Kadkhodapour, J., Butz, A., Ziaei-Rad, S., Schmauder, S., 2011a. A micro mechanical study on failure initiation of dual phase steels under tension using single crystal plasticity model. International Journal of Plasticity 27, 1103-1125.

Kadkhodapour, J., Schmauder, S., Raabe, D., Ziaei-Rad, S., Weber, U., Calcagnotto, M., 2011b. Experimental and numerical study on geometrically necessary dislocations and non-homogeneous mechanical properties of the ferrite phase in dual phase steels. Acta Materialia 59, 4387-4394.

Kalidindi, S.R., 1998. Incorporation of deformation twinning in crystal plasticity models. Journal of the Mechanics and Physics of Solids 46, 267-290.

Kalidindi, S.R., Anand, L., 1994. MACROSCOPIC SHAPE CHANGE AND EVOLUTION OF CRYSTALLOGRAPHIC TEXTURE IN PRE-TEXTURED FCC METALS. Journal of the Mechanics and Physics of Solids 42, 459-490.

Kalidindi, S.R., Bhattacharyya, A., Doherty, R.D., 2004a. Detailed analyses of grain–scale plastic deformation in columnar polycrystalline aluminium using orientation image mapping and crystal plasticity models. Proceedings of the Royal Society of London. Series A: Mathematical, Physical and Engineering Sciences 460, 1935-1956.

Kalidindi, S.R., Bhattacharyya, A.,Doherty, R.D., 2004. Detailed analysis of grain-scale plastic deformation in columnar polycrystalline aluminum using orientation image mapping and crystal plasticicty models. Proc. R. Soc. A 460, 1935-1956.

Kalidindi, S.R., Binci, M., Fullwood, D., Adams, B.L., 2006a. Elastic properties closures using second-order homogenization theories: Case studies in composites of two isotropic constituents. Acta Materialia 54, 3117-3126.

Kalidindi, S.R., Bronkhorst, C.A., Anand, L., 1992. Crystallographic texture evolution in bulk deformation processing of FCC metals. Journal of the Mechanics and Physics of Solids 40, 537-569.

Kalidindi, S.R., Duvvuru, H.K., Knezevic, M., 2006b. Spectral calibration of crystal plasticity models. Acta Materialia 54, 1795-1804.

Kalidindi, S.R., Houskamp, J.R., Lyons, M., Adams, B.L., 2004b. Microstructure sensitive design of an orthotropic plate subjected to tensile load. Int J Plasticity 20, 1561-1575.

Kalidindi, S.R., Knezevic, M., Niezgoda, S., Shaffer, J., 2009. Representation of the orientation distribution function and computation of first-order elastic properties closures using discrete Fourier transforms. Acta Materialia 57, 3916-3923.

Kalidindi, S.R., Landi, G., Fullwood, D.T., 2008. Spectral representation of higher-order localization relationships for elastic behavior of polycrystalline cubic materials. Acta Materialia 56, 3843-3853.

Kalidindi, S.R., Niezgoda, S.R., Landi, G., Vachhani, S., Fast, T., 2010. A Novel Framework for Building Materials Knowledge Systems. Cmc-Computers Materials & Continua 17, 103-125.

Kalidindi, S.R., Pathak, S., 2008. Determination of the effective zero-point and the extraction of spherical nanoindentation stress–strain curves. Acta Materialia 56, 3523-3532.

Kalidindi, S.R., Schoenfeld, S.E., 2000. On the prediction of yield surfaces by the crystal plasticity models for fcc polycrystals. Materials Science and Engineering a-Structural Materials Properties Microstructure and Processing 293, 120-129.

Kanjarla, A.K., Van Houtte, P., Delannay, L., 2010. Assessment of plastic heterogeneity in grain interaction models using crystal plasticity finite element method. International Journal of Plasticity 26, 1220-1233.

Knezevic, M., Al-Harbi, H.F., Kalidindi, S.R., 2009. Crystal plasticity simulations using discrete Fourier transforms. Acta Materialia 57, 1777-1784.

Knezevic, M., Kalidindi, S.R., 2007. Fast computation of first-order elastic-plastic closures for polycrystalline cubic-orthorhombic microstructures. Computational Materials Science 39, 643-648.

Knezevic, M., Kalidindi, S.R., Fullwood, D., 2008a. Computationally efficient database and spectral interpolation for fully plastic Taylor-type crystal plasticity calculations of face-centered cubic polycrystals. International Journal of Plasticity 24, 1264-1276.

Knezevic, M., Kalidindi, S.R., Mishra, R.K., 2008b. Delineation of first-order closures for plastic properties requiring explicit consideration of strain hardening and crystallographic texture evolution. International Journal of Plasticity 24, 327-342.

Knezevic, M., Levinson, A., Harris, R., Mishra, R.K., Doherty, R.D., Kalidindi, S.R., 2010. Deformation twinning in AZ31: Influence on strain hardening and texture evolution. Acta Materialia 58, 6230-6242.

Kocks, U.F., Mecking, H., 2003. Physics and phenomenology of strain hardening: the FCC case. Progress in Materials Science 48, 171-273.

Korzekwa, D.A., Lawson, R.D., Matlock, D.K., Krauss, G., 1980. A consideration of models describing the strength and ductility of dual-phase steels. Scripta Metallurgica 14, 1023-1028.

Korzekwa, D.A., Matlock, D.K., Krauss, G., 1984. Dislocation substructure as a function of strain in a dual-phase steel. MTA 15, 1221-1228.

Kroner, E., 1986. Statistical Modelling, in: Gittus, J., Zarka, J. (Eds.), Modelling Small Deformations of Polycrystals. Elsevier Science Publishers, London, pp. 229-291.

Kröner, E., 1977. Bounds for effective elastic moduli of disordered materials. Journal of the Mechanics and Physics of Solids 25, 137-155.

Kroner E. In: Gittus J, Z.J., editors., 1986. Statistical modelling. Modelling small deformations of polycrystals, 229-291.

Landi, G., Kalidindi, S.R., 2010. Thermo-Elastic Localization Relationships for Multi-Phase Composites. Computers, Materials, & Continua 16, 273-294.

Landi, G., Niezgoda, S.R., Kalidindi, S.R., 2009. Multi-scale modeling of elastic response of three-dimensional voxel-based microstructure datasets using novel DFT-based knowledge systems. Acta Materialia 58, 2716-2725.

Landi, G., Niezgoda, S.R., Kalidindi, S.R., 2010. Multi-scale modeling of elastic response of three-dimensional voxel-based microstructure datasets using novel DFT-based knowledge systems. Acta Materialia 58, 2716-2725.

Lebensohn, R.A., Dawson, P.R., Kern, H.M., Wenk, H.-R., 2003. Heterogeneous deformation and texture development in halite polycrystals: comparison of different modeling approaches and experimental data. Tectonophysics 370, 287-311.

Lebensohn, R.A., Liu, Y., Ponte Castañeda, P., 2004. On the accuracy of the self-consistent approximation for polycrystals: comparison with full-field numerical simulations. Acta Materialia 52, 5347-5361.

Lebensohn, R.A., Tomé, C.N., 1993. A self-consistent anisotropic approach for the simulation of plastic deformation and texture development of polycrystals: Application to zirconium alloys. Acta Metallurgica et Materialia 41, 2611-2624.

Lebensohn, R.A., Tome, C.N., Castaneda, P.P., 2007. Self-consistent modelling of the mechanical behaviour of viscoplastic polycrystals incorporating intragranular field fluctuations. Philosophical Magazine 87, 4287-4322.

Levinson, A., Mishra, R.K., Doherty, R.D., Kalidindi, S.R., 2013. Influence of deformation twinning on static annealing of AZ31 Mg alloy. Acta Materialia 61, 5966-5978.

Li, H.-w., Yang, H., Sun, Z.-c., 2006. Explicit incremental-update algorithm for modeling crystal elasto-viscoplastic response in finite element simulation. Transactions of Nonferrous Metals Society of China 16, Supplement 2, s624-s630.

Li, H.W., Yang, H., Sun, Z.C., 2008. A robust integration algorithm for implementing rate dependent crystal plasticity into explicit finite element method. International Journal of Plasticity 24, 267-288.

Li, S., Hoferlin, E., Bael, A.V., Houtte, P.V., Teodosiu, C., 2003. Finite element modeling of plastic anisotropy induced by texture and strain-path change. International Journal of Plasticity 19, 647-674.

Lian, J., Barlat, F., Baudelet, B., 1989. Plastic behaviour and stretchability of sheet metals. Part II: Effect of yield surface shape on sheet forming limit. International Journal of Plasticity 5, 131-147.

Liu, Y.S., Delannay, L., Van Houtte, P., 2002. Application of the Lamel model for simulating cold rolling texture in molybdenum sheet. Acta Materialia 50, 1849-1856.

Lyon, M., Adams, B.L., 2004. Gradient-based non-linear microstructure design. J Mech Phys Solids 52, 2569-2586.

Mayeur, J.R., McDowell, D.L., 2007. A three-dimensional crystal plasticity model for duplex Ti-6Al-4V. International Journal of Plasticity 23, 1457-1485.

Mayeur, J.R., McDowell, D.L., Neu, R.W., 2008. Crystal plasticity simulations of fretting of Ti-6Al-4V in partial slip regime considering effects of texture. Computational Materials Science 41, 356-365.

McDowell, D.L., 2010. A perspective on trends in multiscale plasticity. International Journal of Plasticity 26, 1280-1309.

McGinty, R.D., 2001. Crystallographic multiscale representation of polycrystalline inelasticity. Ph.D. Thesis. Georgia Institute of Technology.

Molinari, A., Canova, G.R., Ahzi, S., 1987. A self consistent approach of the large deformation polycrystal viscoplasticity. Acta Metallurgica 35, 2983-2994.

Musienko, A., Tatschl, A., Schmidegg, K., Kolednik, O., Pippan, R., Cailletaud, G., 2007. Three-dimensional finite element simulation of a polycrystalline copper specimen. Acta Materialia 55, 4121-4136.

Nagorka, M.S., Krauss, G., Matlock, D.K., 1987. The effect of microstructure and strain rate on the stage III strain hardening and ductility of dual-phase steels. Materials Science and Engineering 94, 183-193.

Needleman, A., Asaro, R.J., Lemonds, J., Peirce, D., 1985. Finite element analysis of crystalline solids. Computer Methods in Applied Mechanics and Engineering 52, 689-708.

Nemat-Nasser, S., Guo, W.G., Cheng, J.Y., 1999. Mechanical properties and deformation mechanisms of a commercially pure titanium. Acta Materialia 47, 3705-3720.

Nix, W.D., Gao, H., 1998. Indentation size effects in crystalline materials: A law for strain gradient plasticity. Journal of the Mechanics and Physics of Solids 46, 411-425.

Oppenheim, A.V., Schafer, R.W., Buck, J.R., 1999. Discrete time signal processing. Prentice Hall, Englewood Cliffs, NJ.

Pan, J., Rice, J.R., 1983. Rate sensitivity of plastic flow and implications for yield-surface vertices. International Journal of Solids and Structures 19, 973-987.

Panchal, J.H., Kalidindi, S.R., McDowell, D.L., 2013. Key computational modeling issues in Integrated Computational Materials Engineering. Computer-Aided Design 45, 4-25.

Paruz, H., Edmonds, D.V., 1989. The strain hardening behaviour of dual-phase steel. Materials Science and Engineering: A 117, 67-74.

Pathak, S., Kalidindi, S.R., Klemenz, C., Orlovskaya, N., 2008. Analyzing indentation stress-strain response of LaGaO3 single crystals using spherical indenters. Journal of the European Ceramic Society 28, 2213-2220.

Pathak, S., Stojakovic, D., Doherty, R., Kalidindi, S.R., 2009a. Importance of surface preparation on the nano-indentation stress-strain curves measured in metals. Journal of Materials Research 24, 1142-1155.

Pathak, S., Stojakovic, D., Kalidindi, S.R., 2009b. Measurement of the local mechanical properties in polycrystalline samples using spherical nanoindentation and orientation imaging microscopy. Acta Materialia 57, 3020-3028.

Peeters, B., Seefeldt, M., Teodosiu, C., Kalidindi, S.R., Van Houtte, P., Aernoudt, E., 2001. Work-hardening/softening behaviour of b.c.c. polycrystals during changing strain paths: I. An integrated model based on substructure and texture evolution, and its prediction of the stress-strain behaviour of an IF steel during two-stage strain paths. Acta Materialia 49, 1607-1619.

Peirce, D., Asaro, R.J., Needleman, A., 1982. An analysis of nonuniform and localized deformation in ductile single crystals. Acta Metallurgica 30, 1087-1119.

Peirce, D., Asaro, R.J., Needleman, A., 1983. Material rate dependence and localized deformation in crystalline solids. Acta Metallurgica 31, 1951-1976.

Plunkett, B., Cazacu, O., Lebensohn, R.A., Barlat, F., 2007. Elastic-viscoplastic anisotropic modeling of textured metals and validation using the Taylor cylinder impact test. International Journal of Plasticity 23, 1001-1021.

Plunkett, B., Lebensohn, R.A., Cazacu, O., Barlat, F., 2006. Anisotropic yield function of hexagonal materials taking into account texture development and anisotropic hardening. Acta Materialia - 54, - 4169.

Pollock, T.M., Allison, J.E., Backman, D.G., Boyce, M.C., Gersh, M., Holm, E.A., Lesar, R., Long, M., A.C.Powell, Schirra, J.J., D.D.Whitis, C.Woodward, Integrated

computational materials engineering: A transformational discipline for improved competitiveness and national security.

Popov, E.P., 1998. Engineering Mechanics of Solids, 2 edition ed. Prentice Hall, Englewood Cliffs, New Jersey, USA.

Press, W.H., Teukolsky, S.A., Vetterling, W.T., Flannery, B.P., 2002. Numerical Recipes in C++.

Proust, G., Kalidindi, S.R., 2006. Procedures for construction of anisotropic elastic-plastic property closures for face-centered cubic polycrystals using first-order bounding relations. Journal of the Mechanics and Physics of Solids 54, 1744-1762.

Qu, S., Huang, Y., Pharr, G.M., Hwang, K.C., 2006. The indentation size effect in the spherical indentation of iridium: A study via the conventional theory of mechanism-based strain gradient plasticity. International Journal of Plasticity 22, 1265-1286.

Raabe, D., Roters, F., 2004. Using texture components in crystal plasticity finite element simulations. International Journal of Plasticity 20, 339-361.

Raabe, D., Wang, Y., Roters, F., 2005. Crystal plasticity simulation study on the influence of texture on earing in steel. Computational Materials Science 34, 221-234.

Raabe, D., Zhao, Z., Mao, W., 2002. On the dependence of in-grain subdivision and deformation texture of aluminum on grain interaction. Acta Materialia 50, 4379-4394.

Raabe, D., Zhao, Z., Roters, F., 2001. A finite element method on the basis of texture components for fast predictions of anisotropic forming operations. Steel Research 72, 421-426.

Raabe, D., Zhao, Z., Roters, F., 2004. Study on the orientational stability of cube-oriented FCC crystals under plane strain by use of a texture component crystal plasticity finite element method. Scripta Materialia 50, 1085-1090.

Rossiter, J., Brahme, A., Simha, M.H., Inal, K., Mishra, R., 2010. A new crystal plasticity scheme for explicit time integration codes to simulate deformation in 3D microstructures: Effects of strain path, strain rate and thermal softening on localized deformation in the aluminum alloy 5754 during simple shear. International Journal of Plasticity 26, 1702-1725.

S. R. Kalidindi, A.B., and R. Doherty, 2004. Detailed Analysis of Plastic Deformation in Columnar Polycrystalline Aluminum Using Orientation Image Mapping and Crystal Plasticity Models. Proceedings of the Royal Society of London: Mathematical, Physical and Engineering Sciences.

Sachtleber, M., Zhao, Z., Raabe, D., 2002. Experimental investigation of plastic grain interaction. Materials Science and Engineering A 336, 81-87.

Sakaki, T., Sugimoto, K., Fukuzato, T., 1983. Role of internal stress for continuous yielding of dual-phase steels. Acta Metallurgica 31, 1737-1746.

Salem, A.A., Kalidindi, S.R., Doherty, R.D., 2003. Strain hardening of titanium: role of deformation twinning. Acta Materialia 51, 4225-4237.

Salem, A.A., Kalidindi, S.R., Semiatin, S.L., 2005. Strain hardening due to deformation twinning in α-titanium: Constitutive relations and crystal-plasticity modeling. Acta Materialia 53, 3495-3502.

Salem, A.A., Semiatin, S.L., 2009. Anisotropy of the hot plastic deformation of Ti-6Al-4V single-colony samples. Materials Science and Engineering: A 508, 114-120.

Sarosiek, A.M., Owen, W.S., 1984. The work hardening of dual-phase steels at small plastic strains. Materials Science and Engineering 66, 13-34.

St-Pierre, L., Héripré, E., Dexet, M., Crépin, J., Bertolino, G., Bilger, N., 2008. 3D simulations of microstructure and comparison with experimental microstructure coming from O.I.M analysis. International Journal of Plasticity 24, 1516-1532.

Taylor, 1938. Plastic Strain in Metals.

Tikhovskiy, I., Raabe, D., Roters, F., 2007. Simulation of earing during deep drawing of an Al–3% Mg alloy (AA 5754) using a texture component crystal plasticity FEM. Journal of Materials Processing Technology 183, 169-175.

Van Houtte, P., 1994. Application of plastic potentials to strain rate sensitive and insensitive anisotropic materials. International Journal of Plasticity 10, 719-748.

Van Houtte, P., Delannay, L., Kalidindi, S.R., 2002. Comparison of two grain interaction models for polycrystal plasticity and deformation texture prediction. International Journal of Plasticity 18, 359-377.

Van Houtte, P., Kanjarla, A.K., Van Bael, A., Seefeldt, M., Delannay, L., 2006. Multiscale modelling of the plastic anisotropy and deformation texture of polycrystalline materials. European Journal of Mechanics - A/Solids 25, 634-648.

Van Houtte, P., Li, S., Seefeldt, M., Delannay, L., 2005. Deformation texture prediction: from the Taylor model to the advanced Lamel model. International Journal of Plasticity 21, 589-624.

Van Houtte, P., Van Bael, A., 2004. Convex plastic potentials of fourth and sixth rank for anisotropic materials. International Journal of Plasticity 20, 1505-1524.

Van Houtte, P., Van Bael, A., Winters, J., 1995. The Incorporation of Texture-Based Yield Loci Into Elasto-Plastic Finite Element Programs. Textures and Microstructures 24, 255-272.

Van Houtte, P., Yerra, S.K., Van Bael, A., 2009. The Facet method: A hierarchical multilevel modelling scheme for anisotropic convex plastic potentials. International Journal of Plasticity 25, 332-360.

Watt, D.F., Jain, M., 1984. Effect of martensite morphology on the strength differential effect in dual phase steels. Scripta Metallurgica 18, 1379-1382.

William H. Press, S.A.T., William T. Vetterling, and Brian P. Flannery, 2002. Numerical recipes in C++. Cambridge University Press, Cambridge.

William L. Briggs, V.E.H., 1995. The DFT: an owner's manual for the discrete Fourier transform. Society for Industrial and Applied Mathematics, Philadelphia, PA

Williams, J.C., Baggerly, R.G., Paton, N.E., 2002. Deformation behavior of HCPTi-Al alloy single crystals. Metallurgical and Materials Transactions a-Physical Metallurgy and Materials Science 33, 837-850.

Woo, W., Em, V.T., Kim, E.Y., Han, S.H., Han, Y.S., Choi, S.H., 2012. Stress–strain relationship between ferrite and martensite in a dual-phase steel studied by in situ neutron diffraction and crystal plasticity theories. Acta Materialia 60, 6972-6981.

Wu, X., Proust, G., Knezevic, M., Kalidindi, S.R., 2007. Elastic-plastic property closures for hexagonal close-packed polycrystalline metals using first-order bounding theories. Acta Materialia 55, 2729-2737.

Yoshida, K., Brenner, R., Bacroix, B., Bouvier, S., 2011. Micromechanical modeling of the work-hardening behavior of single- and dual-phase steels under two-stage loading paths. Materials Science and Engineering: A 528, 1037-1046.

Zaefferer, S., 2003. A study of active deformation systems in titanium alloys: dependence on alloy composition and correlation with deformation texture. Materials Science and Engineering: A 344, 20-30.

Zeng, Z., Jonsson, S., Roven, H.J., 2009. The effects of deformation conditions on microstructure and texture of commercially pure Ti. Acta Materialia 57, 5822-5833.

Zhao, Z., Mao, W., Roters, F., Raabe, D., 2004. A texture optimization study for minimum earing in aluminium by use of a texture component crystal plasticity finite element method. Acta Materialia 52, 1003-1012.

Zhao, Z., Ramesh, M., Raabe, D., Cuitiño, A.M., Radovitzky, R., 2008. Investigation of three-dimensional aspects of grain-scale plastic surface deformation of an aluminum oligocrystal. International Journal of Plasticity 24, 2278-2297.